Studying Material Properties On The Nanometer Scale: Instrumental Development And Applications.

Thesis by Stephen D. O'Connor
In partial fulfillment of the requirements for the degree of
Doctor of Philosophy

California Institute of Technology
Pasadena, California
1995
(submitted May 19, 1995)

To Juan Valdez

ACKNOWLEDGMENTS

Kudos to the following:

- Dave Baselt, my AFM guru.
- Kim Komaserik, an undergraduate at Caltech, who is now the world's leading expert on ultramicroscopy of hair.
- Marissa la Madrid, my material science collaborator.
- Marc Unger, a graduate student in the JDB group who was the driving force behind the tip-sample potential derivations.
- Ron Gamble is **the** Ron Gamble of "Gamble Mode"
- Jack Beachamp and Marcel Widmer initiated the mass spectrometry project, which is being continued by Dimitri K., a new graduate student of Jack and John's.
- Schubert Soares was my cohort for all of the sensor work.
- My family.
- And of course, my fearless leader JDB, for paying the bills, among other things.

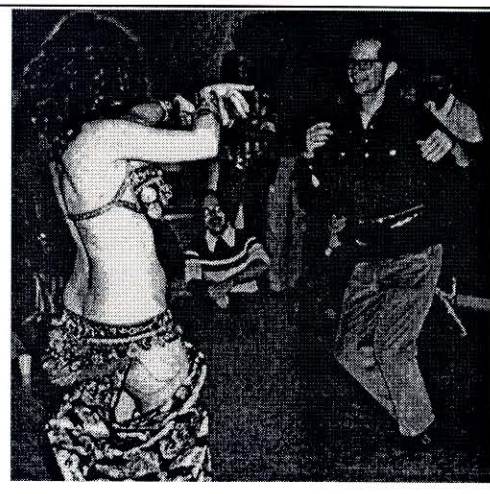

John D. Baldeshweiler during....

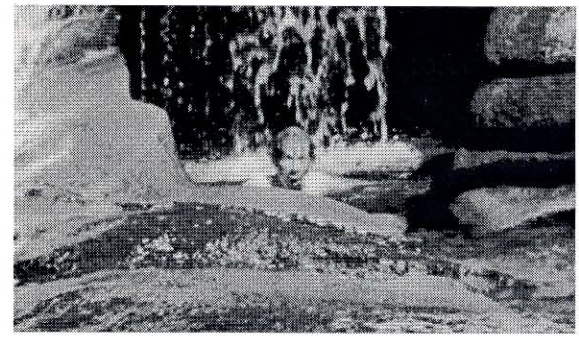

... and after the dancing lesson.

ABSTRACT

This thesis describes experimental work designed to understand and manipulate material properties on the nanometer scale. Two strategies have been explored: instrument development and experimental applications.

Section I describes work associated with atomic force microscopy, including application studies of human hair morphology and the surface microstructure of a bulk metallic glass ($Zr_{41.25}Ti_{13.75}Cu_{12.5}Ni_{10}Be_{22.5}$). Also included in this section are two instrumental advances. First, a mathematical algorithm to extract intermolecular potentials from experimental data is described. Second, a simple, robust method for reducing mechanical noise in these experiments is presented.

Section II outlines early experiments aimed at applying Near-field Scanning Optical microscopy to gas-phase chemical analysis. Standard instruments were constructed and tested. Preliminary work aimed at using the near-field effect to desorb ionized particles from surfaces was also completed.

Section III describes the construction of temperature and vibration sensors based on material properties in silicon. Unprecedented resolution has been obtained with a simple, inexpensive device. The vibration sensors take advantage of Schottky barrier reshaping while the junction is excited with optically induced charge carriers. In a similar manner, the temperature sensors monitor changes in electron mobility.

TABLE OF CONTENTS

PROLOGUE

In 1991, I joined the Baldeschwieler group as a first year graduate student with aspirations of becoming an experimental physical chemist. John was very patient and allowed me to do a lot of exploring in the lab. Along the way, I wasted a lot of time and broke a lot of stuff, but luckily we discovered a number of interesting result which are presented in this thesis. Hopefully, I have presented the results in a format that will be a bit more enjoyable for the reader than the typical thesis. I have tried to avoid detailed experimental procedure and analysis. Instead, I have presented a qualitative description of some of my work, highlighted with a lot of pictures and drawings.

It was problematic to determine a unifying theme for the work I have accomplished. The first theme that popped into mind was "nanotechnology," which is the current trendy description to describe research on "tiny" things. However, it is unclear to me that nanotechnology is the correct word to describe the type of research I have completed. I normally associate the word "technology" with the application of scientific discoveries to commerce and industry. The technologist understands a field and can find pragmatic solutions to "consumer" problems, such as manufacturing, electronics, computers, *etc.*

The experiments described in this thesis are definitely not "applications" of nanometer scale science. Rather, I have studied how materials operate on a small scale, with the hope of eventually taking advantage of this knowledge. A number of strategies have been employed to reach this goal.

- Chapter 1 is a brief review of atomic force microscopy (AFM), which has been an important tool for much of the work described in this thesis.

- Chapters 2 and 3 present experimental results that have been obtained using a commercial AFM with minor modifications. In order to take full advantage of this technique at its current state of development, material systems with unique properties have been considered.

- Chapters 4 and 5 describe AFM instrumentation that has been developed in our laboratory.

- Chapter 6 outlines the early instrumental developments of Near-Field Scanning Optical Microscopy and its conjunction with Mass Spectrometry.

- Chapters 7 - 9 describe work we have accomplished using Schottky barrier detectors as sensors to monitor temperature and vibration changes.

- Appendix I is a patent application that we have filed on tip-modification methods. Two other patents have been filed, but the material is covered in sections 2 and 3.

Chapter 1 - Introduction to Atomic Force Microscopy

Traditional microscopy utilizes solid lenses to bend light rays and magnify images onto a focal plane. Diffraction limits the resolution of this strategy to approximately half the wavelength of light. One way to overcome this problem is to develop alternative microscopies that utilize radiation with much shorter wavelengths, such as electron microscopy (EM). However, EM requires harsh imaging conditions not suitable to many systems.

An alternative imaging mechanism is based on touch. A probe tip is brought near a surface; the interaction between the probe and sample is monitored as the tip is scanned across the surface. It was based upon this principal that Binnig and Rohrer began an imaging "mini-revolution" when they invented the Scanning Tunneling Microscope (STM) in 1982.[1] The STM works as follows:

- a small bias voltage is applied between a conducting tip and sample.
- the tip is brought microscopically close to the surface.
- when the tip-sample distance becomes sufficiently small, electrons will quantum mechanically tunnel between the two conductors, producing a small current.
- this current is exquisitely sensitive to changes in tip-sample separation:

$$i_{tunneling} \propto \exp(-A\phi^{1/2}d),$$

  where **A** is a constant, ϕ is the work function, and **d** is the tip sample distance.
- the tip is now scanned across the surface; differences in tunneling current correspond to differences in electronic topography.

The introduction of STM has led to the development of a number of "probe" microscopies, most notably the atomic force microscope first demonstrated at Stanford in 1985.[2] Atomic force microscopy (AFM) is based on a similar principle as STM in that the interactions that provide contrast are very short range. In AFM, the "interaction forces" between the tip and sample are monitored. In this manner, it is possible to investigate the topology of insulating samples with AFM without the need of a conducting coating.

The ability of probe microscopes to achieve atomic resolution, combined with the flexibliity of the instruments earned its inventors the Nobel Prize in Physics in 1992. Also, a number of successful commercial ventures have been formed to market these instruments (see Table 1).

Company	Location	Academic Affiliation
Topometrix	Santa Clara, CA	Caltech
Digital Instruments	Santa Barbara, CA	UCSB
Park Scientific Inst.	Sunnyvale, CA	Stanford

Our work at Caltech has used AFM in detail. In this chapter, AFM instrumentation and hardware will be discussed. The different imaging modes that are available will also be outlined.

INSTRUMENTATION/HARDWARE

A commercially available AFM system from Topometrix with in-house software[3] was used for the experiments described in this thesis (see Figure 1).

A flexible cantilever is constructed with a small tip on the end. As the tip is lowered into mechanical contact with the sample, attractive/repulsive forces perturb the tip from its equilibrium position. The deflection of the cantilever is monitored as the tip is scanned; a feedback loop may be used to maintain a constant cantilever deflection. Each part of the instrument is described below.

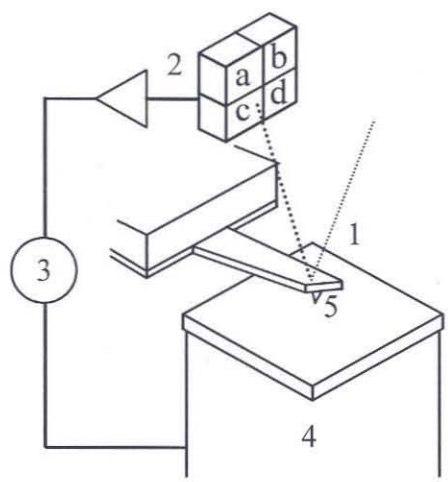

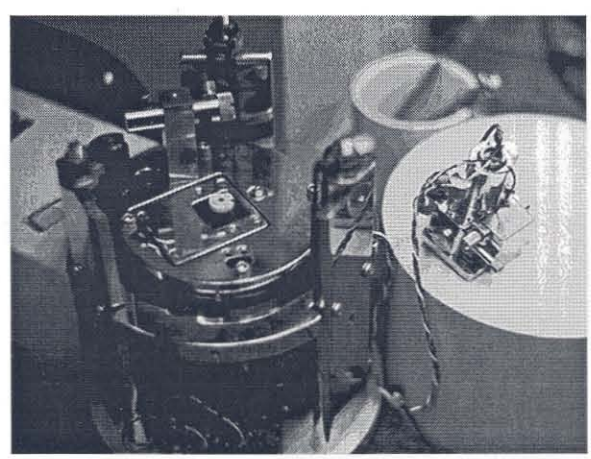

Figure 1: top - AFM schematic; 1 - flexible cantilever with tip; 2 - detector and preamp; 3 - feedback circuit; 4 - piezoceramic scanner (x,y,z); 5 - tip-sample interaction; **bottom** - picture of the Topometrix instrument.

Cantilevers-Tips

The most critical part of an AFM is the cantilever-tip. When the cantilever is perturbed from its free equilibrium position, a force is imparted on the sample; an equal and opposite force will be applied to the cantilever. The size and shape of the tip will determine the attainable resolution.

In order to image in a non-invasive manner, the force applied by the cantilever must be significantly smaller than the forces holding the atoms on the surface together. To a first approximation, the force due to the cantilever will follow Hook's law:

$$F_{cant} = -\mathbf{k}_{cant}\mathbf{z},$$

where $\mathbf{k}_{cant}$ is the cantilever spring constant and $\mathbf{z}$ is the displacement from equilibrium. Typical cantilevers have $\mathbf{k}_{cant} \sim 0.1$ N/m; for comparison, a slinky has a spring constant of 1.0 N/m. This $\mathbf{k}_{cant}$ is much smaller than the force constants of the bonds holding atoms together on a surface (~ 100 N/m for solids).

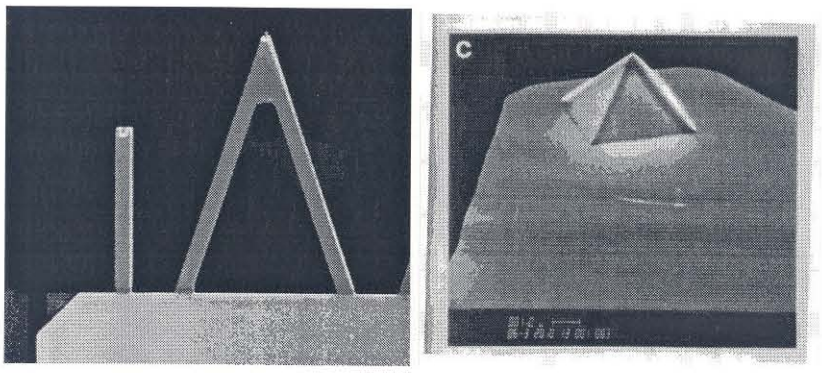

A B

Figure 2: A - two commercially available AFM cantilevers. Image from PSI. **B** - electron micrograph of pyramidal tip; the base of the pyramid is ~ 3 μm.

In order to avoid low frequency coupling, it is also advantageous to construct AFM cantilevers that have high resonant frequencies. The total mass must be small in order to produce reasonable ω_{cant}s. Commercial manufacturers use microlithography to produce cantilevers reproducibly with spring constants ~ 0.1 N/m and $\omega_{cant} > 15$ kHz; these cantilevers are 100 - 400 μm in length. They are made of silicon nitride (Si_3N_4) and coated with a layer of gold to improve reflectivity (see Figure 2A). Two basic shapes are

available: triangular and diving board. The diving board cantilevers are more sensitive to torsional deflection.

A critical feature is the shape of the AFM tip, especially at the apex. During an experiment, the topography recorded by the instrument will be a convolution of the geometries of the tip and sample; the shape of the tip will determine the absolute attainable resolution (see Figure 3). Typically available tips are pyramidal in shape with a 30 - 50 nm end radii (see Figure 2B).[4] Flat samples can be imaged with very high resolution, since small asperities at the end of a tip will be the actual imaging tip for flat samples.[5] However, the total tip diameters are large and will effectively broaden the features imaged for samples with significant vertical topography. Advances have been made to make sharper tips with better aspect ratios.[6,7] However, the sizes of these tips are still very large on the molecular scale.

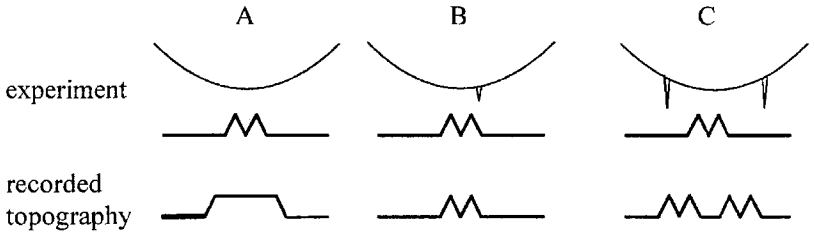

Figure 3: three different tip shapes; **A** - the large radius of curvature makes the small surface features unresolvable; **B** - the small tip asperity is responsible for the imaging, producing a high-resolution image; **C** - a "double tip" produces two images.

Detection

A number of methods have been used to monitor cantilever deflections as the sample is scanned. Initially, Gerber *et al.* used electron tunneling to monitor these changes.[1] Optical detection schemes have proven to be preferable due to their relative experimental simplicity and excellent sensitivity. The most commonly used method is the optical lever; this method is inexpensive and achieves resolution similar to interferometry;[8,9] atomic resolution can be achieved with both of these strategies. A laser diode beam is focused on the back of the cantilever; the light is reflected onto a photodiode (see Figure 4) As the cantilever is deflected a small amount (**d**), the actual movement of the beam at the detector (**D**) depends on the angular deflection (θ) and the distance between the cantilever and detector (**L**). The optical lever gain for our experimental configuration is ~ 2000.

Two signals are simultaneously monitored by the photodiode:

$$\text{current (C)} = (a+b) - (c+d)$$

$$\text{friction (F)} = (a+c) - (b+d)$$

where **a**, **b**, **c** and **d** are the four quadrants of the photodetector as defined in Figure 1. The current corresponds to vertical deflection of the cantilever; the friction signal corresponds to torsion of the cantilever.

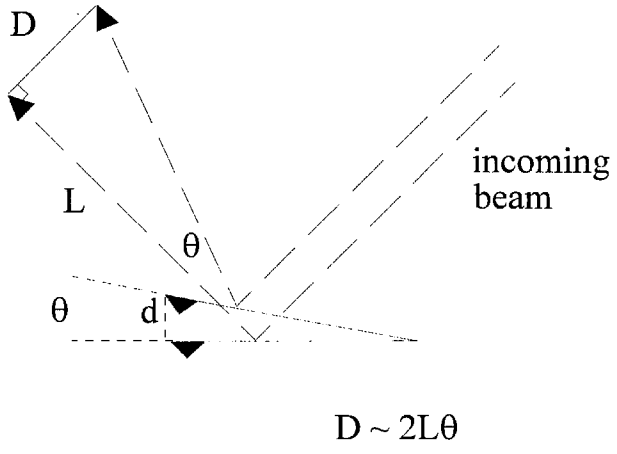

Figure 4: amplification using the optical lever effect. The distance between the cantilever and detector (L) is very large.

Feedback

A feedback circuit maintains a constant cantilever deflection while scanning by adjusting the height of the sample with the tube scanner. A digital proportional-integral-differential feedback circuit algorithm is used with this system.[10]

Scanner

Piezoceramics are used to scan the sample as the tip deflections are monitored; a piezoceramic is a material that expands/contracts as an electric field is applied across one of its dimensions.[11] Three scan ranges are available with our system: 1 μm, 10 μm and 75 μm. The 1 and 10 μm scanners are tube piezoceramics; the 75 μm scanner is a pivoting design (see Figure 5). The sample is mounted on a metallic disk and held to the scanner using a magnet. This scheme allows for easy sample replacement while maintaining rigid contact to the scanner.

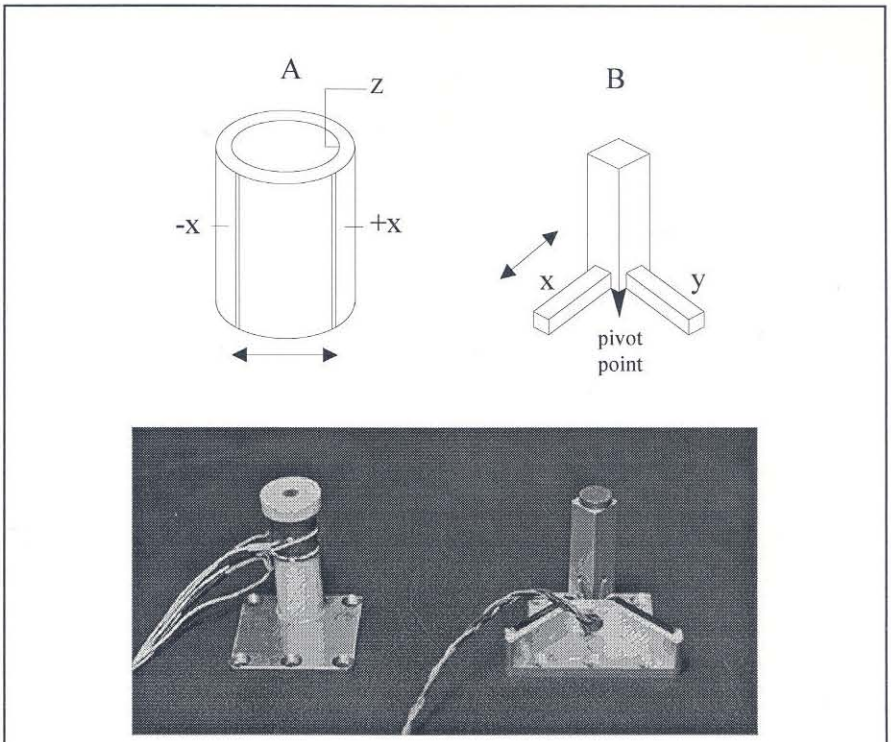

Figure 5: **A** - a tube piezoceramic produces stable, 3-axis translation. As high voltages are applied between quadrant segments of outer electrodes (labeled + x and - x) and the inner common ground, the tube can be made to move in the direction of the arrow; the tube is translated in the z direction by applying a bias voltage to the inner electrode; **B** - a pivoting design has three orthogonal piezos for x,y,z translation.

IMAGING MODES

Two general classes of imaging are performed: static and dynamic. Static modes monitor the DC error voltage required to maintain a fixed cantilever position. Dynamic imaging involves monitoring an AC signal that shifts when the cantilever approaches the sample and as the sample is scanned.

Contact Mode

To image a sample, the tip-sample separation is decreased until the interaction potential is strong enough to perturb the cantilever from its equilibrium position. If a strong attractive force is present between the tip and sample, attractive mode imaging may be accomplished. However, this mode is usually unstable. More practical is to bring the tip into the repulsive regime of the interaction potential until the cantilever is deflected away

from the sample. The force from the cantilever is equal and opposite the force from the interaction potential:

$$k_{cant}z - \frac{\partial}{\partial q}U(q) = 0,$$

where **z** is the displacement of the cantilever, **q** is the tip-sample distance, and U(**q**) is the interaction potential between the tip and sample. As the tip is scanned, changes in sample topography and composition will alter U(**q**) and the position of the cantilever will change. Imaging contrast corresponds to local changes in U(**q**) and can be monitored in two ways:

1. **constant deflection:** the feedback loop maintains a constant cantilever deflection by altering the height of the sample as the tip is scanned. This mode is also referred to as constant force mode, since the imaging force does not change (the recorded topography is actually the correlation of topography and sample compressibility; for most samples, compressibility is constant.).

2. **constant height:** the feedback loop is turned off. The sample is scanned at constant height and the changes in cantilever deflection provide contrast.

Both of the imaging modes work very well on hard samples. They are easy to implement and have fairly low background noise. However, the cantilever imaging force ($-k_{cant}z$) may be large enough to perturb soft biological samples.

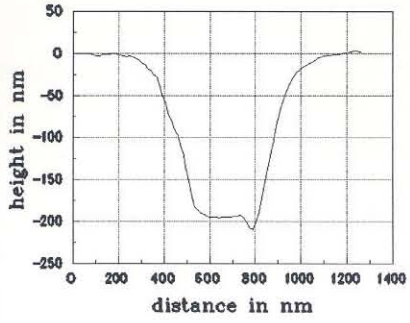

A

B

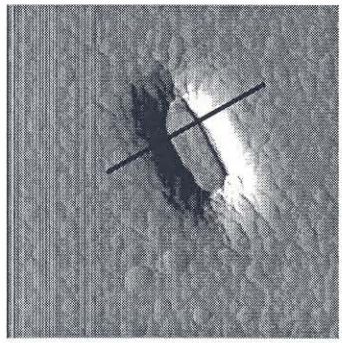

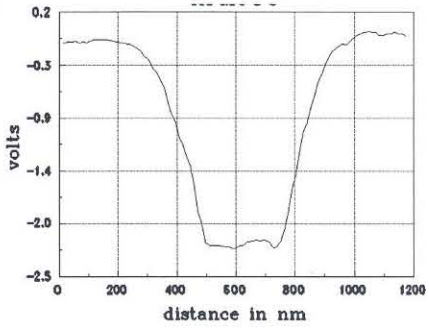

C

D

Figure 6: A - constant deflection image of a CD pit; **B -** linecut of the height data corresponding to the line drawn in A. The pit is ~ 200 nm deep. **C -** constant height image of the same pit. **D -** the y axis is now in volts on the photodetector; 200nm = 2 Volts, therefore 1Volt at the detector is approximately equal to 100 nm of cantilever deflection.

Frictional Force Microscopy (FFM)

The lateral force applied to the cantilever can be simultaneously monitored in contact mode [F = (a + c) - (b + d) from Figure 1].[12,13] These lateral forces correspond to local changes in surface friction. However, cross-talk between the local height and lateral force makes interpretation of these images problematic; a sudden change in the slope of the sample features will produce a component of lateral force that does not correspond to a frictional change. In order to remove this cross-talk, the forward and reverse scans are both saved. When going up a slope, the friction appears artificially high; in the reverse scan, this same area will artificially appear as low friction(see Figure 7).[10] Therefore, if the forward and reverse scans are added, friction-topography crosstalk will be minimized and primarily differences in friction will remain.

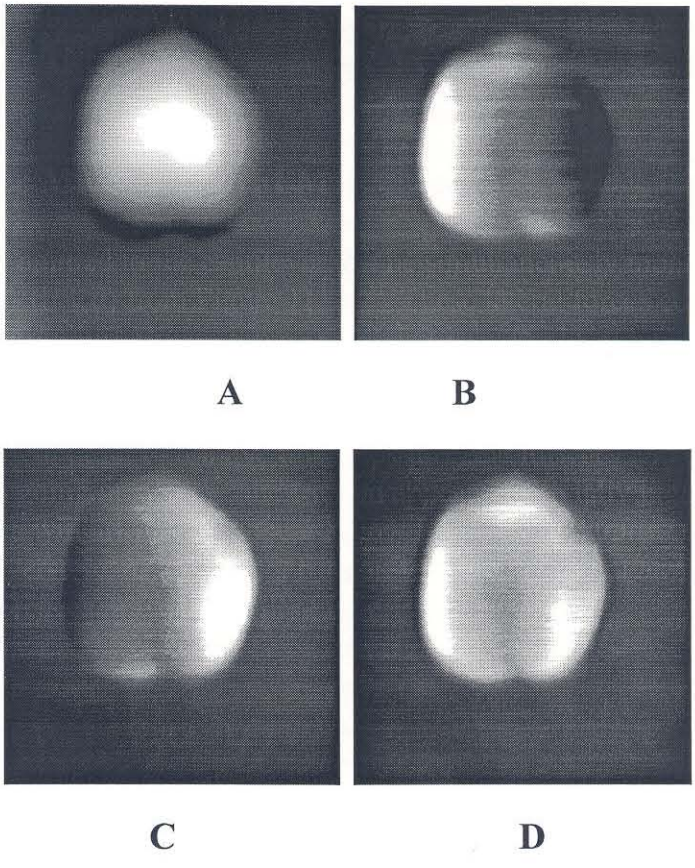

Figure 7: 540 nm AFM images of a reverse-micelle on mica. **A** - topography; **B** - left-to-right friction image. Notice the high friction on the left and low friction on the right of the micelle; **C** - right-to-left friction image; **D** - B + C, cross-talk is eliminated and the true friction is displayed. The reverse-micelle is "stickier" than the underlying mica substrate.

Resonance Non-contact

Resonance non-contact mode is an alternative to the static modes described above[14]:

- the cantilever is vibrated at its fundamental resonance frequency (ω_0 = 15 - 25 kHz for commercially available cantilevers).[15]
- as the tip-sample distance is decreased, the interaction potential will alter the resonance frequency of the cantilever; applying a force to the tip is effectively the same as altering the spring constant of the cantilever.
- since the driving frequency (= ω_0) is no longer equal to ω_{cant}, the amplitude of the cantilever vibration will be lowered an amount that depends on the quality factor (**Q**).
- a shift in the amplitude of the AC signal at the detector can be used as a setpoint for feedback.
- in a similar manner, altering the ω_{cant} will also shift the phase of the vibration with respect to the phase of the driving signal; this phase shift can also be used for feedback control.

Appreciable changes in phase and amplitude can occur in the attractive regime of the interaction potential; also, lock-in techniques can be used in this mode which lower the total noise. Unlike a static attractive mode, this dynamic mode allows lock-in detection of the cantilever response, increasing the stability of the feedback loop. Also, the effects of the surface potential can be monitored at a much longer range with this strategy than for contact mode imaging.

Scanning Chemical Microscopy (SCM)

The addition of chemical contrast would make AFM an extremely powerful tool for studying biological system and material properties. A number of preliminary experiments have been performed in this area. An AFM tip is derivatized with known chemical groups. As the forces between this tip and a sample are monitored, it is possible to elucidate the nature of the chemical interactions in a quantitative manner; these forces will be different as the specific chemical groups are changed (see Chapter 4). Two strategies have been employed to detect these chemical differences: force curves and lateral force detection.

Force Curves

A force curve is a plot of cantilever deflection versus z position:[16]

- the sample is fully retracted away from the tip (no deflection).
- as the tube scanner decreases the tip-sample separation, the cantilever deflection is monitored.
- once the cantilever reaches its fully deflected position (maximum cantilever deflection); the sample is then retracted in the same manner.

The tip-sample interaction potential can be extracted from this force curve. Also, if the tip geometry is known, single inter-molecular pair potentials can be determined. Force curves are discussed in detail in Chapter 4.

A number of force curve experiments have been used to determine interaction potentials between specific chemical moieties:

1. Ho *et al.* observed quantized adhesion which they attributed to single hydrogen bonds; their experimental value of 10 piconewtons agrees with theoretical calculations.[17]
2. Lee *et al.* determined the binding constants for both the streptavidin-biotin interaction and DNA duplex formation.[18,19]
3. Dammer *et al.* measured the binding force between cell adhesion proteoglycans from a marine sponge. A single molecule was studied and found to adhere with a force as large as 400 piconewtons.[20]

Determining the true chemical nature of a surface from a force curve is extremely difficult, unless the surface is homogeneously prepared. The addition of different local forces quickly makes interpretation problematic, especially since the contact area for a tip-sample interaction is still fairly large on a molecular scale. [Recall, the radius of curvature for a typical AFM tip is 30 -50 nm.] Therefore, imaging an unknown surface with this detection strategy is currently problematic (*e.g.* it is difficult to discriminate effects of topography versus composition).

Lateral detection

An alternative method for detecting chemical contrast has been implemented by Frisbie *et al.*[21] A surface test pattern was constructed that consisted of alternating regions of hydrophobic/hydrophilic chemical groups; $-CH_3$ terminated thiols were used in the hydrophobic region; -COOH terminated thiols were used in the hydrophilic region. AFM tips were modified in a similar manner. As the tip was scanned across the test pattern, both the topography and friction was monitored. When the $-CH_3$ tip was used, high friction occurred when the tip was over the $-CH_3$ terminated area of the test pattern (see Figure 8); the opposite behavior was observed with the -COOH terminated tip.

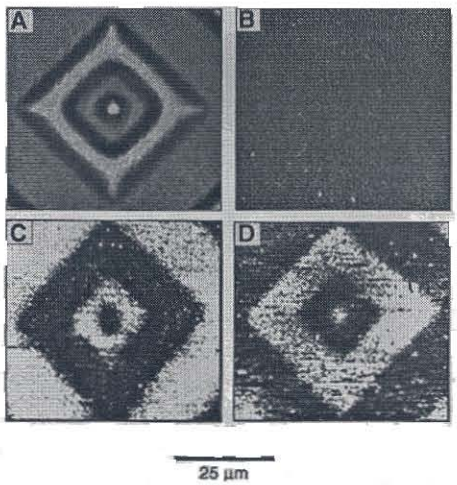

Figure 8: SCM test pattern **A** - optical image, the light area is the -COOH terminated region; **B** - AFM topography image, the surface is flat; **C** - frictional image with a $-CH_3$ terminated tip, the bright regions correspond to high friction; **D** - friction image with -COOH tip. This image was taken from reference 20.

The major technological hindrance for this strategy is the modification of the AFM tip in a reproducible, covalent manner. Frisbie *et al.* used thiol binding to gold.[22] However, a gold coating must be applied to the AFM tip prior to derivatization; this coating increases the radius of curvature even further. Marc Unger, a graduate student in our group at Caltech, is developing methods to chemically derivative AFM tips using silinization chemistry.[23] This strategy should allow SCM to be performed at high resolution.

Other Contrast Mechanisms

Numerous contrast mechanisms have been combined with the general AFM strategy, including magnetic resonance;[24] magnetic force;[25,26] thermal imaging;[27] ion-conductance;[28] capacitance;[29] ultrasonic modulation.[30]

REFERENCES

1. Binnig G., Rohrer H., Gerber C., Weibel E. Phys. Rev. Lett. **49**, 57 (1982).
2. Binnig G., Quate C., Gerber C. Phys. Rev. Lett. **56**, 930 (1986).
3. Baselt D., Clark S., Youngquist M., Spence C., Baldeschwieler J. RSI **64**, 1874 (1992).
4. Albrecht T., Akamine S., Carver T., Quate C. JVSTA 8, 3386 (1990).
5. Albrecht T. and Quate C. J. Appl. Phys. **62**, 2599 (1987).
6. Keller D. and Chih-Chung C. Surf. Sci. **268**, 333 (1992).
7. Ultralevers are available for Park Scientific Instruments.
8. Meyer G. and Amer N. Appl. Phys. Lett. **53**, 2400 (1988).
9. Putman C., De Grooth B., Van Hulst N., Greve J. J. Appl. Phys. **72**, 6 (1992).
10. Baselt D. Ph.D. Thesis, Caltech (1993).
11. Piezoceramics are commercially available from Staveley Sensors, East Hartford CT and Channel Industries Santa Barbara CA.
12. Mate C., McClelland G., Erlandsson R., Chiang S. Phys. Rev. Lett. **59**, 1942 (1987).
13. Baselt D. and Baldeschwieler J. JVSTB **10**, 2316 (1992).
14. Martin Y., Williams C., Wickramasinghe H. J. Appl. Phys. **61**, 4723 (1987).
15. Chen G., Warmack R., Thundat T., Allison D., Huang A. RSI **65**, 2532 (1994).
16. Burnham N., Colton R., Pollock H. Nanotech. **4**, 64 (1993).
17. Hoh J, Cleveland J., Prater C., Revel J., Hansma P. JACS **114**,4917 (1992).
18. Lee, G., Kidwell,D., Colton R. Langmuir **10**, 354 (1994).
19. Lee, G., Chrisey L., Colton R. Science **266**, 771 (1994).
20. Dammer U., Popescu, O., Wagner, P., Anselmetti D., Guntherodt H., Misevic G. Science **267**, 1173 (1995).
21. Frisbie C., Rozsnyai F., Noy A., Wrighton M., Lieber C. Science **265**, 2071 (1994).
22. Weick B., Furey M., Vick B. J. Tribology **116**, 260 (1994).
23. Dang T. and Gnanasekaran R. JVSTA **9**, 1406 (1991).
24. Rugar D., Zuger O., Hoen S., Yannonni C., Vieth H., Kendrick R. Science **264**, 1560 (1994).
25. Grutter P. Wadas A. Meyer E .Heinzelmann H. Hidber H. et al. JVSA **8**, 406 (1990).
26. Wadas A., Rice P., Moreland J. Appl. Phys. A **59**, 63 (1994).
27. Maywald M., Pylkki R., Balk L. Scan. Micr. **8**, 181 (1994).
28. Bard A., Denuault G., Lee C., Mandler D., Wipf D. Acc. Chem Res. **23**, 357 (1990).
29. Williams C., Hough W., Rishton S. Appl. Phys. Lett. **55**, 203 (1989).
30. Rabe U. and Arnold W. Ann. Physik **3**, 589 (1994).

CHAPTER 2 - Atomic Force Microscopy of Human Hair Cuticles: A Microscopic Study of Environmental Effects on Hair Morphology

An atomic force microscope has been used to provide quantitative real-time analysis of human hair morphological changes under ambient conditions; this form of microscopy combines the lateral resolution of an electron microscope and the flexibility of a light microscope. Three experiments were performed: a study of hair morphology in air versus water, a kinetic study of hair hydration and a determination of how pH changes affect hair morphology. The overlapping keratinized cells that form the hair cuticle spread out between 50-150% when hydrated, compared to a total shaft diameter change of 10%. This hydration reaches a saturation point within the first few minutes after immersion. Also, hair swells much more at higher pH.

INTRODUCTION

The growth of hair follicles and the accompanying keratinized cells has been studied for many years and is well understood.[1] However, the mature hair shaft has been the subject of less intense analytical study. The effects of external chemicals on the hair shaft are of great interest in both the medical field and cosmetic industry. Current methods to analyze these effects consist mainly of macroscopic testing such as touch and tell little about the actual hair morphology.

Light microscopy has been used to analyze macroscopic properties of hair using numerous staining techniques.[2] Electron microscopy has complemented these experiments and been a useful tool to study microscopic hair morphology.[3] However, these techniques have two very restrictive limitations; light microscopy is limited in lateral resolution whereas electron microscopy does not allow ambient imaging conditions.

A new method for analyzing hair morphology at high resolution and under ambient conditions has been explored in our laboratory. An atomic force microscope (AFM)[4,5] has been used in these experiments to analyze hair morphology as the environmental conditions are changed, allowing the direct study of hydration effects. The AFM combines the lateral resolution of an electron microscope with the environmental flexibility of the light microscope. Also, the height resolution is superior to either technique.

Traditional microscopy utilizes solid lenses to bend light rays and magnify images onto a focal plane. However, due to diffraction these techniques are limited in resolution to approximately half the wavelength of light. One way to overcome this problem is to turn to alternative forms of radiation that have a much smaller wavelengths, such as electron microscopy (EM). However, EM requires that imaging be done under vacuum, and insulating biological samples usually require a metal coating prior to imaging.

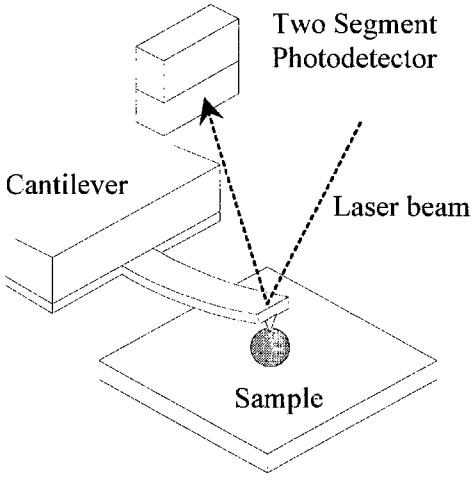

Figure 1. Atomic Force Microscope (AFM) schematic - a laser beam is focused onto the back of a flexible cantilever. The reflection then strikes a two quadrant position sensitive photodiode. As the cantilever is raster scanned across the sample, its relative height can be monitored since the beam will strike a new position on the photodetector.

Probe microscopy utilizes an alternative imaging mode where a sharp tip is brought very close to a surface and the tip-sample interaction is monitored as the tip is scanned. The resolution for this approach is limited by the size of features on the probe. To image using AFM, a cantilever with a small pyramidal tip is placed over the sample and lowered into mechanical contact. A tube piezoceramic is then used to scan the tip over the sample in sub-angstrom steps. The deflection of the cantilever corresponds to changes in height of the sample. These motions are monitored by reflecting a laser beam from the cantilever onto a position sensitive two-quadrant photodiode (see Figure 1).

AFM has been used to study a number of interesting biological systems. For instance, very high resolution images of DNA, proteins, and DNA-protein complexes have been obtained under physiological conditions.[6,7,8] However, true molecular resolution was not observed due to the large tip sizes; this hinderance remains a problem for all AFM experiments. Larger biological systems have also been studied, such as living neurons and activated platelets.[9,10] However, no quantitative data about hydration rates or pH dependence has been extracted from these studies.

MATERIALS AND METHODS

These experiments have been performed with a Topometrix[11] AFM system with in-house software.[12] A pivoting 75 μm scanner and standard pyramidal tips were used in all of these experiments.

All the hair samples were taken from the heads of undergraduate students at Caltech. Hair from 7 students was imaged. The areas of the hair imaged were at least 1 cm away from the scalp. Since this study was designed to demonstrate the power of AFM as an analytical technique for studying hair morphology, no precautions about hair condition, care, diet, *etc.* were taken prior to acquisition of the samples.

To prepare the samples, the hair was cut, stretched over a sample stud and bonded with five minute epoxy on the ends to hold it in place. The samples were rinsed with water to remove excess contaminants before imaging. Three different experiments were performed:

1. A comparison of hair morphology in air versus water.
2. A kinetic study to determine the rate of hydration of the hair.
3. A determination of the hair morphology changes versus pH.

For all 7 subjects, over 200 images of hair in water and 100 images in air were taken and compared. All of the images shown in this report are quite typical and reproducible. In order to determine the rate at which the hair absorbs water, an area of a hair in air was imaged. Distilled water was then added and another image was taken every 30 seconds for 7 minutes in the same area. The steps in the region imaged were then analyzed and averaged. This procedure was performed on two subjects. Longer term hydration was also studied by taking a scan every 2 minutes for 40 minutes. This procedure was repeated for four subjects.

To determine the effects of pH on hair morphology, a hair was soaked in distilled water for 25 minutes. The hair was then immersed in phosphate buffer that had been pH adjusted with hydrochloric acid and sodium hydroxide. Eight different pHs were used. After incubation for five minutes in the buffer, images were taken every five minutes over different regions for ~ 30 minutes; this procedure was completed for one subject.

RESULTS

Morphology in Air vs. Water

Figure 2A is a typical 63 x 63 μm image of hair in air. The image has been shaded with a simulated light source from the right in order to highlight the structural differences; no other image processing has been performed. The hair cuticle exhibits consecutive overlapping sheaths. These sheaths are layers of imbricated, keratinized cells that make up the cuticle. A linecut was taken in order to show quantitative height data versus position. The line inserted into the picture shows the location of the corresponding linecut shown in Figure 2B. Throughout this paper, the height of one sheath relative to the next will be referred to as the step height. The average step height of the sheaths in air is approximately 500 nm. Occasionally there will be a larger step in the 1-2 μm range; less than 5% of the steps measured exhibited this larger size. The average diameter of the hair shafts in air was reproducible and approximately 50 μm.

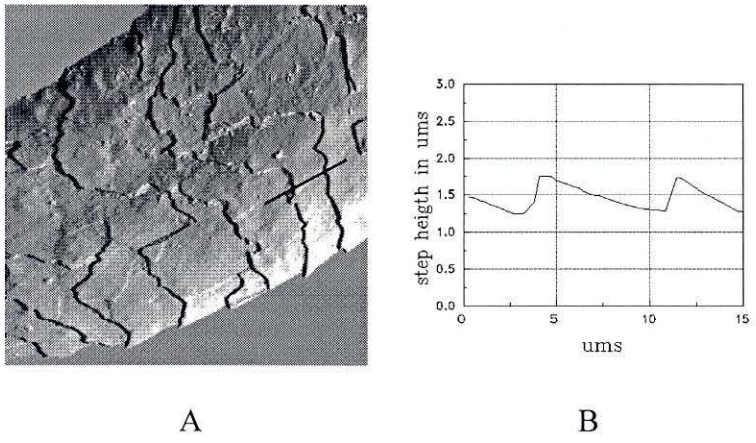

Figure 2 - A. 63 x 63 μm AFM image of hair in air - there are 256 x 256 pixels and the entire image was acquired in 62 seconds. The image is light shaded in order to accentuate the features. No other image processing was performed.
B. AFM linecut - the data represents the quantitative height data following the line drawn in **2A**; from left to right, the two steps are 500 and 400 nm respectively.

Figure 3A is a 44 x 44 μm image of hair from the same subject as used in Fig. 2, after it had been soaked in water for 30 minutes. The step heights are about 1 μm, as shown in Figure 3B. For this subject, an average step height of 1200 nm was observed for the hairs soaked in water, approximately a 140% increase. Certain steps were occasionally as small as 500nm; less than 10% of the steps imaged were this small.

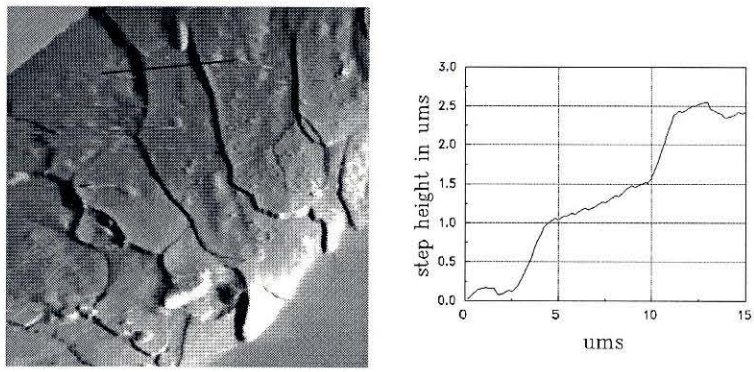

A B

Figure 3. A. 44 x 44 μm AFM image of hair in water - the hair was immersed in distilled water for ~ 30 minutes. Imaging parameters are the same as Fig. 2.
B. AFM linecut - the two steps are 1100 and 1000 nm respectively. This linecut exhibits a different slope that the one in Figure 2 due to an overall sample slope. It does not effect the quantitative data.

Kinetics of hydration

Figure 4 is a plot of a single step height for a single subject versus time. The hair was imaged in air, then immersed in water and reimaged. (The microscope requires a realignment procedure once the water is added that takes 1-2 minutes, therefore the first data point in water is always delayed.) Images were then taken of the same area every 30 seconds for 7 minutes. The data shown are a single step height change versus time. The majority of the hydration occurs in the first 2 minutes after immersion. A first-order exponential fit to this data gives:

$$\text{step height (nm)} = 680\ \text{nm} - (226\ \text{nm} \times \exp^{-0.0117\ \text{sec}^{-1} \times \text{time}}).$$

The rate constant is 0.0117 sec^{-1}, with a correlation better than 99%. This value was reproducible for scans of the same subjects hair. The error bars represent the standard deviation in the measurement of the step height.

The kinetic experiment was repeated with the same subject and showed remarkably similar results. Also, experiments have been carried out up to 40 minutes with data points every 2 minutes for three subjects; again the majority of the hydration occurred in the first few minutes

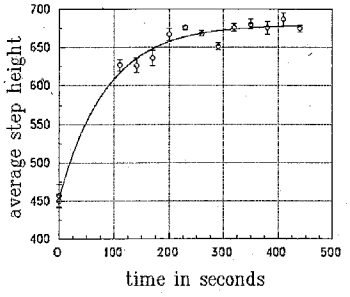

Figure 4. Step heigh versus time - the average step height versus time of a single hair step for a single subject. Each data point is the average value of a single step; the error bars represent the standard deviation in the measurement of the average step height at each point. The first data point at time = 0 represents the step height in air. The solid line in an exponential fit to the data with a correlation better than 99%.

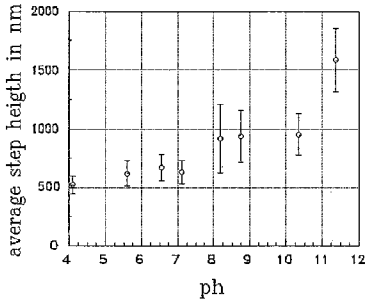

Figure 5. - Step Height versus pH - Each data point is an average of many steps from the same subject at different pH levels; the error bars are the standard deviation of each. The imaging solutions were phosphate buffer that was pH adjusted with hydrochloric acid and sodium hydroxide. The images were taken after soaking the hair for 25 minutes in distilled water and then 5 minutes in the buffered solution, well beyond the saturation time determined from Figure 4 Images were then taken every 5 minutes for the next 30 minutes.

Hair Morphology vs. pH

Figure 5 is a plot of step height versus pH. Each data point is an average of at least 30 steps from hair from the same subject. The first image in each case was taken after 25 minutes in water followed by 5 minutes in the buffered solution, well beyond the saturation time determined from Figure 4.

A critical observation is that the step height depends on both the initial and the final pH values. For example, if a hair is immersed in buffer at pH 7 for 25 minutes and then imaged in buffer at pH 8, a very different average step height is observed compared to a hair that is immersed in pH 6 buffer for 25 minutes, but again imaged at pH 8. Therefore, each data point in Fig. 5 represents step heights observed for a "fresh" hair sample from the same subject, initially soaked in distilled water for 25 minutes, then imaged at the pH level indicated. The error bars are the standard deviation of measurements of the step heights. An increasing trend in average step height is shown. A similar trend was observed with samples from other subjects. At high pH, not only do the step heights increase dramatically, but visible degradation (possibly hydrolysis) occurs (see Figure 6).

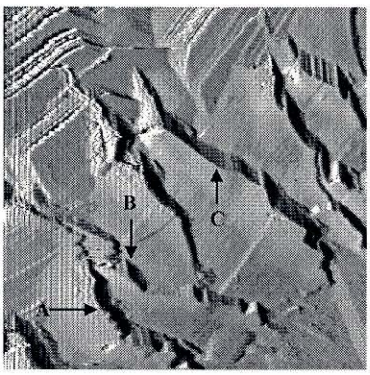

Figure 6. 38 x 38 μm AFM image of hair at high pH - the hair has been soaked in buffer at pH 11.39 for ~ 5 minutes. The arrows denoted by a, b, and c are three steps of height 2200, 1400, and 1500 nm respectively. Visible degradation of the hair is occurring; the edges of the hair are no longer apparent as in Figure 4. The blurring of the image is not due to instrument noise.

DISCUSSION

Morphology in Air vs. Water

Hair could be more susceptible to damage when wet than when dry. Since hair is a complex composite of protein fibers and keratinized cells, it may be possible that adding water hydrates these fibers and weakens their three-dimensional structure. A total shaft diameter increase when hair is immersed in water or buffer (typically about 10%) was observed. This swelling has also been observed with light microscopy. The sheath step height increases dramatically compared to the total shaft swelling. Two factors could be responsible for this dramatic difference: the outer layer of cells could be taking up a larger amount of water than the total hair shaft, or the overlapping cells of the cuticle could be separating once hydrated. A number of studies have investigated the binding states of water in keratin.[13,14] However, these studies have been directed at a molecular understanding. Our investigation correlates macroscopic morphology to hydration.

It would be advantageous to protect the hair cuticle from hydration and swelling while hair is immersed, for instance during swimming and bathing. If a conditioner or hair treatment could be devised that inhibited hydration, it could act as a protective coating. Currently, the effectiveness of these chemical treatments is determined based on the macroscopic properties of hair and is often subjective. Quantitative information about relative sheath height changes may be more pertinent.

This study has shown that AFM is an excellent analytical technique to provide quantitative information on morphological changes under ambient conditions. Also, this method eliminates subjectivity that is often used in determining hair care effectiveness. A large increases in step heights was observed in certain subjects (see Figures 2 and 3). In other samples, the increase in sheath step height in water is not nearly as dramatic. In Figure 4, the single step studied has a height of 460 nm in air. After soaking in water for 5 minutes it is 675 nm. This is a 47% increase in step height. Still, this opening is much more dramatic than the overall hair diameter change, which is approximately 10%.

A rigorous analysis of the hair treatment for this sampling group has not been completed. This study is meant to show the ability of AFM for studying this type of system.

Kinetics of Hydration

In order to take full advantage of the AFM to image hair morphology, it is important to understand how hair interacts with water. As can be seen from Figure 4, the hydration of the hair seems to saturate very quickly, after just a few minutes. Therefore, an incubation time of at least 3-5 minutes should be used before morphological changes are studied in order to avoid confusion from simple hydration kinetics.

Hair Morphology vs. pH

The manner in which chemicals effects hair morphology will be very important in designing intelligent chemical additives for hair treatment. A simple study on how the average step height is effected by pH changes has been completed and provides basic information about the morphological effects of the hydration process.

Figure 5 shows an increasing trend in the sheath step height as the pH increases. This trend has been observed with numerous samples and averaging techniques. The increase is most dramatic at high pH, where the hair is visibly degraded. In Fig. 6, the hair begins to loose its cylindrical shape after only 5 minutes in the pH 11.4 buffer. After a few minutes at this pH, the hair began to fall apart. This could be seen by simply looking at the sample visually. This degradation also occurred at pH 10.4 after about 15 minutes. It is possible that this degradation is due to the large increase in step height at this pH. The sample soaked at pH 4 did not exhibit this behavior; the three-dimensional structure of the hair at this pH remained completely intact even after 30 minutes incubation.

A possible explanation for the observed differences in total swelling for various subjects, as well as the observed pH curve, is that cationic surfactants are covering the hair prior to sampling. Empirical observations show that cationic surfactants make good conditioners.[15] An increase in pH would cause the removal of these cationic conditioners, making the hair more susceptible to hydration. At low pH, the cation head groups would remain charged and adsorbed to the hair. This mechanism may also

explain why various steps open a different amount under water, since incomplete coverage of the surfactant may occur from one region of the hair to another.

In this study, a new methodology for studying hair morphological changes has been presented. We believe it is a superior technique to any available; it combines the high resolution of electron microscopy with the environmental and sample flexibility of light microscopy. The dual advantage that AFM affords may make it an ideal choice for studying early stages of certain clinical hair abnormalities that would otherwise go undetected. Also, it should be an effective tool for determining the effectiveness of hair care treatment.

FUTURE EXPERIMENTS

The effects of external chemical additives on the hair shaft is of great interest in both the medical field and cosmetic industry. Current methods to analyze these effects consist mainly of subjective macroscopic testing such as touch and tell little about the actual effects on hair morphology. Typically, conditioned hair is described by "the ease by which a comb can be pulled through freshly washed hair."[16]

US Patent #4,507,280 claims "a hair conditioning composition relatively stable toward repeating shampooing comprising an aqueous acidic composition containing a cationic polymer product, and amphoteric surfactant product and a betaine." We hypothesize that these compounds form a protective layer over the hair cuticle, protecting the hair shaft from hydration. An AFM will be used to explore this hypothesis by analyzing hair morphological changes *in situ*.

Experimental Methodology

We wish to investigate the effect of chemical additives on hair morphology. We hypothesize that the additives cover the hair cuticle and inhibit hydration. We also hypothesis that our preliminary results were tainted by the presence of residual shampoo or conditioner prior to imaging. The following assumptions make the experiments viable:

1. The swelling observed in the preliminary experiments is indeed caused by hydration.
2. The hydration may damage the three dimensional structure of the hair.
3. Stopping hydration would therefore protect the hair.

In order to examine this hypothesis, three tasks will be performed:

- The hair will be cleaned.
- The hair will be imaged without the presence of condition.
- The hair will be imaged after treatment with conditioner.

First, we must repeat the preliminary experiments in a more controlled manner. Hair will be obtained from a controlled test group. For example, all white females between the ages of 18-20 with long straight brown hair and similar health. Many samples will be taken from each subject; we will also keep track of how far from the scalp the hairs are removed. The hair will then be cleaned as previously described.[17] This cleaning should remove any residual conditioner or surfactant left on the hair which could be responsible for artifacts. The hair will then be imaged in air and in water as before. There are three possible outcomes:

The step heights expand...

1. a similar amount as observed in the preliminary experiments
2. to a greater degree.
3. to a lesser degree.

Outcome 2 would be consistent with our hypothesis that the preliminary experiments were tainted by poor sample preparation. Outcomes 1 or 3 would mean that either our hypothesis was incorrect, or our cleaning method did not effectively remove the shampoo or conditioners. If outcome 1 or 3 is observed, we will attempt alternative cleaning methods. The expansion trends for a single subject should be similar for each sample. If they are not, it is possible that the cleaning method is ineffective.

The final experiments will be to determine the effect of conditioners on hair morphology. A number of commercially available conditioners will be obtained. One example is the betaine conditioner mentioned in the introduction. The hair will be treated with conditioner, imaged in air and then imaged in water as before. Three outcomes are possible:

The steps may open up ...

1. a similar amount as observed when they were untreated.
2. to a greater degree.
3. to a lesser degree.

Outcome 3 would be consistent with our hypothesis that the conditioners will protect the hair from hydration. Outcome 1 would indicate that the conditioners have little or no effect. Outcome 2 would indicate that the conditioner acts in the exact opposite manner that we predicted and could be a very poor choice as a conditioner. The relative effects of different conditioners on hair morphology can be quantified using the AFM in this manner.

Discussion

The step height change observed in our preliminary work could have been caused by one of two phenomena: the outer cells of the cuticle could be hydrating more than the

total hair, or the overlapping cells of the cuticle could be opening up after immersion, increasing the space between them. The experiments outlined in this proposal will not elucidate this mechanism. However, hydration is occurring to a large degree at the cuticle surface.

As stated before, the preliminary work could have been tainted by poor sample preparation. Individual hairs may exhibit different properties depending on race, genetics, diet, health, hair-care, *etc.* Therefore, we will compare samples obtained from the same subject in order to determine reproducibility. Also, the areas imaged will be constant throughout this sampling. For instance, we will only compare data taken from samples that were ~ 1 inch from the scalp.

Hair could be more susceptible to damage when wet than when dry. At first, this seems counterintuitive since we consider hair to be more manageable, easier to comb, *etc.* when it is wet. However, if we recall that hair is a complex composite of protein fibers and keratinized cells, it may be possible that adding water may hydrate these fibers and weaken their three-dimensional structure.

It would be advantageous to protect the cuticle from hydration while the hair is immersed, for instance during swimming and bathing. If a conditioner or hair treatment could be devised that inhibited step height increase, it could act as a protective coating. Currently, the effectiveness of these chemical treatments is determined based on the macroscopic properties of hair. This method is adequate if all the information needed pertains to the final softness/coarseness of the hair. However, if "healthy" hair is the desired quality, quantitative information about relative sheath height changes may be more pertinent. For instance, a conditioner may act as an excellent softener due to macroscopic viscosity properties but may do nothing to coat the imbricated cells and thus protect the hair from hydration.

REFERENCES

1. Montagna W. The Structure and Function of Skin. New York: Academic Press, 267 (1962).
2. Jurdana L. and Leaver I. Poly Inter. **27**,197 (1992).
3. Hess W., Seegmiller R., Gardner J., Allen J., Barendregt S. Scan. Micr. **4**, 375 (1990).
4. Binnig G., Quate C., Gerber C. Phys. Rev. Lett. **56**, 930 (1986).
5. Rugar D. and Hansma P. Physics Today **43**, 23 (1990).
6. Hansm H., Bezanilla M., Zenhausern F., Adrian M., Sinsheimer R. Nuc. Acids Res. **21**, 505 (1993).
7. Weisenhorn A., Drake C., Prater C., Gould P., Hansma P., Ohnesorge F., Egger M., Heyn S., Gaub H. Biophys. J. **58**, 1251 (1990).
8. Erie D., Yang G., Schultz H., Bustamante C. Science **266**,1562 (1994).

9. Parpura V., Haydon P., Henderson E. J. Cell Science **104**, 427 (1993).
10. Fritz M., Radmacher M., Gaub H. Biophys. J. **66**, 1328 (1994).
11. Topometrix Inc., Santa Clara, CA.
12. Baselt D., Clark S., Youngquist M., Spence C., Baldeschwieler J.RSI **64**, 1874 (1993).
13. Leveque J., Garson J., Pissis P., Boudouris G. Biopolymers **20**, 2649 (1981).
14. Matoltsy G. The Chemistry of Keratinization. In: Montagna W, Ellis R, eds. The Biology of Hair Growth. New York:Academic Press Inc., 135 (1958).
15. Pohl S., Hnatchenko M., Feinland R. Hair conditioning composition and method for use. U.S. patent **4507280**, (1985).
16. Garcia M. *et al.* J. Soc. Cosmetic Chem. **27**, 379 (1976).
17. Hess W., Flinders J,, Pritchett C., Allen J. J. Mamm. **66**, 75 (1985).

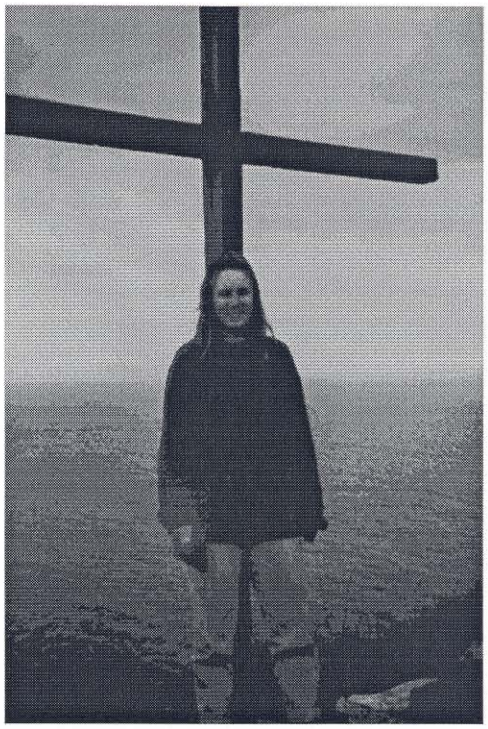

Kim Komisarek is an undergraduate at Caltech and my collaborator on this project.

CHAPTER 3 - Surface Microstructure of $Zr_{41.25}Ti_{13.75}Cu_{12.5}Ni_{10.0}Be_{22.5}$, a Bulk Metallic Glass

The surface of $Zr_{41.25}Ti_{13.75}Cu_{12.5}Ni_{10.0}Be_{22.5}$, a bulk metallic glass, has been imaged using atomic force microscopy. The samples were spherical ingots ranging in size from 2.5 - 10 mm in diameter, prepared by RF induction melting. The untreated surfaces were very smooth -- features were no higher than 3 nm over a 10 x 10 μm region, comparable to many polished surfaces. Two types of microstructure were also observed; in some samples, periodic striations forming either a striped or a checkered structure were present, with wavelengths between 1 and 2 μm, and amplitude of approximately 2 nm; in other cases, 'cracked mud'-like patterns were observed. These microstructures could be related to strain induced surface roughening; preliminary calculations are presented that are consistent with this hypothesis.

INTRODUCTION

Recently, Peker and Johnson discovered a class of easily processible metallic glasses.[1] These glasses require cooling rates of 10 °K/sec or less, orders of magnitude slower than traditional metallic glasses and can be heated well above the glass transition temperature without crystallization. These materials possess many technologically useful properties, including high strength/weight ratio, high wear resistance, low frictional coefficient, and high corrosion resistance. Previous metallic glasses require thin film processing and crystallize below the glass transition temperature, T_g, limiting their applications. These new metallic glasses can be manufactured with dimensions thicker than an inch and processed above T_g. These properties increase substantially the usefulness of metallic glasses.

The correlation between topography, surface chemistry, and friction in these metallic glasses is under investigation in our laboratory. This report presents the topographic results obtained using atomic force microscopy. Three types of surface structures have been observed:

1. Disordered regions with roughness smaller than 3 nm.
2. Periodic 'stripes' and checkered patterns with wavelengths between 1 - 3 μm and amplitudes between 2 - 3 nm.
3. Regions that appear as 'cracked mud-like' patterns.

EXPERIMENTAL DETAILS

The samples were bulk metallic glass (BMG) ingots of $Zr_{41.25}Ti_{13.75}Cu_{12.5}Ni_{10.0}Be_{22.5}$, ranging in size from 2 - 10 mm in diameter. They were prepared by induction melting on a water-cooled silver boat under a titanium gettered argon atmosphere. X-ray diffraction showed broad peaks characteristic of amorphous materials. High resolution TEM on similar samples showed no ordered features larger than 1.2 nm. X-ray photoemission spectroscopy studies have shown the presence of an oxide surface composed of Zr, Ti and Be.[2] The samples looked very shiny and smooth to the naked eye. The smaller samples were mounted on steel washers with 5-minute epoxy. Larger samples were first sectioned with a diamond saw in oil, washed in an ultrasonic cleaner (acetone/methanol/DI water sequence), then mounted as before.

The atomic force microscope (AFM) has been used as a very sensitive tool for imaging flat surfaces, even on an atomic scale.[3,4] To image using AFM, a cantilever with a small pyramidal tip is placed over the sample and lowered into mechanical contact. A tube piezoceramic is then used to scan the tip over the sample. The deflection of the cantilever corresponds to changes in height of the sample. These motions are monitored by reflecting a laser beam from the cantilever and onto a position sensitive photodiode. The lateral or frictional force can also be determined by using a four-quadrant detector.[5]

A Topometrix AFM system with in-house software was used in contact mode for all of these experiments.[6,7] All of the images were taken in air with standard pyramidal tips Si_3N_4; two scanners were used, a 10 μm tube scanner and a 75 μm pivoting scanner. The samples imaged were unusual for AFM due to their relatively large height and small radius of curvature. All of the samples studied in this report were at least 2 mm high; metal spacers were used to lower the scanning stage to accommodate the large sample height. The Topometrix instrument is equipped with a video camera that images the tip-sample interface at a 45° angle. It was straightforward to position the tip at the apex of the samples by noting the reflection of the light off the sample as it was translated. Prior to imaging, all of the samples were rinsed with acetone/methanol/deionized water, then blown dry with pressurized air to remove excess surface contaminants.

A total of 9 BMG samples prepared by RF induction melting were studied. This technique is performed as follows:

- metal ingots are placed in a water cooled silver boat that is surrounded by a large coiled wire
- a high-current RF signal is passed through the wire; this current induces a large magnetic field in the area of the sample
- the field induces eddy currents in the ingots raising their temperature well above the melting temperature
- once equilibrium has been reached (the alloy is formed), the current is turned off
- the sample cools mainly by conduction with the silver boat

For comparison, a crystalline sample of different composition and a sample made by electrostatic levitation were also imaged. The results presented are from three of the RF levitated samples. Sample I was the top region of a large ingot (~ 10 mm in diameter) that had been sectioned. Sample II was a small spherical ingot (~ 3.5 mm in diameter). Sample III was also spherical (~ 2.5 mm in diameter). All of the images presented were acquired at a scan rate of 4 lines/second and 250 pixels/line, although the scanning rate was varied to check for imaging artifacts. We also zoomed in on features, changed the scanning direction, and rotated some of the samples to verify that the observed features were reproducible.

RESULTS

Figure 1A is an image of the top surface of sample I. As seen in the linecut (Figure 1B), the surface features are no more than 3 nm over the 10 x 10 μm region. No repeating patterns are present. The surface is remarkably flat, since no polishing was performed.

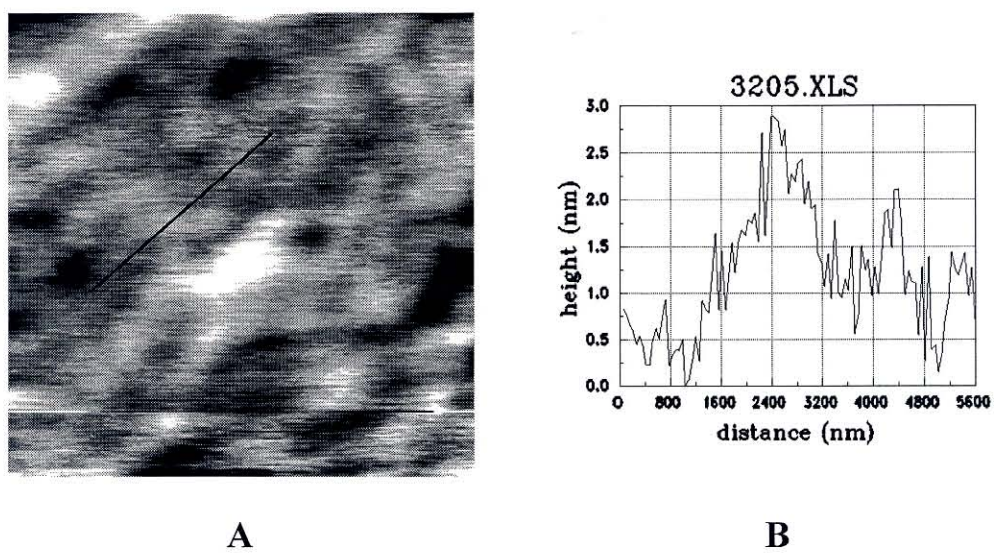

Figure 1: A - a 10 x 10 μm AFM image of Sample I; the data has been line leveled only. This area is relatively flat with no repeating features. **B** - AFM linecut; the plot represents the quantitative height data along the line drawn in A. Even the large feature just below the linecut is only 2 nm in height.

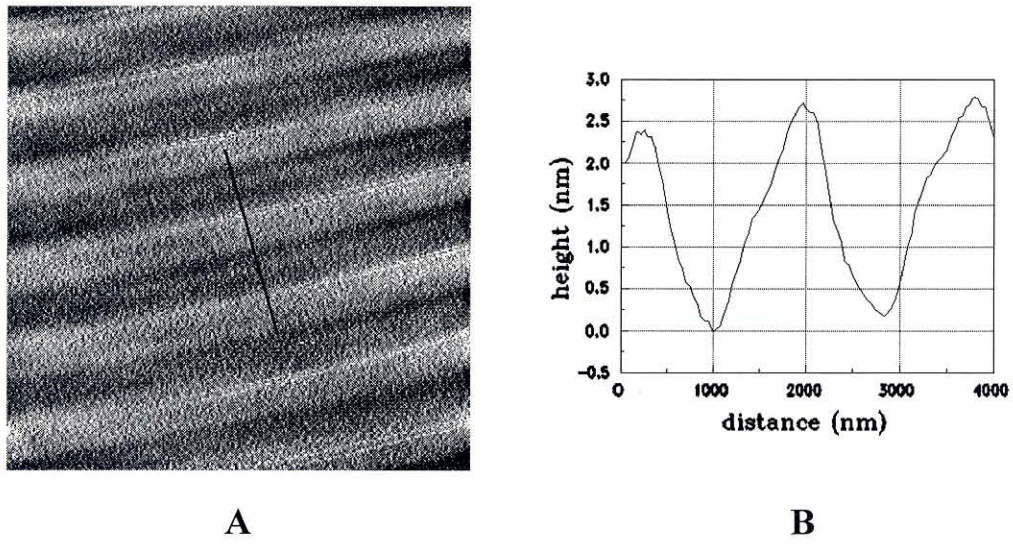

Figure 2: A - a 10 x 10 μm AFM image of sample II; notice the periodic corrugation.
B - the linecut shows that the wavelength of the corrugation is ~ 2 μm with an amplitude ranging between 2 - 3 nm.

Figure 2A is a 10 x 10 μm image of sample II. The figure shows an unexpected striped pattern. These stripes have wavelengths slightly less than 2 μm and amplitudes ranging from 2 - 3 nm (see Figure 2B). In some regions, smaller wavelengths are also observed (Figure 3A), as well as cross-hatched structures (Figure 3B).

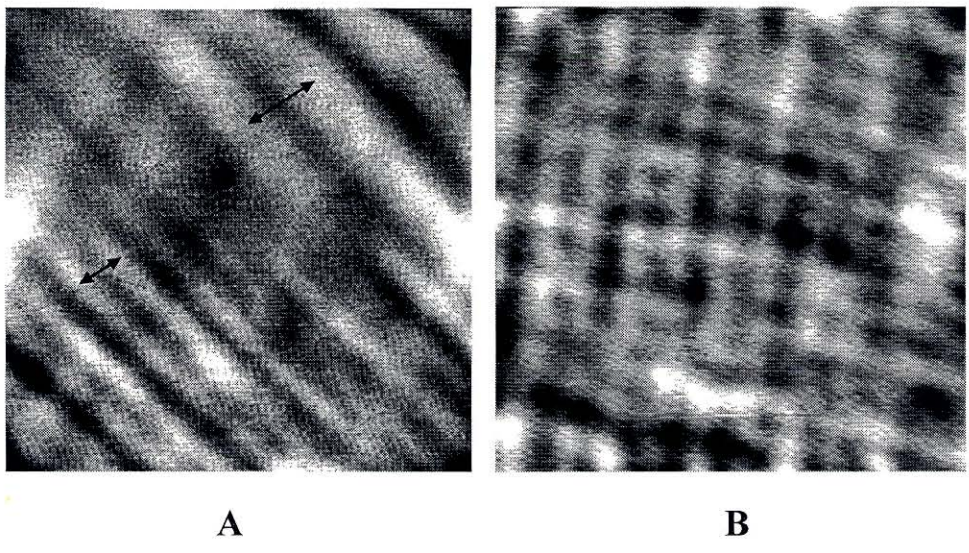

Figure 3: **A** - a 10 x 10 μm AFM image of a different area of sample II; two wavelengths are present, with one roughly half the size of the other; **B** - a 10 x 10 μm AFM image of sample II showing a cross-hatched pattern; the wavelength is ~ 0.8 micron.

Figure 4 is a 50 x 50 μm image of sample III. The wavelength and direction of the corrugations are variable over this distance. The other features are probably surface contaminants.

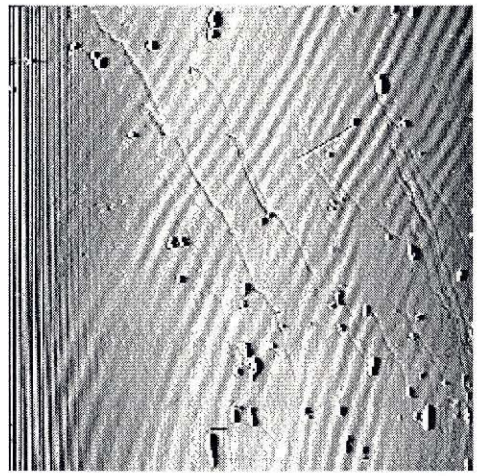

Figure 4 - a 50 x 50 μm AFM image of sample III. The wavelength and direction shift slightly over this large area. The bright spots are probably surface contaminants. The image is shown twice after two different processing techniques; the data is identical.

Figure 5 is a 4.5 x 4.5 μm image of sample II. Notice the cracked mud-like pattern that is present, as well as the small aggregates (~ 100 nm) that are formed.

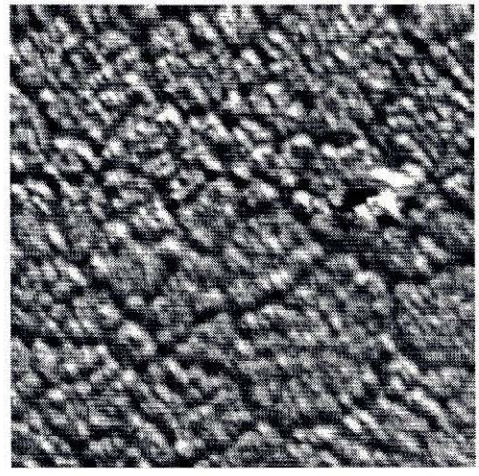

Figure 5 - a 4.5 x 4.5 μm region of sample II; a cracked mud-like pattern is present in this region.

Some type of periodic corrugation was present in 6 of the 9 samples; the 'cracked-mud-like' patterns were observed in 8 out of 9 samples. Since only the top portion of the samples could be imaged, it is impossible to elucidate how extensively these features cover the sample surface. The periodic structures were present only in the small samples -- the largest sample did not show any periodicities. Also, the partially crystallized sample and the electrostatically levitated sample (which was cooled more slowly than the induction melted samples) did not show any regular corrugations.

DISCUSSION

All of the samples prepared for this report showed remarkably smooth surfaces. No polishing or 'high-tech' preparation was required to produce surfaces with nm roughness over 10 μm regions.

However, the surfaces did exhibit very interesting structure on the nm scale. Most interesting was the periodic corrugations that were observed in 6 of the samples. We hypothesize that the stripes could arise from the relief of the stress.

Using continuum mechanics, it has been shown that when an elastic body with a flat surface is non-hydrostatically (uniaxially or biaxially) stressed, the surface can be unstable.[8-16] Undulations may grow with wavelengths that are governed by the competition between stress relaxation and surface tension or gravity. This phenomenon has been referred to as strain induced surface roughening or Grinfield instability. The most unstable wavelength (*i.e.* the wavelength that will be observed) will depend on whether matter is transported across the surface by diffusion or evaporation/condensation.

Linear stability analyses defines a critical wavelength by:[9,12]

$$\lambda > \lambda_o = \pi\gamma/M\sigma^2,$$

where γ is the surface tension and σ is the applied stress. The factor M depends on the boundary condition: for a plane stress, $M = 1/E$; for a plane strain, $M = (1-\upsilon^2)/E$, where E is Young's modulus and υ is Poisson's ratio.

The dominant mass transport mechanism will determine the critical wavelength, λ_m. For transport by surface diffusion, $\lambda_m = (4/3)\,\lambda_o$; for evaporation/condensation, $\lambda_m = 2\,\lambda_o$.

It is problematic to calculate the exact value for λ_m in this system. However, an order-of-magnitude calculation is instructive.

In order to solve for σ, the following approximations are used: E = 93 GPa, $\upsilon = 0.3$ [17] and $\gamma = 1.0$ J/m^2;[18] $\lambda_m = 1.5$ μm is the observed wavelength. A stress (σ) of 0.5 - 0.6

GPa is needed to create the observed instability, depending on whether the plane strain or plane stress boundary conditions are used. A stress of 0.5 GPa corresponds to ~ 0.5% strain at room temperature.[17]

Most of the non-hydrostatic stress in these samples should be due to thermal stress. The sample is cooled mainly by contact with the bottom region of the silver holder, causing a temperature gradient from the top to the bottom. In addition, the surface of the sample cools before the interior. Assuming that the mass transport at the surface is large enough only near and above the glass transition temperature (T_g= 350°C), and the sample cools through a δT of 300-500°C, a coefficient of thermal expansion of 1.0-1.7 x 10^{-5}/°C produces a 0.5% strain. Preliminary measurements indicate that the coefficient of thermal expansion at T_g is approximately 9 x 10^{-4}/°C, and 2 x 10^{-5}/°C above T_g.[19] The Young's modulus, Poisson ratio, and surface tension are not yet rigorously known for this material near T_g; however the values used in the calculation should be within a factor of 2 of the true values.

Assuming surface diffusion to be the dominant mass transport mechanism, a diffusion constant of 10^{-13} - 10^{-14} m^2/sec is required for atoms to travel a few μm in ~ 10 seconds. The bulk diffusion constant for Be is 10^{-18} m^2/s near Tg for this alloy.[20] In crystals, surface and grain boundary self-diffusion constants are 6 - 8 orders of magnitude larger than in the bulk near the melting temperature (T_m) (T_g ~ (2/3)T_m for these BMG's). Therefore, it is quite plausible that the surface diffusion constant is large enough for the instability to occur near T_g.

Similar corrugations were observed in solid He as it was quenched over a few millidegrees,[21] although the wavelength observed (mm's) corresponded to the low stress limit of the instability, in which gravity was the dominant opposing factor. Interestingly, the corrugations in helium disappeared once the temperature was restabilized.[21] Further studies using piezoelectric transducers confirmed that the corrugations were stress induced.[22] Thin films of InGaAs on GaAs[23] and Si/Ge [16,24,25], where lattice mismatch causes stresses of a few GPa, have also exhibited Grinfield instability. Crack-like corrugations were observed in a crystallized polymer, and the authors speculated that the stress was due to the preferential orientation of the crystallization.[26]

Since surface diffusion in these materials has not yet been measured, this hypothesis is still speculative and requires further systematic measurements of both the surface diffusion constant and the dependence of the wavelengths observed on various parameters. The fact that periodic structures were not seen in the largest samples is consistent with our model, since the slower cooling rate would induce a much smaller stress. Similarly, the electrostatic levitated samples, which were 2 mm in diameter but cooled at approximately 1-2 °K/sec did not show any regular corrugations.

It is possible that the stress is due to a mismatch between the oxide layer and the bulk, rather than thermal stress. This can be addressed by making samples in UHV and imaging *in situ*, with a controlled introduction of oxygen.

It is also not clear how the observed half-wavelengths and cross hatching can be accounted for by the current hypotheses, other than that the stress may not be truly uniaxial and could contain multiple vector components. In addition, we have not yet determined what causes the preferred orientation of the stripes.

A few other possible causes for the periodic corrugations were explored and found to be inconsistent:

1. X-ray microprobe analysis of these samples failed to detect any variations in the composition of Zr, Ti, Cu or Ni within the resolution of the instrument (2%). This result seems to eliminate the possibility that local chemical differences cause the corrugations.

2. Samples were synthesized while vibrating the RF levitation container at 60Hz (as well as its harmonics); no correlation was found between the vibration frequency and the presence of the periodic corrugations.

3. The capillary and gravity wavelengths for this material are at least a few millimeters, well above the observed wavelengths.

4. The periodic corrugations resemble interference fringes; the AFM uses an optical beam alignment to detect small cantilever deflections. However, it is difficult to see how the the experimental geometry could produce corrugations similar to those observed. In addition, these fringes would be present in all shiny, curved samples imaged, since stray reflections are hard to avoid. The periodic corrugations only appeared in some samples.

It is unclear at present what causes the crack-like mud patterns. They may be related to the oxidation process, since these structures were more prevalent in samples that were imaged a few months after synthesis. There have been suggestions that Grinfield instability is a precursor to crack formation.[12,27] If this observation is correct, then the cracked-mud-like patterns in these samples could be another manifestation or a more evolved version of the instability. However, these patterns have been observed in both fresh samples and older samples (a few months), as well as coexisting with the periodic ripples. Clearly, more systematic studies are required.

CONCLUSION

The surfaces of the bulk metallic glass $Zr_{41.25}Ti_{13.75}Cu_{12.5}Ni_{10.0}Be_{22.5}$ has been imaged with AFM. The surfaces are remarkably flat, with surface features no higher than 3 nm over a 10 μm region. In some cases, surprising periodic corrugations and cracked-mud-like patterns were observed. A plausible source for these features is strain induced surface roughening or Grinfield instability due to the relief of non-hydrostatic thermal stress.

ACKNOWLEDGMENTS

Co-authors on this paper were M. La Madrid, A. Peker and W. Johnson. The authors would also like to acknowledge useful conversations with M. Cross, B. Spencer, and D. Meiron.

REFERENCES

1. Peker A. and Johnson W. Appl. Phys. Lett. **63**, 2342 (1993).
2. LaMadrid M., Peker A., Housley R., Rice A., Johnson W. to be published.
3. Binnig G., Quate C., GerberC. Phys. Rev. Lett. **56**, 930 (1986).
4. Albrecht T., Quate C., J. Appl. Phys. **62**, 2599 (1987).
5. Meyer G. and Amer N. Appl Phys. Lett. **57**, 2089 (1990).
6. Topometrix, Santa Clara, CA.
7. Baselt D., Clark S., Youngquist M., Spence C., Baldeschwieler J. RSI **64**, 1874 (1993).
8. Asaro R. and Tiller W. Met. Trans. **3**, 1789 (1972).
9. Srolovitz D. Acta. Metall. **37**, 621 (1989).
10. Nozieres P. J. Phys. I France **3**, 681 (1993).
11. Grinfield M. Sov. Phys. Dokl. **31**, 831 (1987).
12. Yang W. and Srolovitz D. Phys. Rev. Lett. **71**, 1593 (1993).
13. Spencer B., Voorhees P., Davis S. Phys. Rev. Lett. **67**, 3696 (1991).
14. Freund L. and Jonsdottir F. J. Mech. Phys. Solids **41**, 1245 (1993).
15. Gao H. J. Mech. Phys. Solids **39**, 443 (1991).
16. Tersoff J. and LeGoues F. Phys. Rev. Lett. **72**, 3570 (1994).
17. Bruck H., Christman T., Rosakis A., Johnson W. Scr. Met. Mat. **30**, 429(1994).
18. The surface tensions of the the component metals range from 1-2 J/m^2 at their respective melting points; Brandes E. and Brook G. eds. Smithells Metals Reference Book, (1992).
19. Bakke E. and Johnson W. private communication.
20. Geyer U., Schneider S., Johnson W., Tombrello T., preprint, (1995).
21. Bodensohn J., Nicolai K., Leiderer P. Z. Phys. B **64**, (1986).
22. Torii R. and Balibar S. J. Low Temp. Phys. **89**, 391 (1992).

23. Venables J., Spiller G., Hanbucken M., Rep. Prog. Phys. **47**, 399 (1984).
24. Jesson D., Pennycook S., Baribeau J., Houghton D. **71**, 1744 (1993).
25. Cullis A., Robbins D., Pidduck A., Smith P., Mat. Res. Soc. Symp. Proc. **280** (1993).
26. Berrehar J., Caroli C., Lapersonne-Meyer C., Schott M. Phys. Rev. B **46**, 13487 (1992).
27. Spencer B. and Meiron D. Act. Met. Mat **42**, 3629 (1994).

CHAPTER 4 - Active Noise Reduction in Atomic Force Microscopy: Gamble Mode

Active noise reduction has been accomplished in atomic force microscopy by applying a high frequency, low amplitude vibration to the cantilever while it is in contact with a surface. The applied excitation (> 200 kHz; ~ 1 nm) is acoustically coupled to the tip and dampens the resonance Q factors of the system. The applied frequency is well above the bandwidth of the acquisition system (50 kHz). We call this mode 'Gamble Mode' or 'resonance-contact'. The non-linear behavior of the tip-sample interaction allows the high frequency excitation to effectively decouple the resonance vibrations.

INTRODUCTION

Active noise reduction is of interest for any analytical instrument and crucial in certain environments. Mechanical noise can induce unwanted signals in atomic force microscopy measurements, limiting the resolution and scan speed. In this report, a method for reducing mechanical noise in atomic force microscopy (AFM) is demonstrated; this technique is easy to implement with minimal instrumentation.

The use of atomic force microscopy (AFM) in a dynamic mode was first demonstrated by Martin *et al.* in 1987.[1] This "resonance non-contact" mode is implemented as follows: the cantilever is vibrated at its first resonance frequency (ω_o). As the tip approaches the sample, the tip-sample interaction produces a force gradient that shifts the resonance frequency of the cantilever:

$$m^* \omega_{new}^2 = k_{new} = k_o - \frac{\partial F}{\partial z},$$

where k is the spring constant, m* is the effective mass, ω is the resonance frequency, and z is the tip-sample separation. Since the driving frequency (ω_o) is not equal to the new resonance frequency of the cantilever (ω_{new}), the amplitude of the vibration is lowered and can be used as a feedback signal. This technique effectively negates the lateral force that is present in normal contact mode imaging. However, this strategy requires special cantilevers and lock-in electronics.

Recently, resonant non-contact mode imaging was demonstrated in water with cantilevers having relatively weak spring constants (0.5 N/m).[2,3] Also, ultrasonic detection has been used in conjunction with AFM to detect cantilever movements in the MHz regime.[4]

In this report, a simple method for reducing low frequency noise in DC AFM experiments is demonstrated. While the cantilever is in contact with the sample, the base of the cantilever is mechanically driven at a high frequency. At certain frequencies, the overall mechanical noise of the system is lowered. No special instrumentation is required for this mode other than a function generator to vibrate the cantilever at high frequency and a piezoceramic to couple the excitation into the cantilever-sample system. We refer to this technique as "resonance contact" or "Gamble Mode" (GM). A mechanism based on non-linear coupling between the tip and sample is presented to explain this phenomena.

EXPERIMENTAL

A Topometrix Discoverer AFM with in-house software was used for the experiments in this report.[5,6] This system uses an optical lever detection scheme to monitor the cantilever displacement. In order to determine the frequency characteristics of the cantilever motion, the output of the photodiode preamplifier was connected directly to a HP spectrum analyzer. Standard 200 μm, thin arm triangular cantilevers were used for all of the experiments ($k = 0.1$ N/m, $\omega_0 \sim 20$ kHz).

The software uses a proportional-integral-differential (PID) feedback algorithm to maintain constant cantilever deflection. The feedback parameters determine the response time of the instrument; higher values will produce shorter response times. However, if the gains are increased above a certain threshold, the feedback will oscillate. This threshold is one of the factors limiting the maximum scan speed.

In order to vibrate the cantilever, the tip mounting system was attached directly to a small dither piezoceramic (labeled GM piezo A in Figure 1). This base-plate was initially designed to be used in resonance non-contact mode. For the liquid experiments, a piezoceramic was glued between the AFM head that houses the tip/detector and the base which houses the sample. Driving this piezo was also effective at coupling vibrations to the cantilever. This piezo will be referred to as GM piezo B. A function generator was used to apply the driving signal.

Three imaging conditions were analyzed: clean samples in air, oily samples in air, and clean samples in water. The oily sample was studied in order to determine the meniscus effect when GM was used in air. The sample was smeared with a small amount of vacuum pump oil; the oil was then wiped off with a Kimwipe before the tip was brought into contact.

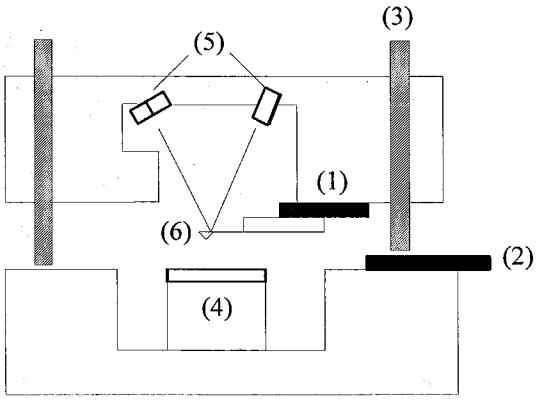

Figure 1: Schematic of the GM setup. Two piezos can drive the GM frequency: (1) GM piezo A or (2) GM piezo B; (3) approach screws; (4) sample tube scanner; (5) feedback laser and photodiode; (6) cantilever.

RESULTS

Typical Noise Spectrum

Figure 2 is a noise spectrum when the cantilever is in contact with a Compact Disk (CD) that had been smeared with oil. Two specific noise peaks are present in this experiment: 4 kHz and 14 kHz (and overtones). The 4 kHz noise changes amplitude as

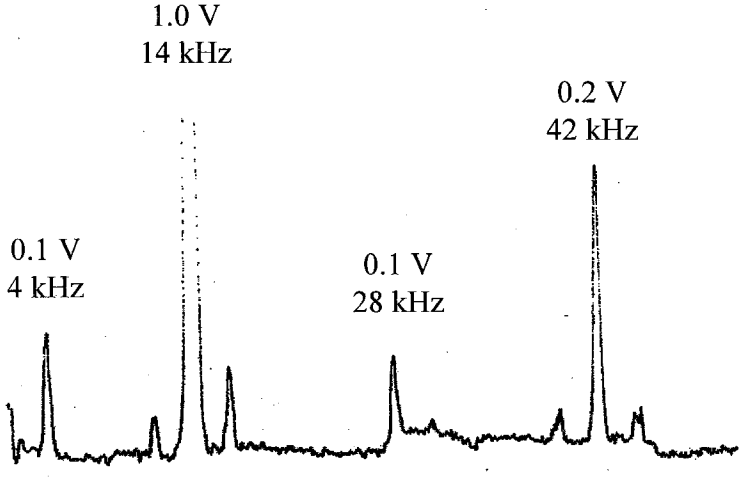

Figure 2: typical noise spectrum; the integral gain is set ~ 12 times higher than the optimal value; the 14 kHz noise is a mechanical resonance; the 28 kHz noise is probably an overtone of the 14 kHz; the values of the amplitudes are labeled in the graph.

the feedback gains are altered but does not shift in frequency. A change in imaging conditions may shift this frequency slightly. For example, changing the meniscus from oil to water shifts this frequency to ~ 2.7 kHz. However, using a new cantilever, sample, or setpoint does not shift this frequency. There is also a mechanical resonance at 14 kHz; this noise varies in amplitude and frequency for different tips and samples.

In order to determine the sources of these peaks, the feedback parameters were altered. As the integral gain was increased, the 4 kHz signal increased in amplitude. As the setpoint was lowered (corresponding to less deflection of the cantilever, less tension), the higher frequency noise increased. Therefore, the high frequency noise is attributed to a mechanical resonance and the 4 kHz noise to a feedback loop resonance.

No particular sources of room noise are present between 1 - 20 kHz, within the detection limits of the system. Therefore, the large noise peaks that are observed when in contact must arise from structural modes with very large quality factors (Q).

The noise level in Figure 2 is actually very high for this instrument; typical ambient noise is ~ 10 mV total. However, to demonstrate the power of this technique, a particularly noisy tip-sample system is presented.

Very similar spectra have been obtained with numerous tips and samples. The feedback resonance does not shift appreciably. The mechanical noise shifts from 12 - 20 kHz, depending on the tip, sample, and scanner. Also, GM is effective even when the initial noise is fairly low, for example 10 mV of total noise prior to GM can be lowered to the white noise level (<< 1 mV).

Gamble Mode

Figure 3 is a spectrum of the noise in Figure 2 after GM had been initiated at 361 kHz on GM piezo A. The same results were obtainable when GM piezo B was used at the same frequency. Notice the different vertical scales. The low frequency noise has been lowered three orders of magnitude. When the initial mechanical noise is more

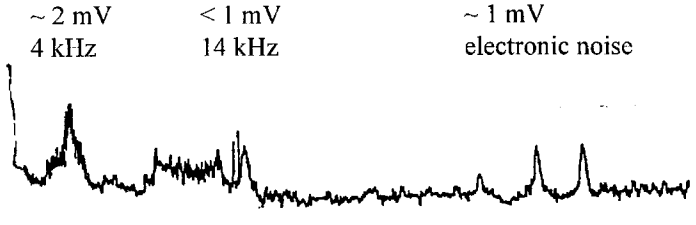

Figure 3: noise in Figure 1 after GM is initiated at 361 kHz; notice the new scale; the small peaks above 30 kHz are electronic noise.

reasonable than in Figure 2 (~ 10 - 100 mV initial noise), the noise can be totally eliminated (within the detection limits of the spectrum analyzer).

The effectiveness of GM is extremely frequency dependent. Certain GM frequencies have no effect on the noise. An interesting observation is that the noise frequencies can be selectively decoupled; for example when GM was shifted from 361 kHz to 342 kHz, the 14 kHz noise was totally eliminated, but the 4 kHz noise was not altered. Other GM frequencies lower the amplitude of the high frequency noise while actually raising the amplitude of the low frequency noise.

The output of the photodiode was simultaneously monitored on an oscilloscope, since the spectrum analyzer was not capable of monitoring signals above 50 kHz. Effective GM frequencies also produce a small AC signal at the same frequency. In Figure 3, a 30 mV peak-to-peak signal at 361 kHz was present, corresponding to a 2.5 nm amplitude on the cantilever. As the GM driving amplitude was lowered, so was this 30 mV signal. Below a certain level, the 361 kHz signal remained (~ 10 mV or 0.8 nm), but the GM effect no longer lowered the noise.

A GM vibration amplitude of at least 1 nm is required to be effective; typically, 2 - 3 nm p-p is used. Larger amplitudes are also effective.

GM has been successfully implemented with numerous tips, samples, and scanners. The same trends were observed when the meniscus layer was altered from oil to water. GM is also effective when imaging was done completely under water in a standard liquid cell.

Driven Noise

In order to explore the mechanism responsible for GM, noise was systematically introduced into the system. To simulate noise, GM piezo B was vibrated at a low frequency; the tip-sample separation was modulated at that frequency, mimicking noise.

GM piezo B was scanned between 0-3 kHz. A small resonance (Q ~ 2) was found at 1.9 kHz. There was no apparent resonance at 2.8 kHz (*i.e.* the noise at 2.7, 2.8, 2.9, *etc.* was identical). GM piezo A was then used to initiate GM. The GM frequency was scanned in order to attempt to dampen both frequencies. Figure 4 is the superposition of the 4 spectra; the x axis is not to scale. It was impossible to lower the noise at 2.8 kHz an appreciable amount (60 mV to 50 mV). However, the 1.9 kHz was lowered with a GM of 335 kHz from 150 mV to 50 mV. No GM frequency could lower the 1.9 kHz noise below 50 mV.

From these results, we conclude that the GM piezo produced a driving vibration of 50 mV on the cantilever. Both the 1.9 and 2.8 kHz peaks could only be lowered to this value. Since the 1.9 kHz signal had a larger initial Q, it was lowered a larger amount.

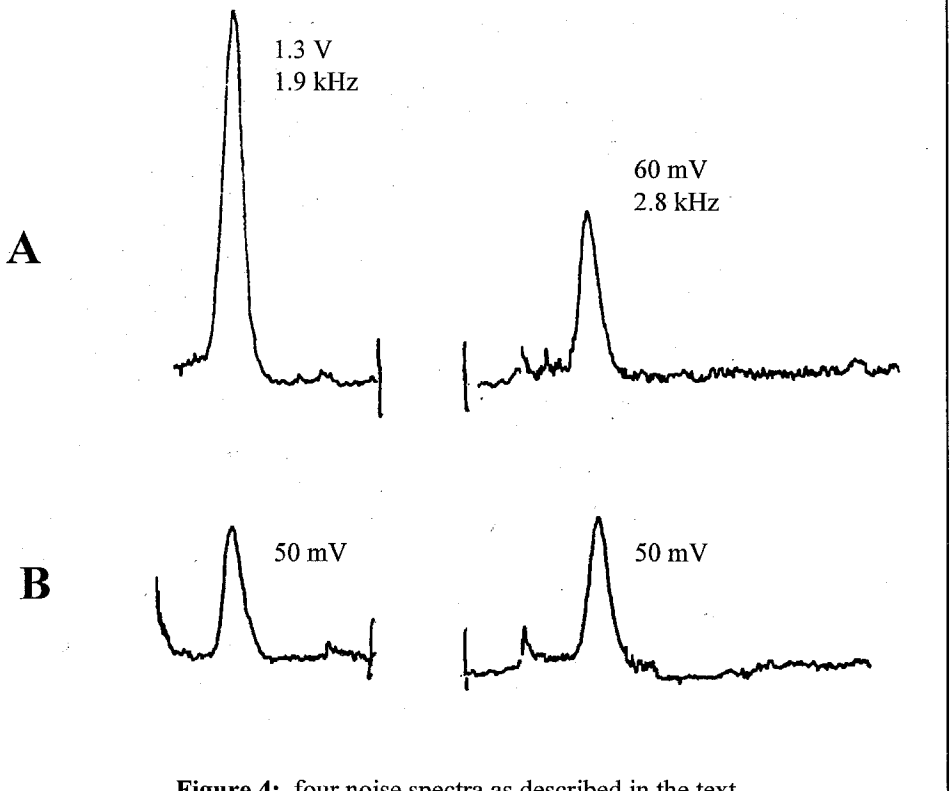

Figure 4: four noise spectra as described in the text.

The 2.8 kHz noise had a very small Q and could only be lowered to the driving amplitude. Therefore, GM loweres the Qs of the structural resonances. It does not decouple vibrations. If GM was decoupling vibrations, it should be possible to lower noise even if the Q is 1.

It was much more difficult to find an effective GM frequency for these two driven noises than in the situation where the normal strucutural modes were excited by the background noise (4 and 14 kHz in Figure 2).

IMAGING EXAMPLES

Figure 5 was taken with the integral gain set ~ 18 times higher than optimal. This high feedback gain allowed the image to be acquired very quickly, 12.5 lines per second and 250 pixels per line. The noise values prior to GM were 1.0 V at 15kHz, 300 mV at 90 kHz, and 60 mV at 3 kHz; with GM on at 375 kHz there was only a 10mV - 3 kHz signal. GM was initiated at the beginning and end of the scan and turned off in the middle. Notice the noisy signal between these two points. The linecuts show that the true features of the CD pit are not resolved without GM.

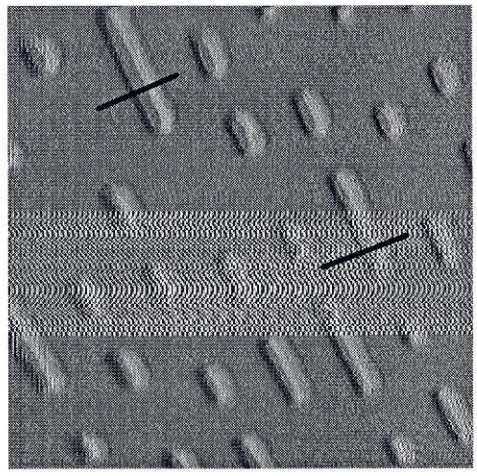

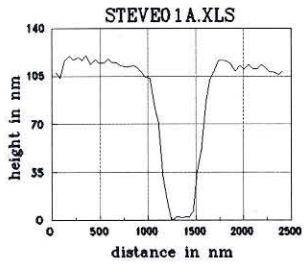

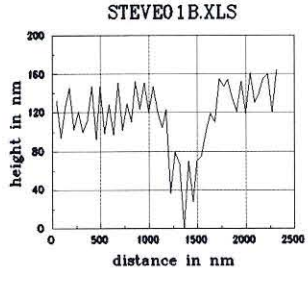

Figure 5: a 10 x 10 mm AFM of a CD; GM was initiated at the beginning and end of the scan. Notice the features are unresolvable when GM is off.

Low frequency noise (< 1 kHz) has also been effectively eliminated while imaging.

Figure 6 is a high resolution image of a bare silicon wafer. Once GM is initiated, smaller features become apparent. Also, streaking occurs in some images. This streaking has not been observed with GM. The noise level was 2 orders of magnitude larger in the image prior to initiation of GM.

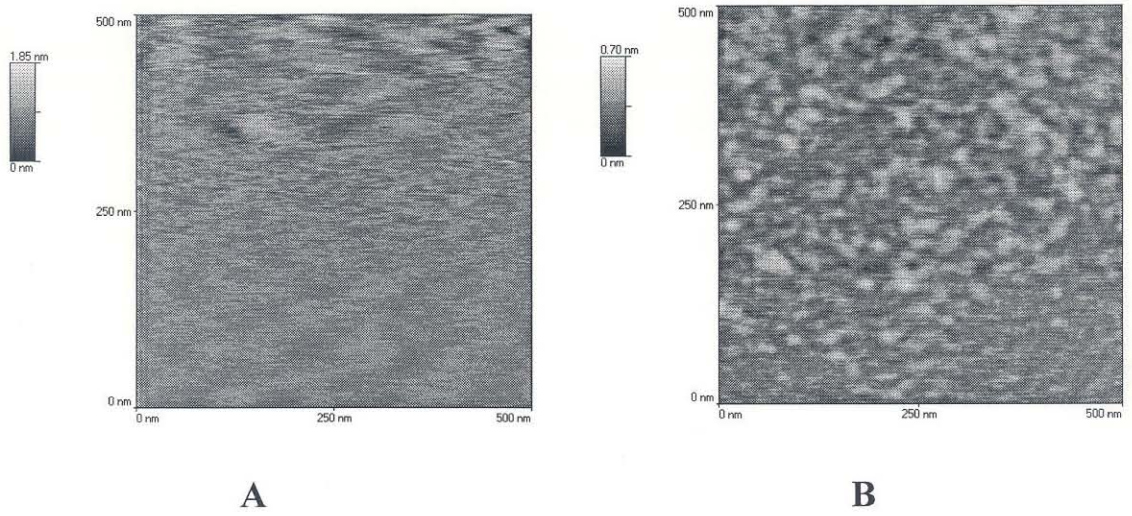

Figure 6: 500 x 500 nm AFM images of a bare silicon wafer; **A** -prior to GM; **B** - GM on.

DISCUSSION

The observed noise peaks are resonance frequencies of the system while the cantilever is in contact with the sample. These peaks have very large Q's. Even while in constant contact, the cantilever will be coupled to these vibrations.

If a vibration is excited in a completely harmonic system, the resulting motion will reflect the displacements characteristic of the normal mode which is excited. No coupling occurs between normal modes. However, the harmonic approximation is only valid for very small vibrational amplitudes. As these amplitudes increase, the non-linear terms of the force equation will become significant and the system will behave anharmonically:

$$F = -kx - ax^2 - bx^3 - \ldots ,$$

where k is the spring constant, x is the displacement, and a, b, ... are constants. As x becomes large, the higher order terms become significant.

When GM is initiated, a finite amplitude (1 - 2 nm) is applied to the cantilever; this vibration causes anharmonic excitation of the system. This anharmonic excitation may allow coupling between the normal modes of the system, broadening the frequency characteristics and lowering the Q values at any particular resonance frequency. GM requires that a finite amplitude be applied in order to probe the anharmonic regime of the potential. This assertion is observed experimentally.

Certain GM frequencies have no effect since they do not effectively couple the vibration of the dither piezo into the cantilever. A GM frequency is required that is a resonance of the system, so that the tip-sample system will have a sufficiently large amplitude to enter the anharmonic regime of the potential.

Another observation is that the GM frequencies that are effective are in the range of natural resonances of the cantilever. Rabe and Arnold calculated and measured the resonance frequencies for a rectangular cantilever and found many structural resonances between 100 -1000 kHz.[4] Similar values have also been calculated for triangular cantilevers.[7] These resonances will be shifted once the cantilever is in contact.

REFERENCES

1. Martin Y., Williams C.C., Wickramasinghe H.K. JAP **61(10)**, 4723-4729 (1987).
2. Putman C.A.J., Van der Werf K. O., De Grooth B. G., Van Hulst N. F., Greve J. APL **64(18)** 2454-2456 (1994).
3. Hansma P.K., Cleveland J.P., Radmacher M., Walters D.A., Hillner P.E., Bezanilla M., Fritz M., Vie D., Hansma H.G., Prater C.B., Massie J., Fukunaga L., Gurley J., Elings V. APL **64(13)** 1738-1740 (1994).
4. Rabe U. and Arnold W. Ann. Physik **3** 589-598 (1994).
5. Topometrix Inc., Santa Clara, CA.
6. Baselt D, Clark S, Youngquist M, Spence C, Baldeschwieler J. Digital signal processor control of scanned probe microscopes. *Review Scientific Instruments* 1993;64:1874-1882.
7. Chen G.Y., Warmack R. J., Thundat T., Allison D. P., Huang A. RSI **65(8)** 2532-2537 (1994).

CHAPTER 5 - Tip-Sample Interactions: Extraction of Single Molecular Pair Potentials from Force Curves

This report describes a method for extracting true tip-sample potentials from force curves in atomic force microscopy. These potentials are not the negative integrals of the observed force curve . Rather, the potential is a function of the cantilever deflection and cantilever spring constant. If information about the shape of the tip is known, a decorrelation may be performed to extract molecular pair potentials from the total tip-sample potential. Applications and limitations of this method are discussed.

INTRODUCTION

Accurate determination of molecular pair potentials is of great interest for molecular design and eventually nanotechnological applications. Atomic Force Microscopy (AFM) is capable of imaging surfaces with high resolution in a non-invasive manner.[1-3] To perform an AFM experiment, a flexible cantilever with a small protruding tip is brought into contact with a surface; as the tip is scanned, the interaction forces between the electron clouds of the atoms of the tip and the sample perturb the cantilever from its equilibrium position.

In addition to its imaging capability, AFM is also capable of measuring the force between the tip and sample as a function of tip-sample separation.[4] This "force curve" is completely analogous to Israchevilli's surface force experiments with a smaller contact area.[5]

Several models have been proposed to explain observed AFM force curves.[6-8] These models show poor agreement with experimental data. One error that is inherent in these models is that the force curve is assumed to be related to the interaction potential by:

$$F_{meas}(r) = -\frac{d}{dr}V(r), \qquad [1]$$

where r is tip-sample separation and V(r) is the potential. However, a force curve does not record the force as a function of tip-sample distance. Rather, it monitors the force versus the separation of the cantilever base and the sample. Equation [1] is only correct when the cantilever base and the tip do not move with respect to each other, which is true only in the limit of an infinite cantilever spring constant.

The chemical nature of the tip and sample must also be considered when interpreting force curves. The potential between tip and sample will be primarily due to the interactions of the surface atoms.[9] Controlled experiments confirm that the surface chemistry dominates the shape of the force curves.[9-11]

In this report, a thorough analysis of the AFM sample-tip-cantilever system will be presented. An accurate expression for the relationship between the force curve and the actual tip-sample potential will be derived. These results will be compared to the standard method of force curve interpretation by numerical simulation.

A chemical model of AFM tip-sample interaction will also be developed. This model analyzes the relation between the tip shape, intermolecular potential, and the total potential between tip and sample. Single intermolecular pair-potentials will be extracted from the total tip-sample potential, and the applications and limitations of applying this method to real experimental data are discussed.

EXTRACTION OF ACCURATE TIP-SAMPLE POTENTIALS FROM FORCE CURVES

Theoretical model (Analytical)

The sample-tip-cantilever system will be modeled by replacing the cantilever with a spring of spring constant k. In Figure 1, the cantilever deflection is $(z - D - c_{eq})$, where c_{eq} is the equilibrium length of the spring.

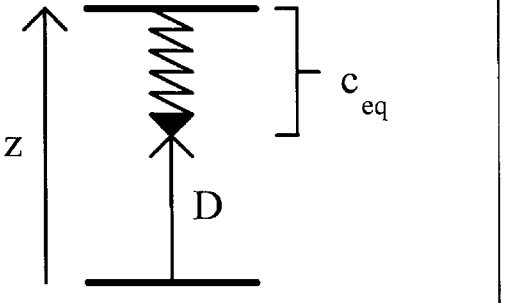

Figure 1: the tip-sample-cantilever system.

To perform a force curve, the cantilever deflection is monitored as the base is withdrawn from the sample; z is being controlled, not D. Since a force curve does not

accurately describe the force vs. distance behavior of the tip vs. the sample, we will use the terminology "deflection vs. distance (DVD) curve."

The relationship between D and z will be used to relate the DVD curve (which is denoted $\beta(z)$) to the tip-sample potential. To find the relationship between D and z, an equation for force balance is used:

[2] $$k(z - D - c_{eq}) + -\frac{d}{dD}V_{ts}(D) = 0.$$

The first term is the force from the cantilever spring; the second term is the force due to the tip-sample potential. When the cantilever is in contact (a compressed state), the cantilever force is negative. The compressed position is in a repulsive regime of the tip-sample potential, therefore the negative derivative will be positive. The total force will be zero at equilibrium.

As the cantilever base is moved, the change in the tip sample distance (dD/dz) is:

[3] $$\frac{dD}{dz} = \frac{k}{k + \frac{d^2}{dD^2}V_{ts}(D)} .$$

For the limiting case where $k >> d^2V_{ts}/dD^2$, the cantilever is not bent by the tip-sample potential, and D changes exactly the same amount as z. For $k << d^2V_{ts}/dD^2$, the tip-sample potential is very stiff and the tip remains fixed relative to the sample regardless of how the cantilever base is moved.

Experimentally, the change in cantilever deflection with respect to z is measured when a force curve is performed:

[4] $$\beta'(z) = \frac{d\beta(z)}{dz} = \frac{d}{dz}(z - D - c_{eq}) = 1 - \frac{dD}{dz} = \frac{\frac{d^2}{dD^2}V_{ts}(D)}{k + \frac{d^2}{dD^2}V_{ts}(D)},$$

which becomes:

[5] $$V_{ts}(D) = \iint \frac{k(\beta'(z))}{(1 - \beta'(z))} dDdD.$$

Since the function is integrated with respect to D, not z, Equation [5] must first be written as a function of D:

[6] $$\beta'(z) = \beta'(D(z)),$$

and from Equation [4]:

[7] $$D(z) = \int 1 - \beta'(z) dz.$$

Numerical simulation

Computer code has been developed to convert the DVD curve to the tip-sample potential (Equation [5]). Figure 2 presents a hypothetical "hard-wall" potential. The DVD curve that would actually be measured due to this potential was calculated; from this DVD curve, the potential was "reconstructed" by the negative integral method and our method (Equation [5]). The zero point on the numerical integration was determined by assuming that the force on the cantilever is zero at maximal distance from the sample. Figure 3 is the same simulation for a Morse potential.

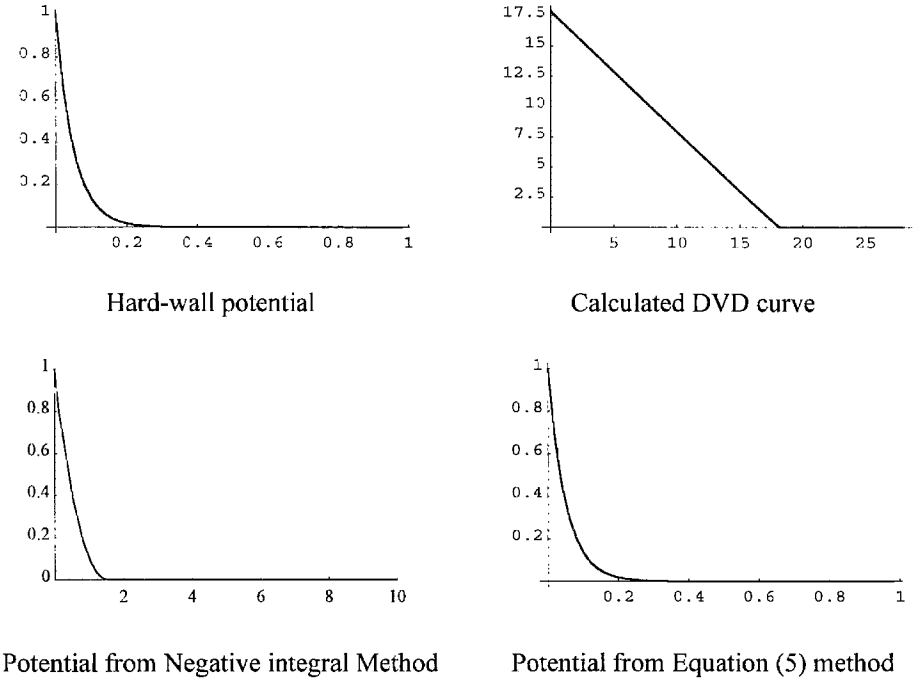

Figure 2: Hard Wall Potential Simulation. The cantilever spring constant = 1 N/m. All the DVD curves have been multiplied by -1 to show deflection away from the surface as positive. The potential derived with the negative integral method has been truncated at 1 nJ for comparison. Notice the difference in length scale.

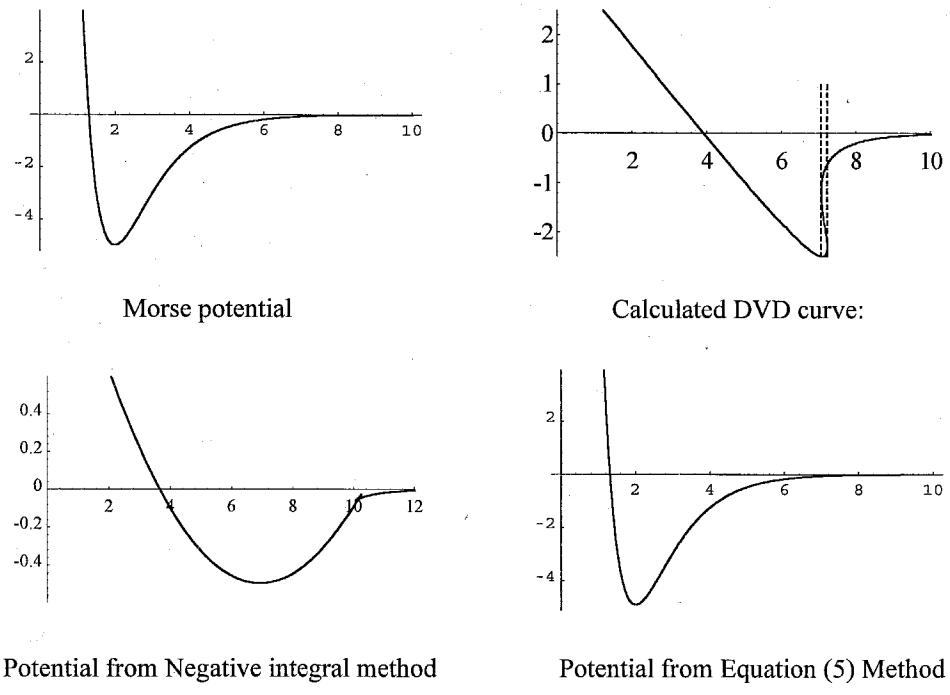

Figure 3: Morse Potential Simulation. The cantilever spring constant = 0.1 N/m. The distance origin is arbitrary. Note the "loopback" in the DVD curve. The dotted lines denote the "points of instability" which manifest themselves in the "jump to contact" and "snap-off" commonly seen in force curves.

AFM systems experience noise from several sources, including thermal cantilever oscillations, electronics noise, and ambient acoustic coupling. The AFM system in our laboratory has a total noise level corresponding to approximately 0.1 nm with a 10μm scan piezo.

Simulations show that the DVD-to-potential transformation is highly sensitive to noise. The effects of the addition of random noise are shown in Figures 4 and 5. This sensitivity is most likely a manifestation of the non-linearity of the algorithm used to perform the conversion.

Application of a smoothing algorithm to the DVD curve corrects this problem. The smoothing algorithm employed was a simple, three-point moving window: the new value at each point is the average of the point and its two nearest neighbors. For 0.1 nm of noise and a cantilever with a 0.1 N/m spring constant, 5 passes of this smoothing algorithm are usually sufficient. For 0.25 nm of noise, 10 passes are sufficient. The smoothing is considered complete when the conversion results are reproducible.

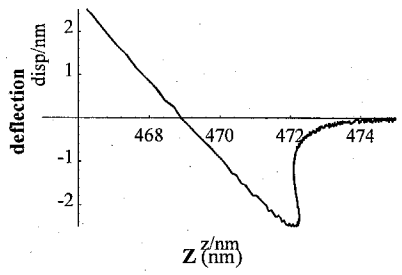

DVD curve with 0.1 nm of noise

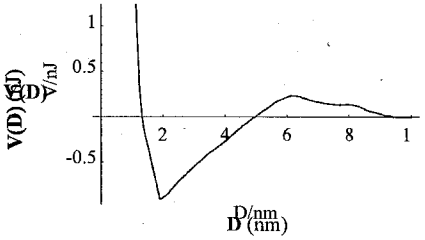

Resultant potential (no smoothing)

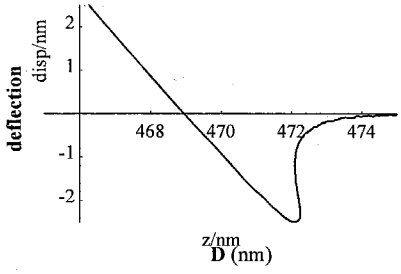

DVD after 5 smoothing passes

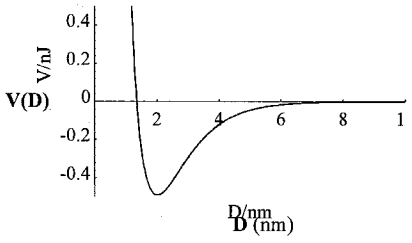

Resultant potential (5 passes)

Figure 4: Simulation with 0.1 nm of noise

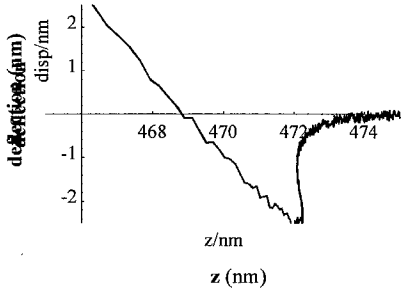

DVD curve with 0.25 nm of noise

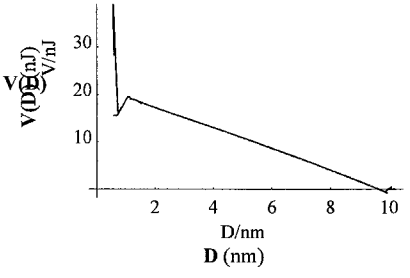

Resultant potential (no smoothing)

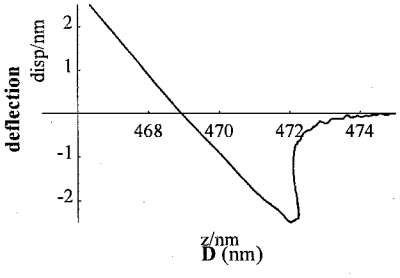

DVD after 10 smoothing passes

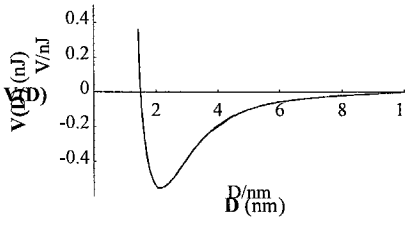

Resultant potential (10 passes)

Figure 5: Simulation with 0.25 nm of Noise

Two other factors may contribute to the inaccuracy of force curves: scanner calibration and spring constant uncertainty. An AFM tube piezoceramic is used to alter the cantilever base-sample distance (z) in a quantitative manner. For most commercially available systems, these scanners are calibrated by the manufacturer. However, hysteresis and repolling may cause these calibrations to be inaccurate. It is preferential to monitor the sample position simultaneously with an alternative mechanism (such as interferometry or capacitance) while the force curve is being performed.

Equation [5] is also dependent upon the cantilever spring constant. Manufacturer specifications can be very inaccurate.[12] A number of highly accurate methods have been developed to determine the cantilever spring constant experimentally.[12-14]

EXTRACTION OF INTERMOLECULAR PAIR POTENTIALS FROM TIP-SAMPLE POTENTIALS

Theoretical model (Analytical)

In this section, the relationship between intermolecular pair potentials, tip geometry, and total tip-sample potential will be analyzed. It will be shown that tip-sample potential can be modeled as the potential between rigidly bound head groups on the tip and sample, *i.e.* $V_{ts}(D) = V_{mol}(D)$. Finally, the tip-sample interaction will be represented by the summation of all the pairwise interactions of chemical "head groups."

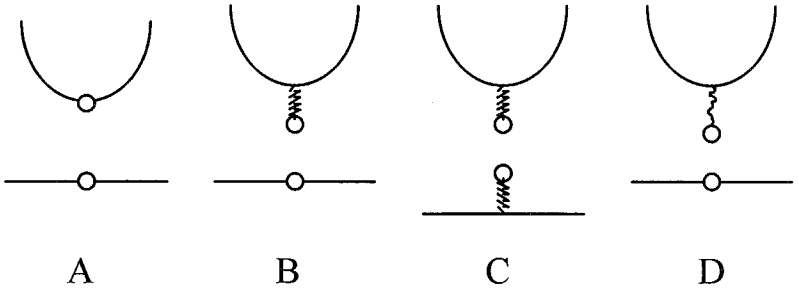

Figure 6: **A.** rigid-rigid model; **B.** rigid-bond; **C.** bond-bond; **D.** molecular tether.

Single interacting pair

RIGID - RIGID

In the case of two interacting headgroups rigidly bound to the tip and sample, the headgroup-headgroup distance D is completely controlled by the relative position of the tip with respect to the sample. In this case, the tip-sample distance and the headgroup-

headgroup distance are equal (D). The potential between tip and sample ($V_{ts}(D)$) is equal to the intermolecular pair potential ($V_{mol}(D)$) between the two head groups: $V_{ts}(D) = V_{mol}(D)$.

RIGID - BOND

If one of the head groups is at the end of a covalent bond, the situation is more complex. The potential in the rigid-rigid case was strictly one-dimensional: $V_{ts} = V_{mol}(D)$. With a covalent bond added, the potential is now a two variable function: $V_{ts}=V_{mol}(D,x)$.

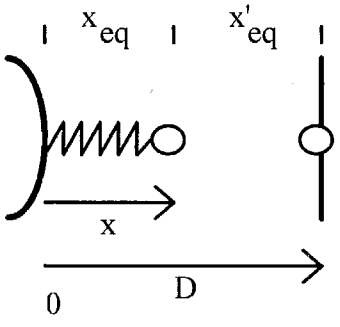

Figure 7: The spring represents a covalent bond; the dotted line represents the head-group headgroup interaction. x_{eq} and x'_{eq} are the equilibrium bond lengths of the covalent and non-covalent (measured) interactions, respectively.

A few simple approximations are used:

1. The total potential is the sum of the potentials of the covalent bond and the interaction potential: $V_{ts} = V_{cov}(x) + V_{mol}(D-x)$.
2. The covalent bond doesn't break in the process of pulling the tip away from the sample.
3. The covalent bond may be assumed to be fixed at its equilibrium length.

The first approximation will fail only if V_{cov} and V_{mol} have a significant amount of "crosstalk" (*i.e.* if the true potential differs from $V_{cov} + V_{mol}$ by a large amount). Figure 8A is contour plot of the total potential for a covalent bond (C-C) and a hydrogen bond, both approximated by morse potentials.

The second approximation can be tested by applying the Boltzmann distribution to the 2D potential. As the tip is retracted from the sample, the tip head-group will enter the "deep" trough (*i.e.* break the V_{mol} bond) or the "shallow" trough (*i.e.* break the covalent bond). Since D changes slowly compared to molecular vibrations ($< 10^7$ nm/sec for a force curve, versus ~ 10^{12} nm/sec for a molecular vibration), the head group is effectively

in thermal equilibrium with its surroundings. Therefore, it is reasonable to consider the two troughs as "states" that will be populated in accordance with the Boltzmann distribution. The ratio of probabilities of occupation of these two states (and therefore the ratio of probabilities of breakage of each bond) is:

[8] $$\frac{P_{shallow}}{P_{deep}} = \frac{P_{break,cov}}{P_{break,mol}} = \frac{e^{-D_{e;cov}/k_bT}}{e^{-D_{e;mol}/k_bT}} = e^{(D_{e;mol}-D_{e;cov})/k_bT},$$

where $D_{e;cov}$ and $D_{e;mol}$ are the dissociation energies of the covalent interaction and the headgroup-headgroup interaction, respectively. For a very weak covalent bond (*e.g.* an oxygen-oxygen peroxide bond, $D_{e;cov} = 2.7 \times 10^{-19}$ J) and a very strong hydrogen bond, ($D_{e;mol} = 5 \times 10^{-20}$ J) the probability of breaking the covalent bond is 6×10^{-24}. For more reasonable bonds strengths (*e.g.* a C-C bond, $D_{e;cov} = 5.6 \times 10^{-19}$ J), this probability would be even lower.

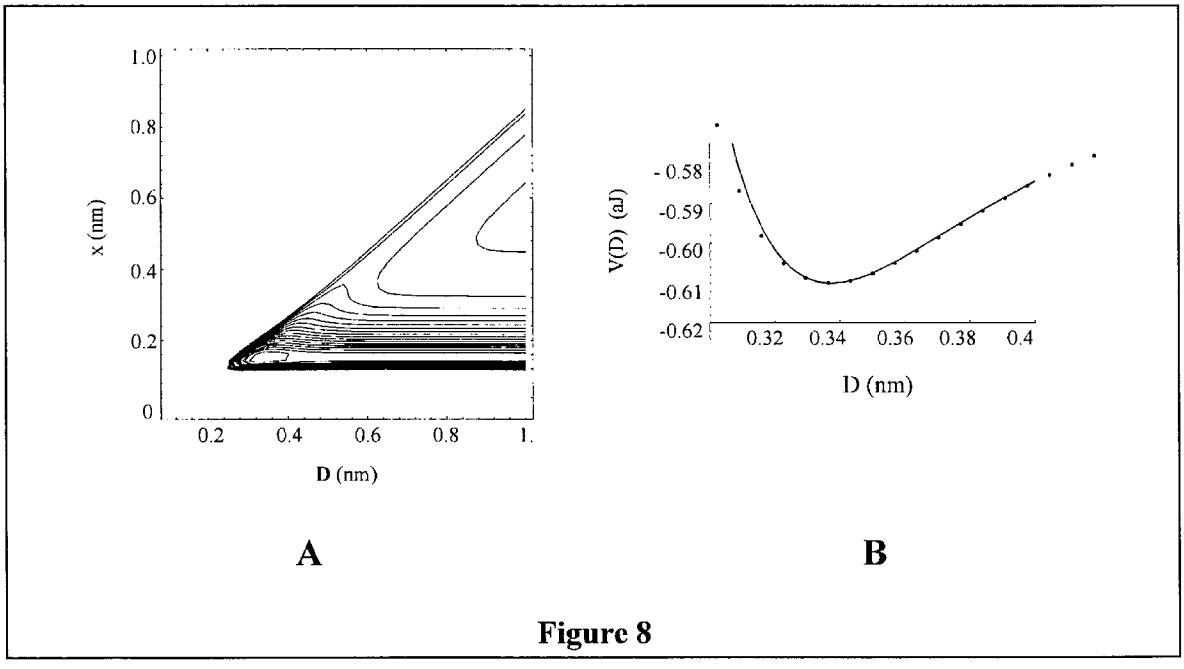

Figure 8

The final assumption is to fix the covalent bond at its equilibrium length. Effectively, this means that $V_{ts}(D)$ is a linecut of $V_{mol}(D,x)$ along $x = x_{eq}$. From the first assumption:

[9] $$V_{ts}(D) = V_{cov}(x_{eq}) + V_{mol}(D - x_{eq}) = b + V_{mol}(D - x_{eq}).$$

$V_{ts}(D)$ is $V_{mol}(D)$ with an offset in D (x_{eq}) and a constant added to the potential. Since the force is measured (-dV/dD), the added constant has no effect and:

[10] $$V_{ts}(D) = V_{mol}(D - x_{eq}).$$

This approximation will only fail if the path of the head group in the potential deviates significantly from a straight line. For example, this deviation may occur in situations where the gradient of V_{mol} approaches the order of the gradient of V_{cov}. Since most intermolecular forces are weaker and vary more slowly than covalent bond forces, this approximation should be accurate. Figure 8B shows a linecut along $x = x_{eq}$ (solid line) and the actual minimum potential vs D (dotted line). Since the covalent bond vibrates rapidly with respect to the change in D, the true path is effectively averaged over the bottom of the deeper trench.

BOND-BOND

In the case where each head group is at the end of a covalent bond, the potential is three-dimensional. This potential can be reduced to a one-dimensional problem by the same method as before.

Multiple groups

In order to derive single molecular potentials from the total tip-sample potential, analytical correlations with a number of tip shapes and a wide variety of intermolecular potentials have been performed. Further, computer algorithms have been developed to perform numerical correlations and decorrelations.

SUM → CORRELATION

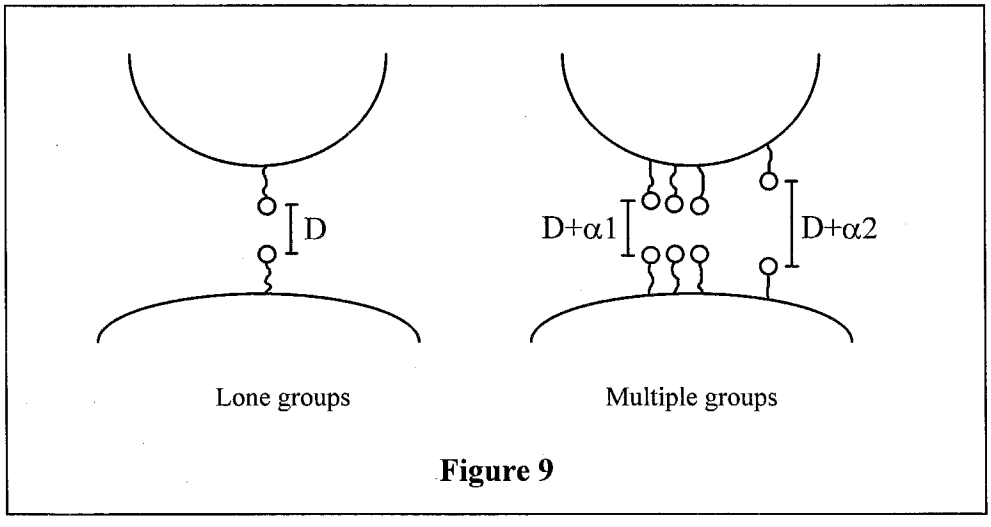

Figure 9

The total tip-sample potential can be written as a sum of the single potentials at variable distances (α)(see Figure 9):

[11] $$V_{ts}(D) = V_{mol}(D+\alpha_1) + V_{mol}(D+\alpha_2) + V_{mol}(D+\alpha_3) + \ldots ;$$

and for n groups:

[12] $$V_{ts}(D) = \sum_{i=1}^{n} V_{mol}(D+\alpha_i).$$

This model assumes no cooperative interaction between the chemical groups. As the limit of a continuum of α_i's is approached:

[13] $$V_{ts}(D) = \int_{-\infty}^{\infty} V_{mol}(D+\alpha)\rho(\alpha)d\alpha,$$

where ρ is the distribution of distances. This integral is a cross-correlation of $V_{mol}(D)$ and $\rho(D)$, a close mathematical relative of the convolution:

14] $$f(x)*g(x) = \int_{-\infty}^{\infty} f(x-\alpha)g(\alpha)d\alpha$$ Convolution

[15] $$f(x)\otimes g(x) = \int_{-\infty}^{\infty} f(x+\alpha)g(\alpha)d\alpha$$ Cross-correlation

[16] $$V_{mol}(D)\otimes\rho(D) = \int_{-\infty}^{\infty} V_{mol}(D+\alpha)\rho(\alpha)d\alpha$$ Tip-Sample cross-correlation

therefore:

[17] $$_{ts}(D) = V_{mol}(D)\otimes\rho(D)$$

This mathematical model is very useful since:

- the correlation may be found by a Fourier transform method if the integral cannot be performed analytically,
- the Fourier transform method can be used to perform a decorrelation, allowing us to find V_{mol} if we know ρ and V_{ts}, and
- numerical methods for performing correlations and decorrelations are readily available.

The Fourier transform method of performing convolutions can be derived by application of the definition of the Fourier transform to the convolution integral. The corresponding method for performing correlations can be derived analogously:

$U_{t\text{-}s}(r) =$	planar -- $\delta(\alpha)$	tilted square $\begin{cases} 1, & 0 \le \alpha \le l\sin\theta \\ 0, & \text{elsewhere} \end{cases}$	sphere -- πd	cone -- $\alpha\pi\sin\theta$	gaussian -- $\frac{1}{\lambda\sqrt{2\pi}}e^{-\alpha^2/2\lambda^2}$
lennard-jones = $4D_e\left(\left(\frac{\sigma}{r}\right)^{12}-\left(\frac{\sigma}{r}\right)^{6}\right)$	$4D_e\left(\left(\frac{\sigma}{r}\right)^{12}-\left(\frac{\sigma}{r}\right)^{6}\right)$	$4D_e\left(\frac{\sigma^{12}}{11r^{11}}-\frac{\sigma^{12}}{11(r+l\sin\theta)^{11}}-\frac{\sigma^{6}}{5r^{5}}+\frac{\sigma^{6}}{5(r+l\sin\theta)^{5}}\right)$	$\pi d 4D_e\frac{\sigma^6\left(-11r^6+5\sigma^6\right)}{55r^{11}}$	$4\pi\sin\theta D_e\sigma^6\frac{\left(2\sigma^6-11r^6\right)}{55r^{10}}$	$\pi\sigma^6\lambda^4 D_e\left(\frac{480L_{\frac{5}{2}}^{-\frac{1}{2}}\left(\frac{r^2\lambda^2}{2}\right)-\sigma^6\lambda^6L_{\frac{11}{2}}^{-\frac{1}{2}}\left(\frac{r^2\lambda^2}{2}\right)}{1920e^{r^2\lambda^2/2}}\right)$
morse = $D_e\left(\left(1-e^{-\beta(r-r_0)}\right)^2-1\right)$	$D_e\left(\left(1-e^{-\beta(r-r_0)}\right)^2-1\right)$	$\frac{D_e}{2\beta}\left[\left(e^{\beta(r_0-r)}-2\right)^2-\left(e^{\beta(r_0-(r+l\sin\theta))}-2\right)^2\right]$	$\frac{\pi dD_e}{2\beta}e^{\beta(r_0-r)}\left(e^{\beta(r_0-r)}-4\right)$	$\frac{\pi\sin\theta D_e}{4\beta^2}\left[e^{-2\beta(r-r_0)}-8e^{-\beta(r-r_0)}\right]$	$D_e\left[e^{2\beta\left(r_0-r+\beta\lambda^2\right)}-2e^{\beta\left(r_0-r+\beta\lambda^2/2\right)}\right]$
power law = $\left(\frac{\sigma}{r}\right)^n$	$\left(\frac{\sigma}{r}\right)^n$	$\frac{\sigma^n}{(n-1)}\left[\frac{1}{r^{n-1}}-\frac{1}{(r+l\sin\theta)^{n-1}}\right]$	$\frac{\pi d\sigma^n}{n-1}\frac{1}{r^{n-1}}$	$\frac{\pi\sin\theta\sigma^n}{\left(n^2-3n+2\right)\left(r^{n-2}\right)}$	--
exponential = ce^{-r/σ_0}	ce^{-r/σ_0}	$-c\sigma_0\left(e^{-(r+l\sin\theta)/\sigma_0}-e^{-r/\sigma_0}\right)$	$\pi dc\sigma_0e^{-r/\sigma_0}$	$\pi\sin\theta c\sigma_0^2e^{-r/\sigma_0}$	$\frac{c}{2\lambda^2}e^{\lambda^2\sigma_0^2/2-r/\sigma_0}$
couloomb = $\frac{q_1q_2}{4\pi\varepsilon}\frac{1}{r}$	$C_c\frac{1}{r}$	$C_c\left(\ln(r+l\sin\theta)-\ln(r)\right)$	does not converge	does not converge	$C_c\frac{\sqrt{\pi/2}Erfi\left(r\lambda/\sqrt{2}\right)}{\lambda e^{r^2\lambda^2/2}}$
charge-dipole = $-\frac{q\mu\cos\theta}{4\pi\varepsilon}\frac{1}{r^2}$	$-C_{cd}\frac{1}{r^2}$	$-C_{cd}\left(\frac{1}{r}-\frac{1}{r+l\sin\theta}\right)$	$-C_{cd}d\frac{1}{r}$	does not converge	$C_{cd}\frac{\pi\lambda L_{\frac{1}{2}}^{-\frac{1}{2}}\left(\frac{r^2\lambda^2}{2}\right)}{2\lambda e^{r^2\lambda^2/2}}$
dipole-dipole = $-\frac{\mu_1\mu_2}{4\pi\varepsilon}\begin{pmatrix}2\cos\theta_1\cos\theta_2\\-\sin\theta_1\sin\theta_2\cos\phi\end{pmatrix}\frac{1}{r^3}$	$-C_{dd}\frac{1}{r^3}$	$-C_{dd}\left(\frac{1}{2r^2}-\frac{1}{2(r+l\sin\theta)^2}\right)$	$-C_{dd}d\pi\frac{1}{r^2}$	$-C_{dd}\pi^2\sin\theta\frac{1}{2r}$	$C_{dd}\frac{\pi^2\lambda^2rL_{\frac{1}{2}}^{\frac{1}{2}}\left(\frac{r^2\lambda^2}{2}\right)}{4e^{r^2\lambda^2/2}}$
charge-nonpolar = $-\frac{q^2\alpha}{2(4\pi\varepsilon)^2}\frac{1}{r^4}$	$-C_{cn}\frac{1}{r^4}$	$-C_{cn}\left(\frac{1}{3r^3}-\frac{1}{3(r+l\sin\theta)^3}\right)$	$-C_{cn}d\pi\frac{1}{r^3}$	$-C_{cn}\pi\sin\theta\frac{1}{6r^2}$	$C_{cn}\frac{\pi\lambda^2L_{\frac{3}{2}}^{\frac{1}{2}}\left(\frac{r^2\lambda^2}{2}\right)}{4e^{r^2\lambda^2/2}}$
dipole-nonpolar = $-\frac{\mu^2\left(1+3(\cos\theta)^2\right)}{2(4\pi\varepsilon)^2}\frac{1}{r^6}$	$-C_{dn}\frac{1}{r^6}$	$-C_{dn}\left(\frac{1}{5r^5}-\frac{1}{5(r+l\sin\theta)^5}\right)$	$-C_{dn}d\pi\frac{1}{r^5}$	$-C_{dn}\pi\sin\theta\frac{1}{20r^4}$	$C_{dn}\frac{\pi\lambda^4L_{\frac{5}{2}}^{-\frac{1}{2}}\left(\frac{r^2\lambda^2}{2}\right)}{16e^{r^2\lambda^2/2}}$
nonpolar-nopolar = $-\frac{3h\nu\alpha^3}{4(4\pi\varepsilon)^2}\frac{1}{r^6}$	$-C_{nn}\frac{1}{r^6}$	$-C_{nn}\left(\frac{1}{5r^5}-\frac{1}{5(r+l\sin\theta)^5}\right)$	$-C_{nn}d\pi\frac{1}{r^5}$	$-C_{nn}\pi\sin\theta\frac{1}{20r^4}$	$C_{nn}\frac{\pi\lambda^4L_{\frac{5}{2}}^{-\frac{1}{2}}\left(\frac{r^2\lambda^2}{2}\right)}{16e^{r^2\lambda^2/2}}$

Table 1: analytical corrclations

[18] $f(x) * g(x) = F^{-1}[F[f(x)] \cdot F[g(x)]]$ Convolution

19] $f(x) \otimes g(x) = F^{-1}[F[f(x)] \cdot F[g(-x)]]$ Correlation

[20] $V_{mol}(D) \otimes \rho(D) = F^{-1}[F[V_{mol}(D)] \cdot F[\rho(-D)]]$ Tip - Sample Correlation

F and F^{-1} represent the Fourier transform and inverse Fourier transform, respectively.

Numerical decorrelation

USED TO FIND INTERMOLECULAR PAIR POTENTIAL:

Straightforward manipulation of the correlation Equations [17] and [20] gives:

[21] $$V_{mol}(D) = F^{-1}\left[\frac{F[V_{ts}(D)]}{F[\rho(-D)]}\right].$$

If $V_{ts}(D)$ and $\rho(D)$ are known, it is in principle possible to extract the intermolecular pair potential of the head groups ($V_{mol}(D)$).

There are several intrinsic limitations to the decorrelation method. Since $V_{ts}(D)$ is averaged over x and y, the extracted $V_{mol}(D)$ is also averaged in x and y. A smooth $\rho(D)$ is a good approximation for a reasonably large number of head groups ($n > 200$ or more).

The correlation method makes the assumption that all interactions are pairwise and molecules only interact with other molecules that are directly opposite them. No account is made for cooperatively between neighboring head groups. If necessary, an appropriately weighted $\rho(D)$ could be chosen to include these cooperative interactions before decorrelating.

USED TO FIND ρ:

The correlation Equations [17] and [20] can also be rearranged to give:

[22] $$\rho(-D) = F^{-1}\left[\frac{F[V_{ts}(D)]}{F[V_{mol}(D)]}\right].$$

Therefore, if $V_{ts}(D)$ and $V_{mol}(D)$ are known, it is in principle possible to extract $\rho(D)$, the head-group distribution function. However, this method has limitations similar to those discussed above. Also, $\rho(D)$ does not uniquely determine the actual geometry (see Figure 10). However, the distribution itself is a valuable piece of information because it allows the radius of curvature at the apex of the probe to be estimated. A distribution

which has a large value close to D = 0 must have a large radius of curvature; a distribution which is near zero at D = 0 has a small radius of curvature.

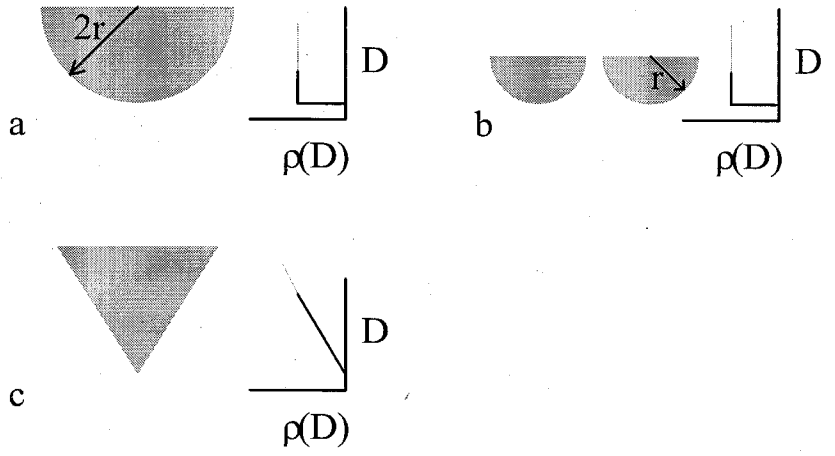

Figure 10: The sphere in **a** and the two spheres in **c** have identical ρ(D), despite having radically different geometries. Comparison of **a** and **c** shows how ρ(D) differs for dull and sharp tip apex shapes.

APPLICATIONS:

Both of the decorrelation methods above assume that $V_{ts}(D)$ has been extracted from the DVD curve. In practice, instrumental limitations restrict the measurement to a finite segment of the DVD curve and thus a finite segment or "envelope" of the potential. Effectively, $V_{ts}(D)$ is being multiplied by a window function (w(D)); w(D) = 1 where $V_{ts}(D)$ is known; w(D) = 0 elsewhere. Therefore, in the Fourier domain, $F[V_{ts}(D)]$ must be replaced with $F[V_{ts}(D)] * F[w(D)]$ (Equations [20] and [21]). This limitation makes the numerical decorrelation possible only under certain conditions.

If $V_{ts}(D)$ is zero outside the envelope, the decorrelation is correct and the information outside the envelope does not corrupt the data. For example, at the right cutoff (i.e. large D), $V_{ts}(D)$ approaches zero. However, most potentials become strongly repulsive as D approaches zero. The left cutoff will be in the repulsive regime, where $V_{ts}(D)$ is large outside the envelope and may distort the results.

If the portion of $V_{ts}(D)$ that lies outside the envelope contributes to the value of the correlation at a particular point, the decorrelation of the envelope-limited $V_{ts}(D)$ at that point will be inaccurate. $V_{ts}(D)$ beyond the left cutoff will be large and will contribute to the value of the correlation within the width of the window. For example, if ρ(D) is non-zero at 1 nm, then the leftmost 1 nm of the decorrelation of the envelope-limited $V_{ts}(D)$ will be inaccurate and must be discarded. Therefore, this method is limited to cases

where the width of the correlating function is less than the width of the potential, $V_{ts}(D)$. Practically, a narrow $\rho(D)$ is required, such as planar, tilted square (with a small angle), narrow gaussians, *etc.*

A more flexible way of doing decorrelations is to use an analytical correlation as given in Table [1]. A functional form, $V_{ff}(D)$ must first be chosen to represent the intermolecular. The correlation $V_{ff}(D)\otimes\rho(D)$ is then fit to the experimentally determined $V_{ts}(D)$. This method avoids envelope-limited potentials and is less sensitive to noise than the decorrelation method. Unfortunately, this method limits the functional form of the potential.

CONCLUSION

In this report, an accurate method for deriving tip-sample potentials from AFM force curves has been developed. Also, a mathematical technique for determining single molecular pair potentials from these tip-sample potentials has been developed. In practice, these algorithms may be used by an experimental microscopist in two manners.

First, if the surface chemistry of the AFM tip is carefully controlled, it should be possible to determine an accurate $\rho(D)$ from the measured force curve, since the molecular pair potentials can be estimated. As noted above, many complicated tip geometries may possess similar $\rho(D)$. However, for typical AFM tips, it should be possible to accurately estimate the radius of curvature of the apex with this method.

Second, an accurate determination of the tip apex shape will produce an accurate $\rho(D)$. Therefore, if a chemical moiety with an unknown pair potential is attached to the tip, the pair potential can be extracted from the force curve.

REFERENCES

1. Binnig G., Quate C., Gerber C. Phys. Rev. Lett. **56**, 930 (1986).
2. Albrecht T., Quate C., J. Appl. Phys. **62**, 2599 (1987).
3. Hansma P. *etal.* Appl. Phys. Lett. **64**, 1738 (1994).
4. Burnham N., Colton R., Pollock M. Nanotechnology **4**, 64 (1993).
5. Israelachivili J. Intermolecular and Surface Forces, Academic Press, New York, (1992).
6. Hartmann U. JVSTB **9**, 465 (1991).
7. Burnham N., Colton R., Pollock H. Phys. Rev. Lett. **69**, 144 (1992).
8. Kotomin E., Shluger A., Causa M., Dovesi R., Ricca F. Surf. Sci. **232,** 399 (1990).
9. Frisbie C., Rozsnyai L., Noy A., Wrighton M., Lieber C. Science **265,** 2071 (1994).
10. Lee G., Chrisey L., Colton R. Science **266,** 771 (1994).

11. Lee G., Kidwell D., Colton R. Langmuir **10**, 354 (1994).
12. Senden T. and Ducker W. Langmuir **10**, 1003 (1994).
13. Cleveland J., Manne S., Bocek D., Hansma P. RSI **64**, 403, (1993).
14. Hutter J. and Bechhoefer J. RSI **64**, 1868 (1993).

Marc Unger is a graduate student at Caltech and my primary cohort on this project, as well as the first author of the patent that appears in Appendix I.

CHAPTER 6 - Near-field Scanning Optical Microscopy

The eyes are perhaps the most powerful tool a scientist possesses for observing natural phenomena. In 1611, Johanes Kepler proposed the first compound microscope, thereby expanding our realm of vision to the microcosm. Ever since, scientists have struggled to increase the magnifying power and versatility of their microscopes: classsically with improved lenses and alternative types of radiation, more recently with lasers and local surface probes. However, due to the low cost, non-invasive nature, and multiple contrast mechanisms associated with visible light, biologists have found traditional optical microscopy to be irreplacible for most applications. Regretfully, many interesting biological features are much smaller than the resolving power of visible wavelengths (resolution > $\lambda/2$ = 210 - 400 nm).

Electron micrsocopy provides information in the nm range. However, the sample preparation requirements make imaging under ambient biological conditions impossible; a metal coating must be applied to insulating samples. Imaging of dynamical biological processes in the 10 - 50 nm range under ambient conditions has in the past been very difficult for the interested observer.

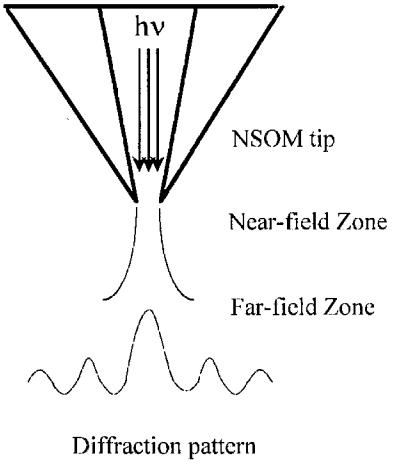

Figure 1: Principle of near-field optics

Near-field Scanning Optical Micrscopy (NSOM) is a relatively new form of probe microscopy (at least in its popularity). The technique was actually invented in 1972.[1] The method utilizes small apertures to image optically surface features. As light passes through a small hole, classical diffraction will occur in the far-field; the far-field is loosely defined as the distance away from the hole equal to or greater than the wavelength of the light. In the region microscopically close to the aperture, a near-field zone is created where the light remains collimated to the size of the aperture(see Figure 1).[2] A NSOM experiment is performed as follows:

- the sub-wavelength aperature is held just above a sample surface.
- the sample is now optically excited.
- classical optical contrast mechanisms are monitored, for example: absorbtion, transmission, fluorescence, *etc.*
- the tip is scanned across the surface and the optical output is monitored at each position.

A critical feature of any probe microscope is the shape of the tip. In NSOM, a sub-wavelength hole must be constructed and scanned over the sample surface. Lewis *et al.* first developed tapered NSOM tips in 1986 by pulling quartz micro pipettes down to a point, then coating the outside with evaporated aluminum.[3] This method produced a very small hole (~ 150 nm) with a long aspect ratio. Betzig *et al.* have since found that tips constructed from quartz fiber optics have a natural degree of collimation along the propagating axis, resulting in a larger amount of light reaching the end of the tip which enhances the intensity for smaller and smaller hole sizes (~ 10 nm).[4]

This chapter will outline the instrumental designs that have been implemented at Caltech. Particularly:

- the construction of NSOM tips
- two instrumental designs and their implementation
- early experiments to combine NSOM and mass spectrometry.

TIPS

Fiber optic tips have been used for our experiments at Caltech; capillary based tips have also been constructed but are inferior to the fiber optic tips. The tips are constructed as follows:

1. The fibers[5] are heated with a CO_2 laser until the quartz become viscous.
2. The fibers are quickly pulled to draw out the quartz to a small point and broken into two sharp tips.
3. The pulled tips are shadow coated from an angle with aluminum in order to produce an opaque coating around the sides of the taper but not at the end of the tip.

Steps 1 and 2 are accomplished with a commercially available quartz capillary puller located in Scott Fraser's lab in the Beckman Institute.[6] The following settings[7] produce sharp tips (< 100 nm) with good aspect ratios for both quartz capillaries and optical fibers:

	heat	filament	velocity	delay	pull
fibers	600-800	0	~20	0	100-200
capillaries	700	4	50	145	150

Step 3 is accomplished using an evaporation system that has been constructed in 33 Noyes. An old evaporator was secured from Mitchio Okumura's lab. A motorized spin-coater was constructed to hold 22 fibers in a circle around the evaporation element. Each individual fiber is spun on its own axis as the aluminum is evaporated, producing an even

coating on the tips. The "spin-coater" and evaporator are shown in Figure 2. Aluminum is used as the coating material; it has one of the shortest extinction coefficients (6.5 nm) and highest reflectivity (92 % at visible wavelengths) of any material.[8]

Figure 2: evaporator and spin coater

Figure 3 is an electron micrograph of a coated-NSOM tip. The end of the tip is uncoated and appears dark in the image since charging occurs at insulating areas of the sample. The scale bar is ~ 150 nm.

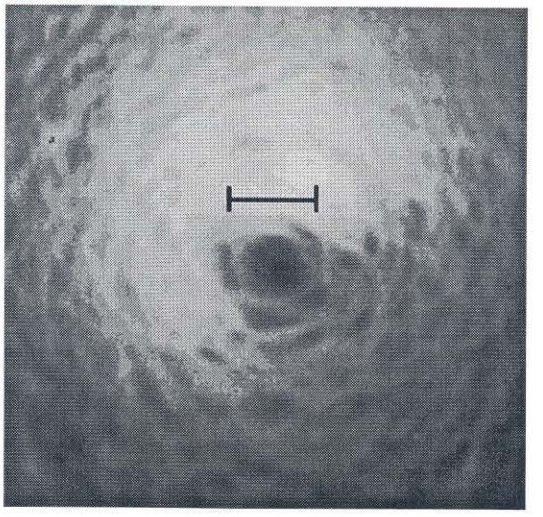

Figure 3: an electron micrograph of the end of an NSOM tip; the scal bar is 150 nm.

INSTRUMENTAL SETUP

Preliminary experiments were completed in our laboratory using the NSOM setup shown in Figure 4A. The near-field light transmitted at the sample surface passes through a transparent substrate and is collected in the far field. An inverted microscope was used to collect the light and focus it onto a photomultiplier tube (see Figure 4B). No feedback mechanism was built into this design.

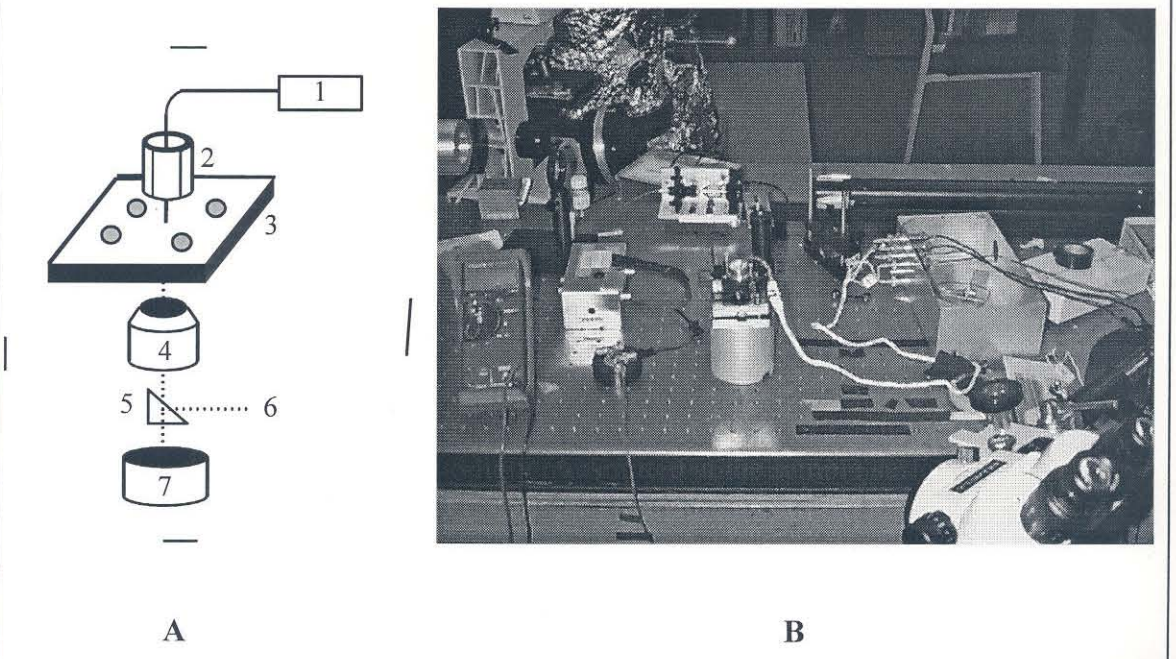

Figure 4: **A** - schematic of no-feedback NSOM instrument. A laser is coupled to a fiberoptic (**1**). The tip is scanned with a tube piezoceramic (**2**) over a sample (**3**). A microscope objective is used to capture the light (**4**) and focus it on a beam splitter(**5**); the beamsplitter sends the light to an eyepiece (**6**) and a photomultiplier tube (**7**). **B** - overview of the experimental system.

Figure 5 is the first image acquired with this instrument. The sample was fresh blood taken from a human finger and smeared onto a cover slip. The tip was lowered towards the sample and an image was acquired at each position. The characteristic doughnut shape of red blood cells can be seen from the image. It is difficult to deterimine the resolution of this image, however it is superior to images obtained with high resolution light micrsocopy. As the tip was lowered, it eventually ran into the sample and was destroyed (see Figure 5B).

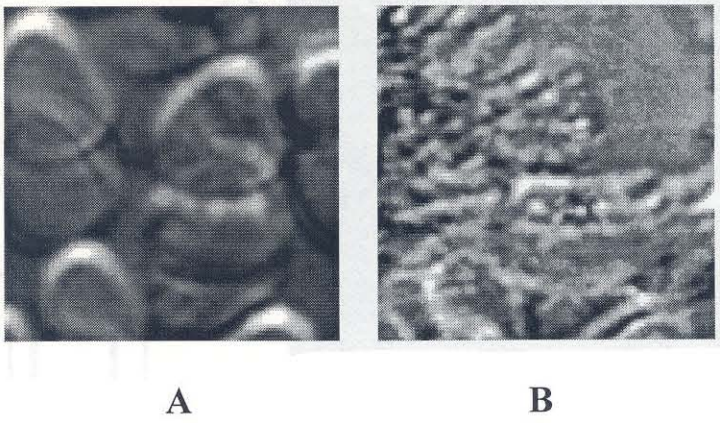

Figure 5: two consective images of RBCs; **A** - Notice the characteristic doughnut shape; **B** - the tip was motored towards the sample one extra iteration and this image was acquired. The tip has been destroyed, as have the cells.

Other samples were imaged with this setup, including liposomes, macrophages and latex beads. However, with this preliminary setup the resolution was never good and the tips were easily destroyed. Therefore, a feedback mechanism was incorporated into the instrument design.

FEEDBACK

In order to exploit fully the near-field effect, the tip-sample distance must be accurately monitored and maintained. The shear force feedback mechanism first demonstrated by Betzig *et al.* was chosen.[9] The fiber is vibrated at its resonance frequency (> 100 kHz, ~ 0.1 nm). The resulting tip amplitude is very large due to its high **Q** factor (~ 100). Our experimental setup has a focused laser diode striking the shaft of the tip at a 60° angle. The partially obstructed beam will then reflect off the sample and onto a two-quadrant photodiode that can monitor the relative dithering response(see Figure 6). This setup is currently being used by Dimitri Kossakovski for imaging purposes.

When the tip approaches the sample, the local shear interactions cause a slight change in the resonance frequency; the majority of this shift is due to the tip interacting with a thin layer of adsorbed water on the sample surface. This resonance shift alters the amplitude and phase of the tip vibration; these shifts can be monitored with a lock-in amplifier. Figure 7 is a curve showing the relative amplitude and phase changes of the dithering tip as it approaches the sample. The feedback can be locked in on either an amplitude or phase shift:

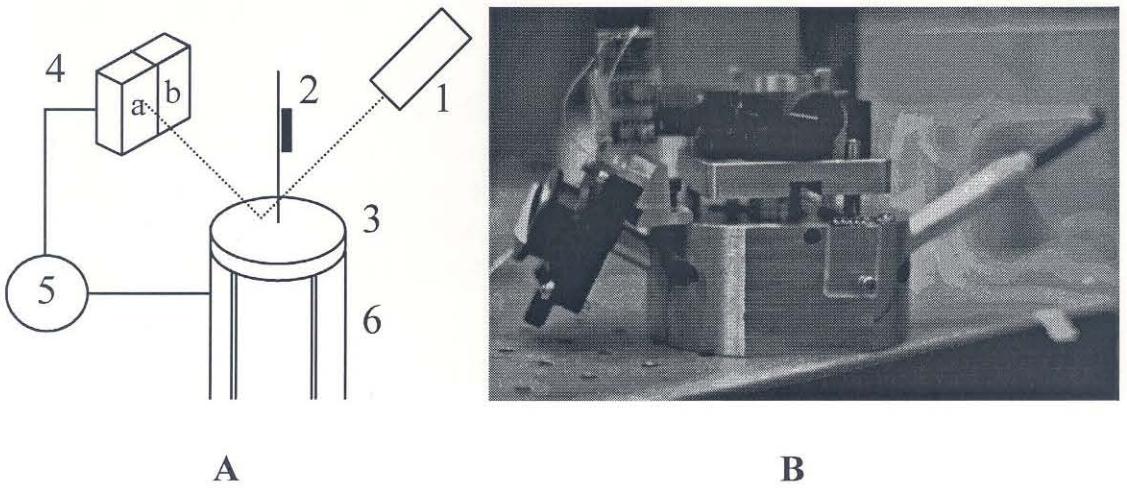

Figure 6: **A** - schematic of the dithering feedback setup. A laser diode (**1**) is focused onto the NSOM tip that is being vibrated at its resonance frequency (**2**). The direction of the vibration is perpindicular to the incoming beam. The beam is reflected off the sample (**3**) and onto a 2-sector photodiode (**4**). The output signal [(a-b)/(a+b)] is sent through a feedback circuit (**5**) that adjusts the height of the sample by expanding a piezoceramic tube.(**6**) In this manner, a constant tip-sample seperation can be maintained. **B** - picture of dithering instrument.

- the tip is vibrated at its resonance frequency.
- when the tip approaches the sample, the resonance shift causes the amplitude to be lowered; this lowering can be used as a feedback mechanism.
- as the tip is scanned, changes in height and sample composition will alter the amplitude; the height of the sample is modulated to maintain the setpoint amplitude.

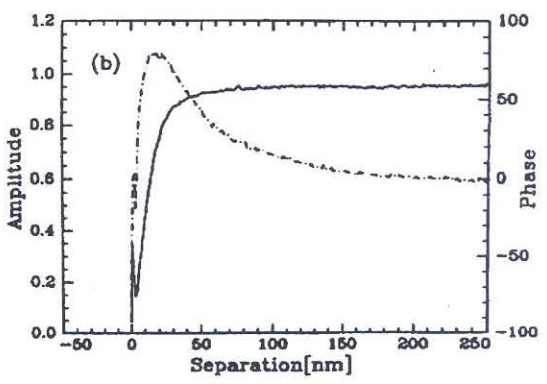

Figure 7: the amplitude (solid line) and phase changes (dotted line) as a NSOM tip approaches a sampole. from reference 9

LASER DESORPTION

A collaberative effort between the Beachamp and Baldeschwieler group has combined our respective interests, namely probe micrscopy and mass spectrometry. The goal of this collaberation is to use NSOM to desorb ions from the surface of a sample and analyze these ions with Time of Flight Mass Spectrometry (TOF-MS). In this manner, the chemical nature of a surface may be analyzed with superior lateral resolution.

The basic operating principle of TOF-MS is to separate ions of different mass to charge ratios based on their relative velocities in an electrostatic potential. All of the ions are accelerated to the same kinetic energy; the lighter ions achieve a higher velocity, since:

$$\text{K.E.} = \text{constant} = \tfrac{1}{2} m_1 v_1^2 = \tfrac{1}{2} m_2 v_2^2 .$$

The ions are then allowed to drift in a field-free region; the different velocities will spatially separate them. At the end of the drift region, they sequentially hit a detector and their flight times are recorded.

Matrix-assisted Laser Desorption Ionization (MALDI) has been shown to be an excellent method for producing ion in the gas phase, especially for large biological molecules.[10] The molecules to be studied are suspended in a acidic matrix that enhances the desorption-ionization process; dihydroxy-benzoic acid was used as a matrix in these experiments. When a short, high energy laser pulse (~ 3 ns) with a fluence of 10^6 - 10^7 watts/cm^2 strikes the sample, the embedded analyte is transferred into the gas phase and ionized with little or no decomposition. The mass to charge ratio may be deduced.

In our experiment, a NSOM tip is used to deliver the light to the surface and desorb ions from a very small area. The tip is then scanned across the sample and the mass spectrum at each position is recorded. This technique should allow sub-micron mass resolution in a lateral direction. The highest resolution previously reported using laser desorption is 1 μm.[11]

Classical TOF setups are symmetrical in design with the ion source normal to the flight tube. This configuration is unappealing for our experiments, since our NSOM tip must be normal to the surface and would block the flight tube. The angular configuration shown in Figure 8 is used to circumvent this problem.

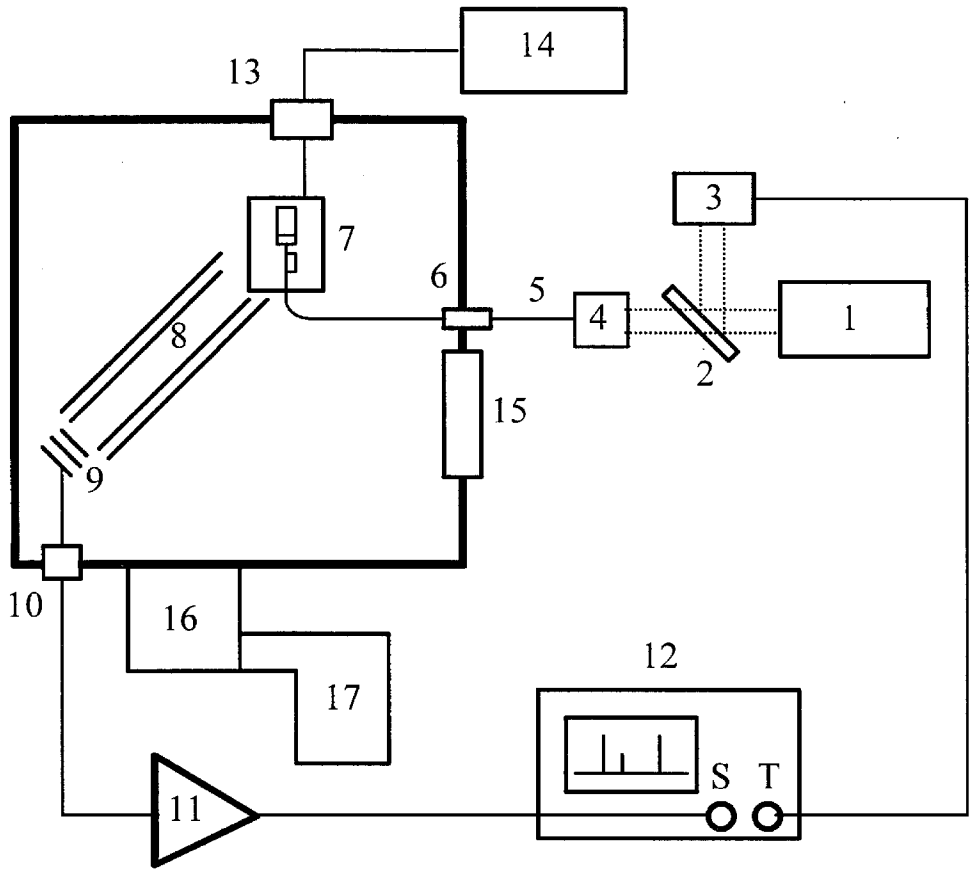

Figure 8: Schematic of the NSOM-TOF setup; see the text for a description of each item.

DESCRIPTION OF FIGURE 8:

1. Pulsed nitrogen laser.[13] This UV laser produces a 3 ns - 250 microjoule pulse at 337 nm. A major consideration was the low cost (~ $5,000).
2. The laser beam is split with a simple glass plate. Most of the beam (~ 95%) is transmitted towards the fiber coupler. The other 5 % is reflected to a joulemeter.
3. A joulemeter is used to trigger the storage oscilliscope.[14] As can be seen in Figure 11, the the delay between the output from the joulemeter and the time ions are desorbed at the sample surface is negligible for the flight times used in our experiments.
4. Fiber coupler.[15] 10% coupling efficiency has been obtained with this coupler, which is the theoretical limit attainable with the divergence angle of the LSI laser. Also, this coupler has shown excellent stability ($\Delta A < 1\%$ over a week).

5. UV tuned fiberoptic.[16] The choice of fiberoptic has proven very crucial. If the fibers are not tuned to UV wavelengths, it is very easy to destroy the cleaved end when trying to couple the light.
6. Two methods may be employed to insert the fiber optic tip into the vacuum chamber: the entire coupling apparatus may be placed in the chamber and the laser light focused through a quartz window, or the fiber may be externally coupled and then fed into the chamber. A teflon feedthrough connector was constructed that allowed chamber pressures as low as 10^{-8} torr. [At this pressure, the feedthrough was not the limiting factor.] Internal coupling could be very sensitive to ambient vibrations and would not allow quantitative chemical analysis.
7. The sample/tip stage is mounted at an angle (~ 45°) to the flight tube.
8. The flight tube consists of two concentric steel tubes; the outer tube is a ground shield to protect the surrondings (and users) from the high voltage on the inner tube tube (> 3 kV).
9. Microchannel plate (MCP) detector.
10. High voltage feedthrough for the flight tube voltage, MCP HV, and MCP output current.
11. MCP preamplifier. Figure 9 is a electrical schematic of the high-speed preamp used for this system.
12. Lecroy Storage Oscilliscope.[17] The scope is triggered by the joulemeter output. The data can be downloaded to a laser writer or digitially stored and transferred to a computer.
13. HV feedthrough for the sample stage control.
14. NSOM control electronics for approach, feedback, and scanning.[18]
15. Quartz view-window.
16. Turbo-molecular pumping has attained pressures as low as 1 x 10^{-8} with our chamber.[19]
17. A mechanical pump is used to back up the turbo pump.

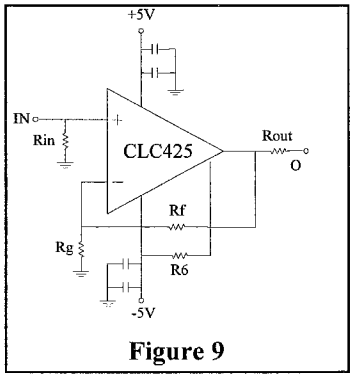

Figure 9

Another problem is that the sample is usually biased at high voltage (3 - 100kV) in order to impart the initial flight energy. However, if a conducting NSOM tip is held < 100 nm from a high voltage source, arcing would cause the tip to be destroyed. Therefore, a high voltage is applied to the flight tube. Figure 10 shows the field lines calculated for the flight tube that has been constructed.[12]

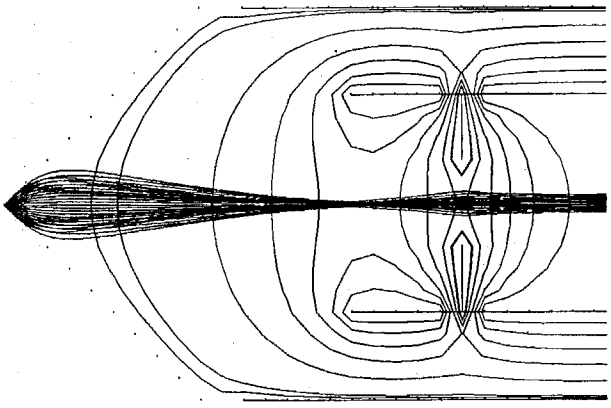

Figure 10: Simulation of the field lines; the sample and outer tube are grounded; the inner tube is at + 3 kV; the lens is at + 430 V.

Preliminary mass spectra was obtained with this instrument (see Figure 11). Ionization was accomplished with a focused laser beam, not with a NSOM tip. The sample was a copper block covered with both acetylcholine and methylene blue. The peaks are labeled in the figure.

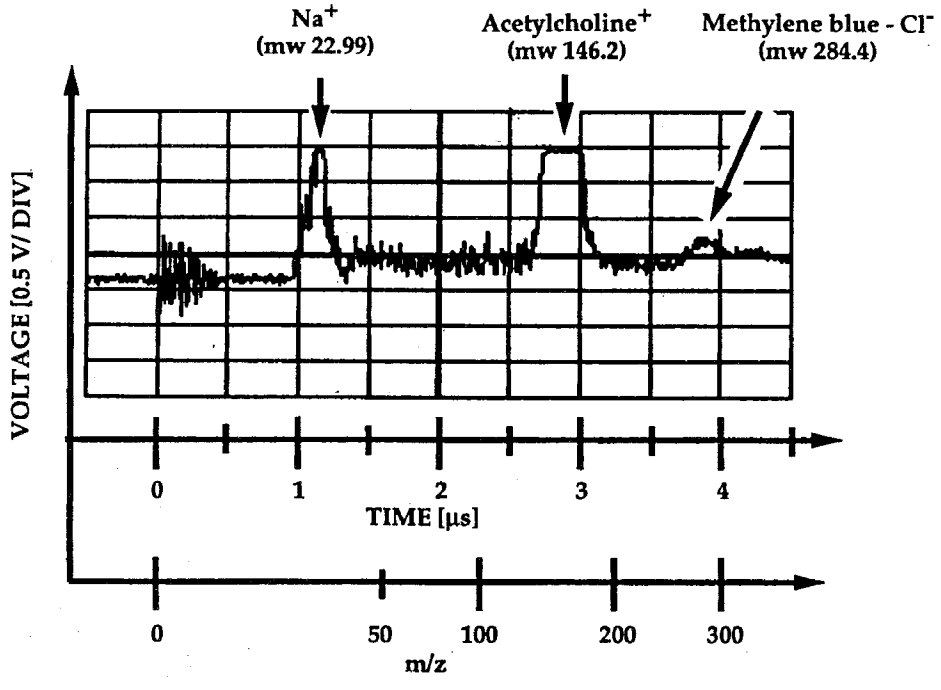

Figure 11: Mass spectrum using our TOF setup; the sample was a methylene blue/acetycholine solution evaporated onto a small copper block.

Two main factors are responsible for the widening of the spectral peaks in Figure 11: the flight tube is relatively short and the ions are desorbed at a 45° angle. The short flight length will not allow the drift velocities to separate the ions a large amount. More importantly, the ions are ejected from the surface with an initial kinetic energy. If the sample is perpendicular to the flight tube, the distribution of the ejected ions will be fairly narrow; this distribution will be determined by the difference between longest ($\mathbf{d_2}$) and shortest ($\mathbf{d_1}$) path lenghts that the ions must follow (see Figure 12). After desorption, the ions with the shortest path length ($\mathbf{d_1}$) will reach the detector first; the total width of the signal will be determined by how long it takes the ions with the longest path length ($\mathbf{d_2}$) to reach the detector once the first ions are monitored. Therefore, the larger the difference between $\mathbf{d_1}$ and $\mathbf{d_2}$, the wider the signal will be.

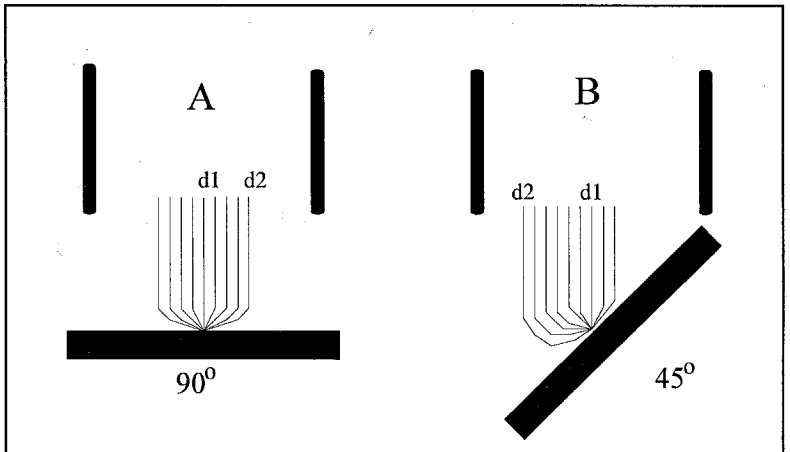

Figure 12: trajectories for two sample/flight tube geometries; the difference between $\mathbf{d_1}$ and $\mathbf{d_2}$ will be much smaller for the perpindicular geometry (A).

The flight tube length in our experiment was limited to the vacuum chamber available. A creative geometric setup could possibly eliminate the latter problem. However, these experiments are only meant to demonstrate high spatial resolution with this instrument, therefore the resolution of this spectrometer is sufficient.

CONCLUSION

This chapter outlined the preliminary work accomplished using NSOM. In particular, the construction of a NSOM with a dithering feedback mechanism was described, as well as our early attempts to use this system to desorb ions in the gas phase. Once efficient laser desorption has been accomplished with this system, a test sample will be used to demonstrate the superior lateral resolution that this technique will afford. One example would be a simple test grating used to calibrate electron microscopes. The grating will be

soaked in a solution of methylene blue. As the tip is scanned, there should be a peak at 284 mass units when the tip is over a protrusion in the grating; when the tip is over a gap, no mass peak will be observed. An image may be displayed based on the intensity of the methylene blue mass peak height.

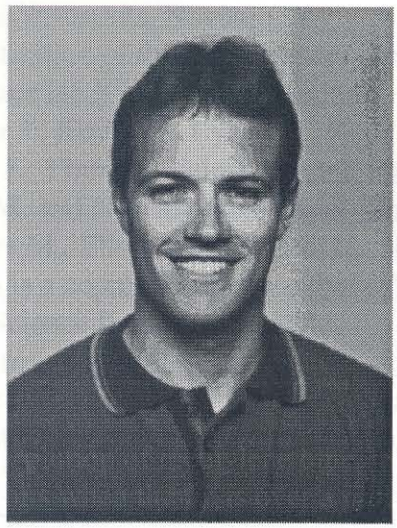

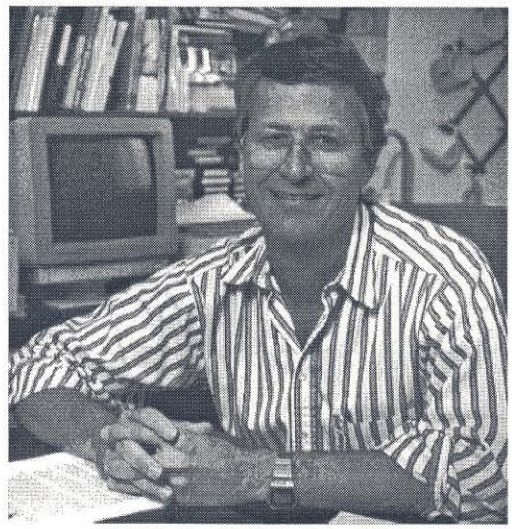

Figure 14: Marcel Widmer, Dimitri Kossakovski, and Jack Beachamp.

REFERENCES

1. Ash E. and Nicolls, G. Nature **237**, 510 (1972).
2. Novotny L., Pohl D., Regli P. J. Opt. Soc. Amer. A **11**, 1768 (1994).
3. Harootunian A., Betzig E., Isaacson M., Lewis A. Appl. Phys. Lett. **49**, 674 (1986).
4. Betzig E., Trautman J., Harris T., Weiner J., Kostelak R. Science **251**, 1468 (1991).
5. Single mode fibers with a 4 μm core diameter were used for these experiments.
6. Sutter Instruments, Novato CA.
7. The definition of these parameters can be found in the Sutter laser-puller manual in the Fraser lab [01 Beckman Institute].
8. Weaver J., Krafta C., Lynch D., Koch E. Phys. Daten. **18,** 14 (1981).
9. Betzig E., Finn E., Weiner J. Appl. Phys. Lett. **60**, 2484 (1992).
10. Karas M. and Hillenkamp F. Anal. Chem. **60**, 2299 (1988).
11. de Vries M., Elloway D., Wendt H., Hunziker H. RSI **63**, 3321 (1992).
12. Simion is a copmuter program that calculates field lines and ion trajectories.
13. Laser Science Inc., Newton MA.
14. Molectron, Portland OR.
15. Oz Optics Ltd., Nepean, Ontario, Canada
16. Radiant Communication Corp., South Plainfield, NJ.
17. Lecroy Corp., Chestnut Ridge, NJ.
18. Clark S., Baselt D., Spence C., Youngquist M., Baldeschwieler J. RSI **63**, 4296 (1992).
19. Model V80A from Varian, Lexington MA.

CHAPTER 7 - Picometer Displacement Tracking of an Optical Beam in a Silicon Schottky Barrier Sensor

A Ni-Si-Ni Schottky barrier sensor is used to sense 0.032 nm (0.064 nm peak-to-peak, 0.023 nm rms) displacement of an optical beam incident on the sensor. This spatial resolution is more than two orders of magnitude better than any previously reported with a simple solid-state device and approaches interferometric levels.

The displacement sensor in this report is shown in Figure 1 and is described in detail elsewhere.[1] It consists of a pair of Nickel Schottky contacts placed on a lightly doped ($\sim 10^{15}$ cm^{-3}) n-type Silicon substrate. The separation between the two electrodes may range from a few mm to tens of mm. A sensor with a planar separation of 10 μm between the Schottky contacts was utilized in our experiments. The use of this device as a highly sensitive vibration detector is demonstrated, resolving the lateral motion of an optical beam with a 0.064 nm peak-to-peak amplitude (0.023 nm rms). This resolution is over 2 orders of magnitude better than any previously reported for a solid-state device and approaches interferometric levels.

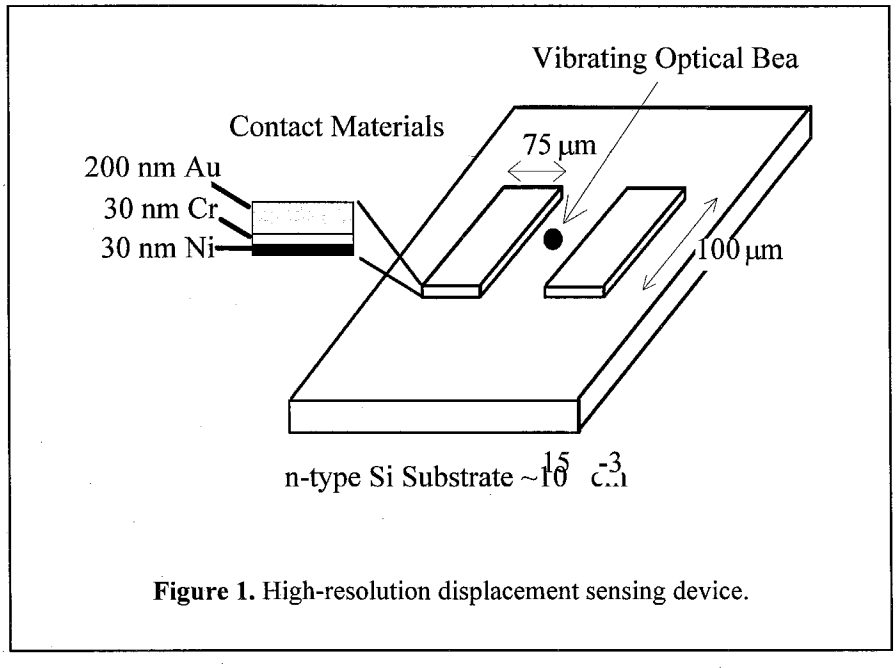

Figure 1. High-resolution displacement sensing device.

Figure 2 is a schematic of the experimental setup. A modified atomic force microscope (AFM) stage was used to perform these experiments.[2] The piezoceramic tube in the AFM was calibrated using atomic corrugations in crystalline graphite as a standard. A stimulus of 1 V across the tube corresponds to a 5.346 nm displacement. It is assumed that the tube responds linearly when driven at voltages well below 1 V.

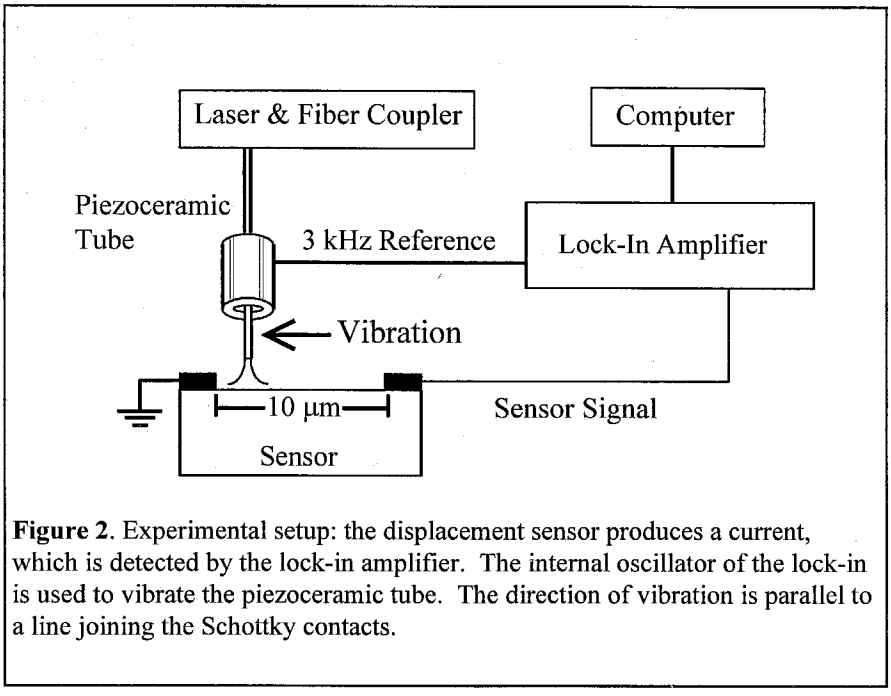

Figure 2. Experimental setup: the displacement sensor produces a current, which is detected by the lock-in amplifier. The internal oscillator of the lock-in is used to vibrate the piezoceramic tube. The direction of vibration is parallel to a line joining the Schottky contacts.

The internal oscillator of a lock-in amplifier was used to drive the piezoceramic tube. A cleaved 4-μm core diameter single mode fiber was attached to the tube. The fiber was coupled to a 1-mW HeNe laser emitting radiation at $\lambda = 633$ nm, and the sensor was illuminated with approximately 0.16 mW of power. The beam was tracked along a line bisecting the plane between the contacts, perpendicular to the contact edges. The beam waist incident on the sensor was geometrically estimated to be 6 μm, since the numerical aperture of the fiber is 0.1 and it was held approximately 20 μm from the surface.

The mechanical vibration of the light source between the two metal contacts produced an AC electrical signal at the contacts. The amplitude of the electrical signal was directly proportional to the amplitude of the vibration. Lock-in amplification was used to coherently detect the electrical signals (of known frequency and phase) in order to filter out non-reference frequency noise.

The light source was positioned near one of the Schottky contacts, producing a DC offset current of 2.6 μA. The tube holding the fiber was then vibrated at a frequency

of 3 kHz. The 3-dB bandwidth of the sensor was 2 GHz, with a linear response at 3-kHz. [1] The short circuit photo current produced by the detector was first amplified within the lock-in by a factor of 10^6 Volts/Amp. The signal was sent through a bandpass filter having a bandwidth of 1.5 kHz. The AC signal at the reference frequency was then converted to a DC voltage proportional to the amplitude. In the final stage, a low-pass filter with a bandwidth of 0.004 Hz was utilized to remove any residual noise components. This ultra-narrow filtering scheme results in very high attenuation to all but the reference frequency.

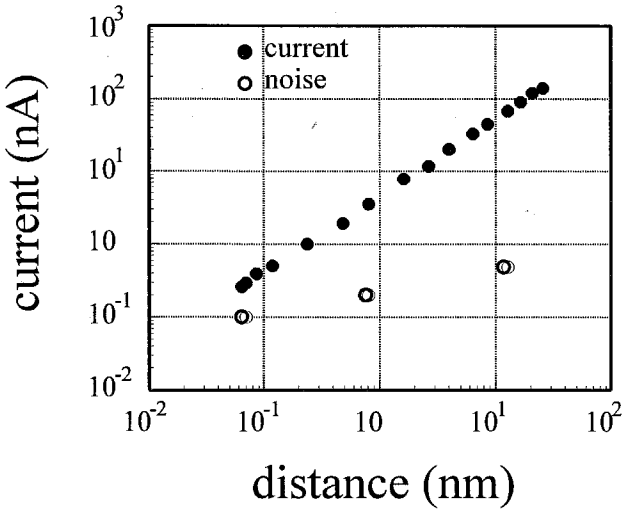

Figure 3. The amplitudes and noise levels produced by the sensor for various vibration stimuli applied to the fiber through the peizoceramic tube.

Figure 3 is a plot of the electrical amplitudes of various peak-to-peak AC signals produced by the sensor, corresponding to vibrations of the optical source. The minimum amplitude of the reference signal produced by the internal oscillator of the lock-in at 3 kHz is 12 mV peak-to-peak. The piezoceramic tube was mechanically driven by this stimulus to a vibrational amplitude of 0.064 nm. The sensor produced a 260 pA signal; the noise component at this amplitude was 100 pA.
The mechanical noise value was determined by measuring variations in the signal without vibrating the piezoceramic. 10 pA of noise contributions from the electronics was measured by driving the piezo with the laser off. This electronic noise has contributions from the amplifier and the electric field on the tube piezo coupling to the sensor. The system also behaved like an antenna, picking up stray electrical noise. The estimated shot noise for a DC offset of 2.6 μA is 55 fA,[3] which was negligible compared to the other sources of noise. Therefore, 90 % of the noise of the system (90 pA) was caused by spurious vibrations and 10 % was electronic noise within the system.

A signal to noise ratio of 10:1 was obtained with a 0.24 nm vibration. The results obtained were repeatable at various vibrational frequencies and on sensors with other contact spacings. These results will be reported elsewhere.

The mechanism for displacement sensitivity in this Schottky barrier sensor could be based on a suggestion by D. K. Donald *et al.* in which the barrier is modified by optically induced charges.[4] This was specifically observed as a "cross over" that occurs in the forward bias part of the current-voltage characteristic of a Schottky barrier photo diode when under illumination.

One possible mechanism to explain this phenomenon goes as follows: the optical beam generates electron-hole pairs in the semiconductor. The electrons move slightly faster than the holes in an ambipolar diffusion process.[5] Therefore, a residual hole density could exist near the contact that reshapes the Schottky barrier. This increase in the density of positive charges (r_+) reduces the depletion width (since $w_d \sim (1/ r_+)^{1/2}$) and changes the electric field at the contact ($E \sim 1/w_d$). The potential gradient is steeper at the contact nearest the point of injection. The barrier at the contact farther away is reshaped to a lesser degree since the diffusion progresses closer to the limit where the electrons and holes diffuse in unison. The flow of electrons and holes in this field configuration is currently under investigation and will appear in detail in a forthcoming publication.

In conclusion, the use of a simple metal-semiconductor-metal Schottky barrier photo diode as a vibration sensor capable of 0.032 nm resolution with a signal to noise ratio of 2.6 to 1 was reported. This resolution is two orders of magnitude better than any displacement sensitivity previously reported with a simple solid-state device. This displacement sensor has potential applications in high-resolution wide-bandwidth vibration sensing, photolithography, microelectronics, and high-resolution microscopy.

The sensors were constructed by S. Soares in the laboratory of Professor Steve Brueck at the University of New Mexico.

REFERENCES

1. Scott K., Sharma A., Wilson C., Mullins B., Soares S., Brueck S. Appl. Phys. Lett. **62,** 3141 (1993).
2. Baselt D. and Baldeshwieler J. RSI **64**, 908 (1993).
3. Horowitz P. Hill W. The Art of Electronics Cambridge Univ. Press, Cambridge, (1980).
4. Donal D., Wang S., Ranganath T., Newton S., Trutna W. Appl. Phys. Lett. **49**, 567 (1986).
5. Sze R. Physics of Semiconductor Devices 2nd ed. John Wiley, New York, (1981).

CHAPTER 8 - Evidence of Schottky Barrier Reshaping by Ambipolar Diffusion

The short circuit current produced by optical injection in a Schottky barrier photodiode is measured under varying intensities. Evidence suggests that the barrier is reshaped by the ambipolar diffusion of charge carriers. We assert that the drift currents associated with the optical injection are responsible for the position sensitive current measured.

Photocurrent gain has been observed in various photodiodes and contributed to a reshaping of the Schottky barrier by the optically generated carriers.[1,2] In order to explore this hypothesis, a position sensitive photodiode has been used to study the interplay between the position of optical injection, applied intensity, and the short circuit current produced. The sensor used is constructed by placing a pair of Nickel Schottky contacts a short distance apart on a lightly doped semiconductor substrate, in this case n-type Silicon doped at ~10^{15} atoms/cm^3.[3] The sensor is shown in Figure 1 of Chapter 7. As the light source is scanned laterally between the contacts, a short circuit current is measured. Scott *et al.* demonstrated very high displacement sensitivity with these sensors. Recently, 23 pm rms displacement sensitivity was reported using this device in an AC mode.[4]

The sensor used in this report is ideal for studying the diffusion of electrons and holes, since the gap is relatively small and the band gap is symmetric prior to injection. The maximum transit time for the electrons and holes to a contact is much smaller than the recombination times, for example; electrons created at the center of a 40 μm sensor will reach either contact in ~ 1.5×10^{-5} seconds, two orders of magnitude faster than the average recombination time in silicon (~ 2.5×10^{-3} s). Another advantage is the ability to alter quantitatively the injection point of the carriers relative to the contacts. Also, all of the signal generated is a result of the optically injected carriers; no interplay between traversing charges and optical injection will occur as in the previous systems studied.[1,2]

The short-circuit current produced under varying injection powers has been measured as the beam is scanned between the contacts. A 15 mW HeNe laser was coupled to a 4 μm core diameter single-mode fiber. The opposite end of the fiber was cleaved and placed a few microns above the sensor, producing a gaussian spot ~ 7 microns in diameter. This injection strategy was employed since the current produced is extremely sensitive to the position of the beam. If a focused laser beam was used as in the previous study, it would be difficult to guarantee that the initial beam position was reproducible once an attenuator was placed in the beam path. The light source was then scanned

between the two contacts using a tube piezoceramic, and the short circuit current was monitored. This procedure was repeated for multiple injection powers.

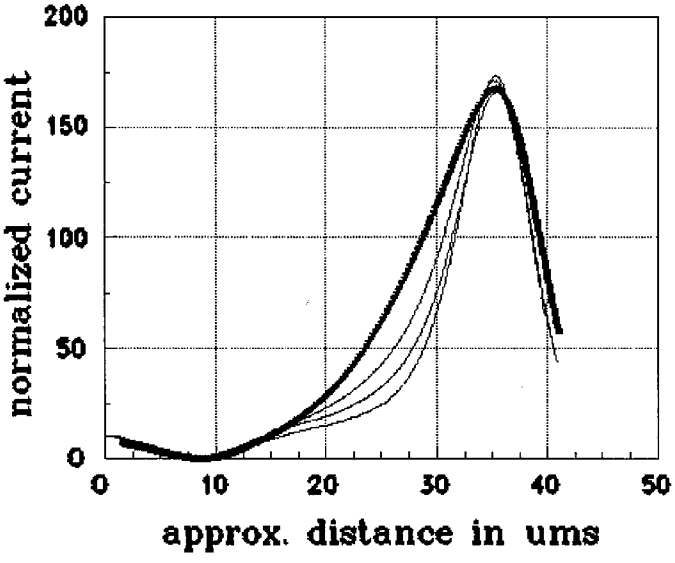

Figure 1: distance versus normalized current for 4 injection powers; the bold line is for the 5 mW injection; the other powers are consecutive in descent, *ie.* 0.5 mW > 0.05 > 0.005 at 20 μm.

Figure 1 is the data obtained at injection powers of 5, 0.5, 0.05, and 0.005 mW. The data was weighted as follows: the 0.5 mW scan was multiplied by 10,by multiplying the lower injection powers in order to normalize the input power to 5 mW (for example, the 0.005 scan was multiplied by 1000). There are three distinct regions within the plot:

1. the zero point, which occurs at the same position for all powers
2. the peaks of each slope, where the spot begins to be shadowed by the Ni contact, again at the same position for each curve
3. the region in between 1 and 2, where each line definitely exhibits different regional slopes.

The 0.005 mw plot shows a lower slope in the central region of the detector and a greater slope near the contact; the 5 mW shows the steepest accent in the center, and thus greater position sensitivity in the central region.

Prior to optical injection, the band structure between the contacts is symmetric (see Figure 2). After injection, the movement of electrons and holes will have two components: diffusion and drift. Diffusion is essentially independent of the band

structure; electrons and holes diffuse radially outward from the point of origin. The drift component will be dominated by the potential fields that are present.[5] Electrons will go down the potential lines (as drawn in the figure) and holes will go up. As the beam is offset towards one contact, the drift component of the holes is driven towards that contact by the electric field setup by the Schottky barrier; these holes recombine with electrons thermionically emitted from the nickel, producing a net flow of electrons from the nickel into the silicon. If a diffusion process was responsible for the short circuit current, the flow of electrons would be greater into the nearer contact due to the greater geometric factor at that contact. This direction of flow is not observed.

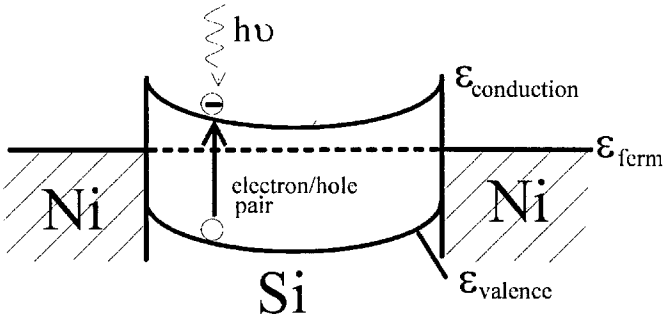

Figure 2: symmetric band diagram between the two contacts prior to reshaping.

As the intensity of light is increased, more electron-hole pairs are created and contribute to the short circuit-current. These carriers are again driven by the potential field induced by the Schottky barrier. If the potential field at the barrier remains unaltered by the optically generated carriers, the same percent of holes and electrons should reach each contact independent of the incident intensity. For example, doubling the optical power should simply double the current. As can be seen from Figure 1, this analysis only seems to apply at the geometric center of the sensor and very near the contact. Therefore, the optical carriers must be changing the shape of the Schottky barrier and therefore altering the magnitude of the potential fields throughout the gap.

We hypothesize that ambipolar diffusion of electrons and holes is responsible for this reshaping. Ambipolar diffusion is a term used to describe the velocity differences of electrons and holes. Initially, the electrons and holes have identical distributions (t_o). The electron velocities are slightly faster than the holes since the effective mass of electrons is smaller.[5] As the distributions evolve, local densities of positive and negative charges are created. Figure 3 is a steady-state representation; the carriers are contiunally being created and diffusing, however a steady-state approximation can describe their distributions at any time.

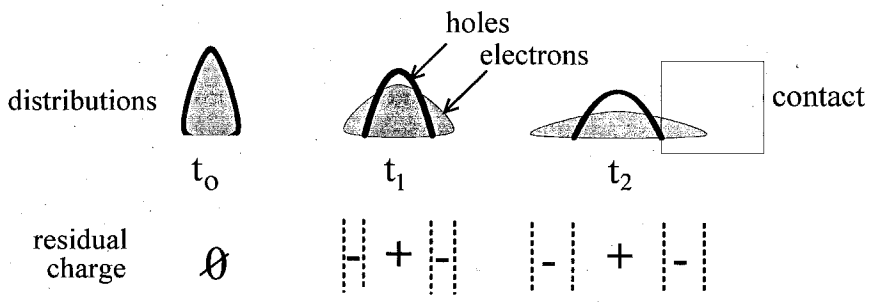

Figure 3: schematic showing the spreading of the electron/hole distrubutions with time; if a contact is superimposed as in t_2 , a residual charge density will be left in the silicon; this density will produce an electric field that will reinforce the Schottky barrier.

If one of the contacts is superimposed on the extended negative area, the electrons will be captured at the depletion region. The added residual positive charge density that remains in the silicon will have an equal and opposite image charge located at the interface in the nickel. These added positive and negative charges will reinforce the preexisting electric field at the contact and reshape the Schottky barrier. A similar reshaping will occur at the opposite contact but to a much lesser degree. The drift component of the carrier mobility will feel an even stronger force driving the holes towards the nearer contact, increasing the relative short circuit current produced.

This model would predict a greater preferential drift of carriers towards the nearer contact at the higher injection powers. Our experimental results are consistent with this assertion.

The actual short circuit current produced due to diffusion and drift of optically induced carriers will be much more complex than the qualitative model described above. However, our model based on simple principals of drift and diffusion does fit the observed data. A more detailed analysis will be developed in a forthcoming publication.

REFERENCES

1. Donal D., Wang S., Ranganath T., Newton S., Trutna W. Appl. Phys. Lett. **49**, 567 (1986).
2. Diadiuk V. and Groves S. Appl. Phys. Lett. **46**, 157 (1985).
3. Scott K., Sharma A., Wilson C., Mullins B., Soares S., Brueck S. Appl. Phys. Lett. **62,** 3141 (1993).
4. O'Connor S. and Soares S. Elec. Lett. **30**, 1844 (1994).
5. Sze R. Physics of Semiconductor Devices 2nd ed. John Wiley, New York, (1981).

CHAPTER 9 - Temperature Sensors Based on Charge Carrier Mobility in Silicon

A solid-state temperature sensor has been constructed based on charge carrier mobility in silicon. Charge carriers are optically generated between two Schottky contacts; the short-circuit photovoltage between the contacts is monitored. As the ambient temperature of the system is changed, the mobility of the carriers will be altered based on scattering theory. The total current is calibrated to changes in temperature.

Modern temperature sensing techniques are based on resistance changes in a metal or a semiconductor.[1] To measure temperature, a small bias current is passed through a resistor and the voltage is monitored. In general, the resistance of a material at any temperature (**T**) can be defined as:

$$r_t = r_o(1 + a\mathrm{T} + b\mathrm{T}^2 + c\mathrm{T}^3 + \ldots),$$

where **a**, **b**, **c**, *etc.* are constants that are experimentally determined. These thermometers are calibrated by fitting the resistance/temperature dependence to an analytical curve. This curve fitting procedure is often tedious and unreliable over large temperature ranges.

An alternative method for measuring temperature in a semiconductor sensor is to monitor changes in charge carrier mobility as a function of temperature. The conductance (σ) of a semiconducting material can be defined by:

$$\sigma = e(\mu_p p + \mu_n n),$$

where μ_p is the mobility of holes, **p** is the concentration of holes, and **e** is the charge on an electron. For lightly doped n-type silicon, the electrons will dominate the equation:

$$\sigma = \mathrm{N}_d e \mu_n$$

where $\mathbf{N}_d$ is the dopant density.[2]

The mobility of carriers in a semiconductor will be affected by two basic scattering mechanisms: lattice scattering and impurity scattering. Lattice scattering is a result of the vibration of atoms about their equilibrium position. The cross-sectional scattering area will increase with temperature. This mechanism is also referred to as phonon scattering.

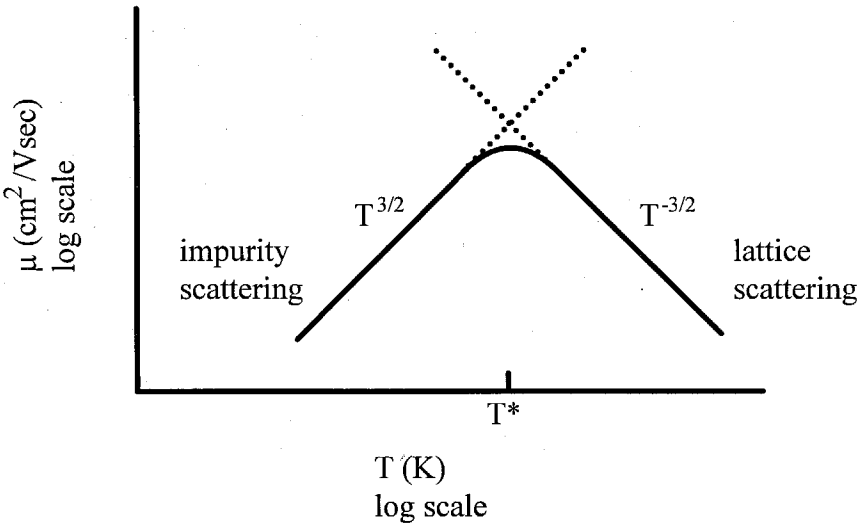

Figure 1: the effects of lattice and impurity scattering on the total electron mobility; mobility will be a maximum at T*.

At lower temperatures, scattering by lattice impurities will dominate. Charged impurities will induce an electrostatic force on the mobile electrons and holes. Since the carriers are moving with smaller momenta at low temperatures, the Coulombic forces will dominate the scattering process. Impurity scattering increases at lower temperatures and higher dopant densities.

The Schottky barrier photodiode described in Chapter 7 was used to measure temperature. The silicon substrate is lightly doped at ~ 8×10^{-14} impurities/cm^2. For this dopant density, impurity scattering should be very small over a wide temperature range and the total mobility can be approximated based on lattice scattering:

$$\mu_e(t) \approx \gamma\, T^{-3/2},$$

where γ is a constant.[3] At very low temperature, impurity scattering may begin to dominate, and a decrease in mobility may be observed.

The temperature sensing experiment was completed as follows:

- a cleaved fiber-optic was positioned just above the sensor, slightly offset from the geometric center of the contacts. This offset produced a short circuit photovoltage of ~ 50 mV @ 300°K, with ~ 0.1 mW of incident light at 633 nm.

- the fiber was fixed at this position using a symmetric invar holder and thermal epoxy.[4]

- the sensor was placed in a closed cycle refrigerator at the Advanced Cryo-Electronics Group at the Jet Propulsion Laboratory.

- the photovoltage between the two contacts was monitored as the temperature was scanned from 13°K to 373°K.

Figure 2 is a plot of the short circuit photovoltage versus temperature. A number of setpoints are used with the refrigerator and labeled on the graph. Notice the turn around point at 21°K. This turnaround could be the temperature (T*) at which impurity scattering begins to dominate the mobility process. Further studies are required to elucidate the true mechanism of mobility change over the large temperature range probed.

REFERENCES

1. Resistance thermometers are available from a number of companies including:
   Texas Instruments, Houston TX.
   Lake Shore Cryotronics Inc., Westerville OH.
   Scientific Instruments Inc., W. Palm Beach FL.
2. Sze R. Physics of Semiconductor Devices 2nd ed. John Wiley, New York, (1981).
3. Wolffenbuttel R. Sens. Act. A **22**, 639 (1990).
4. Abelstik Laboratories, Rancho Dominguez CA.

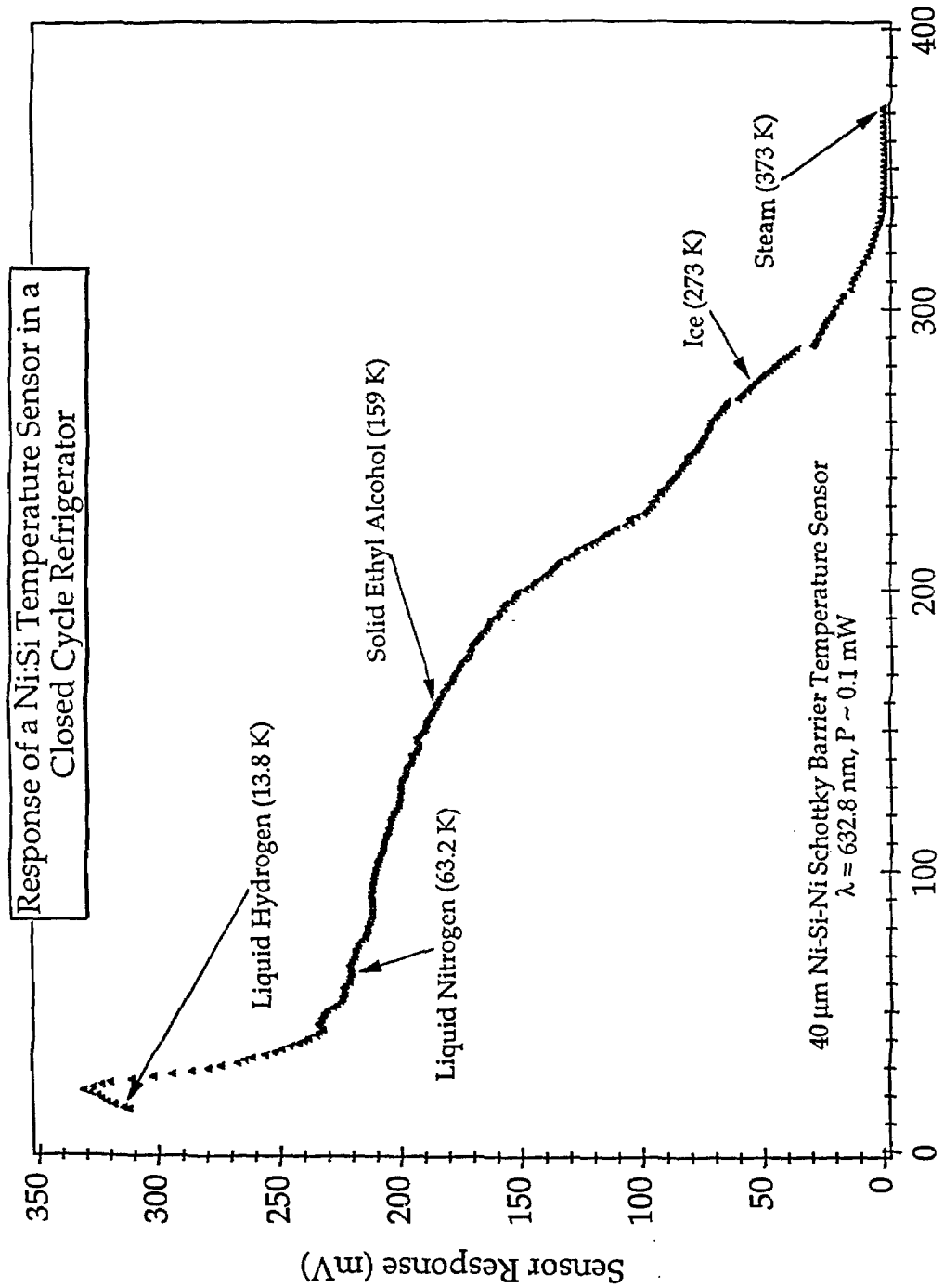
Response of a Ni:Si Temperature Sensor in a Closed Cycle Refrigerator
Liquid Hydrogen (13.8 K)
Liquid Nitrogen (63.2 K)
Solid Ethyl Alcohol (159 K)
Ice (273 K)
Steam (373 K)
40 μm Ni-Si-Ni Schottky Barrier Temperature Sensor
λ = 632.8 nm, P ~ 0.1 mW
Sensor Response (mV)
Temperature (K)
0
50
100
150
200
250
300
350
0
100
200
300
400

APPENDIX I - PROBES FOR SENSING AND MANIPULATING MICROSCOPIC ENVIRONMENTS AND STRUCTURES

FIELD OF THE INVENTION

The present invention relates generally to probes for sensing and manipulating microscopic environments and objects, and more particularly to a chemically functionalized scanning probe tip.

BACKGROUND OF THE INVENTION

Information about the microscopic three-dimensional topography of a surface may be obtained by scanning probe miscroscopy (SPM) techniques providing atomic or near-atomic resolution. The principal scanning probe microscopes are the scanning tunneling microscope (STM) and the atomic force microscope (AFM), both of which achieve the microcharacterization of materials by the use of a fine scanning probe tip. The force or current between the sample atoms and the atoms of the tip is a highly nonlinear function of their distance. For surfaces that are nearly atomically flat, the force or current between the sample and the tip is usually dominated by a single atom of the tip that happens to extend slightly more than the others. This property allows imaging of the flat surface with atomic resolution.

The SIM operates on electric principles and therefore requires both a conducting tip and a conducting sample. When the tip is positioned within a few atomic diameters of the sample and a bias voltage is applied, a small tunneling current flows between tip and sample. The tip may then be moved laterally with a piezoelectric translator to scan a surface while a computer-controlled feedback mechanism adjusts the height of the tip to maintain a constant current (constant-current mode), or the tip may be moved across the surface at a constant height while monitoring the current (constant-height mode). A surface image may be generated by plotting the tip height or current change versus the lateral position of the tip.

Atomic force microscopy relies upon atomic interactions between the tip and the sample, and has more versatility in that is requires neither a conducting tip nor a conducting sample. In atomic force microscopy, the surface of a sample is scanned by a sharp tip held at the end of an elastic member, such as a wire or cantilever base, attached at its other end to a transducer. The force between the tip and the sample due to interaction of their electron clouds deforms the elastic member and, if the member is vibrated by the transducer, changes it resonance frequency and amplitude of oscillation. The deformation or vibration is monitored using electron tunneling (using an STM), or laser interferometry, or with an optical lever, and the resulting signal may be used to drive the transducer in a feedback loop. In this manner, the surface topography of the sample may be characterized. The sensitivity of the AFM technique is such that it is also possible to

measure the chemical interactions between chemical groups on the probe surface and chemical groups on the sample surface. Thus, it is possible to obtain a chemical interaction image of the sample, which yield information about the chemical nature of the sample surface.

Other scanning probe microscopes, such as magnetic force microscopes and electrostatic force microscopes operate on analogous principles to provide microscopic surface images.

At present, most tips have a tapered shape ending with a rounded surface having a radius of curvature of 5 nm or more. Previously used materials for tips include silicon, silicon nitride, diamond, graphite, transition metal carbides and refractory metals. Such tips may be obtained by one or a combination of methods including cleaving or single crystals, chemical or electrochemical etching, and surface reactions such as anomalous dry oxidation of silicon followed by etching. The radius of curvature and the angle of taper of the tip limit the resolution of imaging of steep or low-radius-of-curvature surface features in the scanning probe microscopes known heretofore, and prevent imaging such features with atomic resolution.

Previous attempts to reduce tip size for improved resolution have focussed on electrochemical etching of traditional tip materials, particularly silicon and tungsten. U.S. Patent 5,242,541, for example, provides a method for producing single-crystal silicon tips with radii of 2 to 5 nm by a masking and etching process. The formation of tungsten tips having radii of curvature as small as 1 to 5 nm by reverse electrochemical etching has also been disclosed (Mircea Fontino, *Tip sharpening by normal and reverse electrochemical etching* 64 Rev. Scientific Instruments 159-167 (1993)). However, etching produces tips with irregular shapes, only some of which are suitable for microscopy. In order to maximize production quality and the resolution of the images obtained by the scanning probes there is still a need for scanning probe tips having regular, predictable shapes, smaller radii of curvature and greater angle of taper than currently available.

There have been few attempts to modify the chemical nature of the probe surface. The non-covalent derivatization of a silicon nitride probe tip by avidin and biotin has been demonstrated. Semi-covalent derivatization of a silicon nitride cantiliever by self-assembly of thiols on a sputtered gold surface has also been disclosed. Non-covalent attachment, however, is not sufficient, because the interaction forces between attached molecule and sample are of a comparable strength, and may detach the molecules from the probe surface. The strength of the gold-thiol bond appears nearly sufficient, but the thick layer of gold used reduces the resolution of the probe microscopy technique. Thus, there is a need for a technique which can reliably and stably functionalize probe surfaces.

Heretofore, scanning probe microscopes have been useful for sensing atomic environments. However, the present invention is advantageous in that probes are provided for functions beyond the imaging of microscopic surfaces. For example, tips

are provided by the present invention with specific functional moieties to target and/or interact with biological molecules *in vitro*, or to assist in nano-chemistry, lithography, or nanofabrication techniques.

Accordingly, an object of the present invention is to provide a method of preparing a probe tip functionalized with chemical moieties.

It is another object of the present invention to provide a method of preparing a probe tip suitable for scanning probe miscroscopy comprising a single macromolecule attached at its apex.

It is a further object of the present invention to provide methods of stiffening appropriate macromolecules, preparing a probe tip to receive a single macromolecule and securing a single macromolecule to a probe tip.

It is a further object of the present invention to provide a method of preparing a probe tip functionalized with a manipulative agent or agents.

It is yet another object of the present invention to provide a method of sensing a microscopic environment using probes prepared by the method described herein.

It is yet another object of the present invention to provide a method of manipulating a microscopic environment, object, or structure using probes prepared by the method described herein.

Additional objects and advantages of the invention will be set forth in the description which follows, and in part will be obvious from the description, or may be learned by the practice of the invention. The objects and advantages of the invention may be realized and obtained by means of the instrumentalities and combinations particularly pointed out in the claims.

SUMMARY OF THE INVENTION

The present invention is directed to methods and apparatus for a probe for sensing and/or manipulating a microscopic environment or structure. For sensing and manipulation techniques that require a probe tip which is entirely functionalized with a specific chemical moiety, the probe tip is prepared using covalent derivatization.

For sensing and manipulation techniques which require attachment of a single macromolecule, the method of preparing the probe comprises the step of protecting an area at the tip of a probe from a passivating agent, where the area is suitable for covalent linkage thereto of a single macromolecule. Preferably, this area is in the range of about 10,000 $Å^2$ to 3 $Å^2$. The tip is then contacted with a passivating agent so that its unprotected portion is passivated. The unpassivated area is then deprotected and one end

(the proximal end) of a single macromolecule is covalently attached to the unpasivated area.

For SPM with improved tip radius and aspect ratio, the attached macromolecule preferably has a substantially cylindrical or conical shape and an outer diameter at its distal (unattached) end of about 2 to 50 Å. The probe prepared according to the invention may be used to determine surface topography, or as a chemical or biochemical tool to detect or manipulate molecules or other microscopic substrates.

BRIEF DESCRIPTION OF THE DRAWINGS

The accompanying drawings, which are incorporated in and constitute a part of the specification, schematically illustrate a preferred embodiment of the invention, and together with the general description given above and the detailed description of the preferred embodiment given below, serve to explain the principles of the invention.

Figure 1A is a schematic representation of a scanning probe microscope showing the configuration of the piezoelectric tube, tip and sample used for Scanning Tunneling Microscopy.

Figure 1B is a schematic representation of a scanning probe microscopy showing the configuration of the piezoelectric tube, cantilever, tip and sample used for Scanning Force Microscopy.

Figure 1C is an enlarged view of the apex of a typical scanning probe tip known in the art.

Figure 2A is an enlarged view of the apex of a scanning probe tip, completely functionalized according to the present invention.

Figure 2B is an enlarged view of the apex of a scanning probe tip, passivated so as to protect a small area of the apex, as described in the present invention.

Figure 3 is a schematic representation of a linker molecule according to the present invention.

Figure 4 is a schematic representation of a single, rigid macromolecule according to the present invention.

Figure 5 is a schematic representation of the attachment of a single macromolecule to a scanning probe tip according to the present invention.

Figure 6 is a schematic representation of a fully assembled scanning probe tip according to the present invention.

DESCRIPTION OF THE PREFERRED EMBODIMENTS

The present invention is directed to a modified scanning probe tip, methods of preparation and methods of use thereof. The invention will be described, in part, in terms of preferred embodiments, as illustrated in the accompanying Figures.

Referring to Figure 1A, a piezoelectric tube 10 of a scanning probe microscope equipped with a conventional tip 11, is shown. The tube may be extended in the x 12, y 14 and z 16 directions to support and control the scanning probe tip 11 as it scans over the substrate 20, under control of the computer 21.

In Figure 1B, the tip 30 is at the end of a cantilever 31, by which the force on the tip may be measured. The tip 30 may be composed of silicon, silicon nitride, diamond, graphite, transitional metal carbides or refractory metals and sharpened by one or a combination of methods including cleaving of single crystals, chemical or electrochemical etching, ion million, and surface reactions such as anomalous dry oxidation of silicon followed by etching. The cantilever may be composed of silicon, silicon nitride, diamond, or metal.

Figure 1C shows an expanded view of the apex 40 of a typical scanning probe tip known in the art. The shape and sharpness of the tip is highly dependent upon the manner in which the tip is prepared.

Functionalization of the scanning probe.

Functionalization, as used herein, means the modification of a surface to terminate it with a specific chemical moiety. Depending on the functionalization method, the target moiety may be rigidly determined or freely chosen. If the target moiety may be freely chosen, it will be referred to herein as "Y".

The following are schematic representations (i, II, II, and IV) of the functionalization of the scanning probe tip according to the present invention. In these schemes 0 represents the reactive group on the substrate; A, B and X are other reactive groups used to form intermediates and Y is the target moiety, the specific chemical moiety which terminates the probe. In schemes II, III and IV, linker molecules are used, typified by the molecule of Fig. 3.

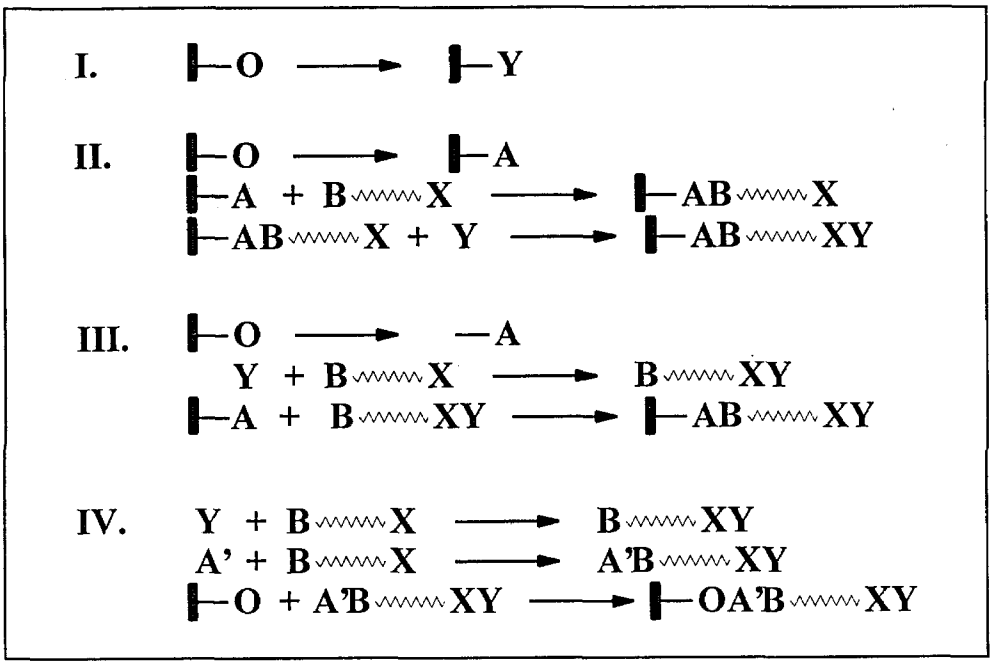

Scheme I shows a direct functionalization from the native reactive oxygen function on the surface of the probe by conversation in a single step to the desired Y function.

Scheme II is a multi-step conversion from the native probe surface oxygen function to an intermediate functional group "A" which is, in turn, reacted with a linker terminated at its distal end with a functional group "X". The group "X" is then reacted with the "Y" functional group to form the desired terminus.

Scheme III is a multi-step conversion whereby the native functional group of the probe is converted to intermediate function "A". In a separate step the desired function terminus "Y" is attached to the end of a linker. The proximal end of the linker containing functional group "B" is then reacted with the surface functional group "A" to attach the linker to the surface.

Scheme IV shows a linker having a "Y" functional terminus and the proximal end of the linker is modified with the group A' which directly reacts with the native surface functional group "O".

The two preferred materials used for the scanning force microscopy probe are silicon nitride (SI_3N_4) and silicon (Si). Both of these materials develop a layer of silicon dioxide (SiO_2) on exposure to atmospheric oxygen. Silicon dioxide is terminated with silanol groups $(So\text{-}OH)_s$, s=1-100,000. Table 1 shows the reactions of the silanol groups, indicating their target moieties.

The entire tip may be functionalized to produce a tip as shown in Fig. 2A. The tip 18 is entirely functionalized with layer 39.

Silicon and silicon nitride may also be functionalized by evaporation of a layer of gold onto the tip surface, followed by treatment with Y-alkyl-thiols, which self-assemble to form a bound Au-S-R-Y monolayer (R = alkyl) on the gold surface. Normally, the Si or Si_3N_4 surface is coated with chromium in order to enhance the adhesion of the gold layer.

Diamond surfaces may be functionalized with fluorine by treatment with fluorocarbons.

Materials used for scanning tunneling microscopy probes must be conductive, and are therefore generally metals or (doped) semiconductors.

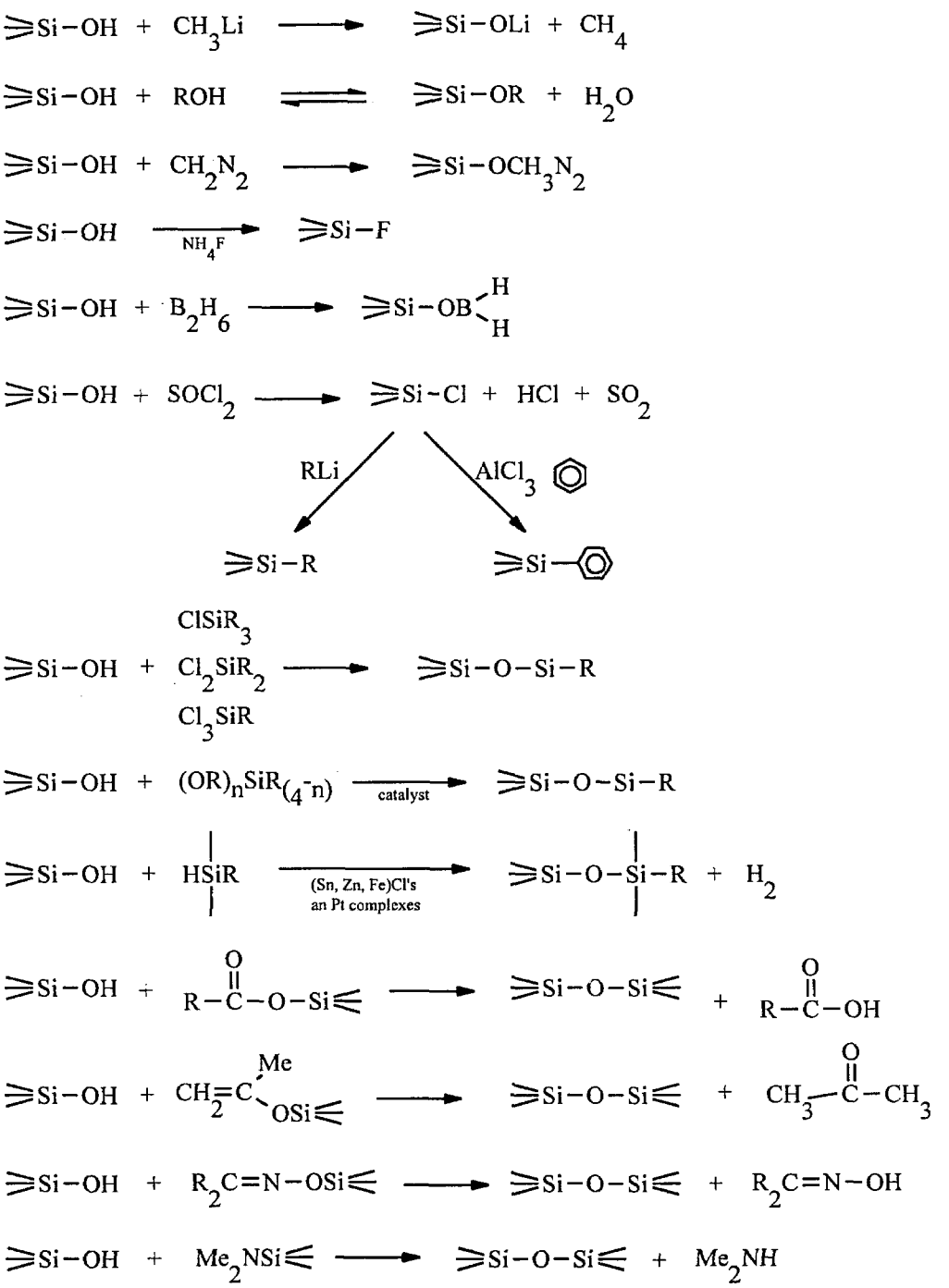

TABLE 1

Gold and silver may be functionalized by Y-alkyl-thiols, which self-assemble to form a bound Au-S-R-Y monolayer (R = alkyl) on the gold surface.

Aluminum may be functionalized by Y-alkyl phosphates of the class $N(RPO)(OH_2)_nY_{3-n}$. (R = alkyl, n = 1-100,000).

Platinum may be functionalized by treatment with molecules containing an olefinic moiety, i.e. by alkens-Y.

Titanium dioxide (TiO_2), tin dioxide (SnO_2), and ruthenium dioxide (RuO2) have an oxide coat which allows them to be silanized analogously to SiO_2. The surfaces of platinum and gold may be prepared by electrochemical means to have an oxide coat within similar reactivity. In general, any substance with a surface terminated with hydroxyl (-OH) groups may be silanized in like fashion.

Example 1: Stepwise-Out Functionalization

A silicon scanning probe is functionalized with single-stranded DNA as follows: The surface of the silicon probe is derivatized by immersion in a 2% solution of aminopropyltriethoxysilane (APTS) in anhydrous toluene for 1 hour, yielding on amino (-NH_2) group covalently bound to the surface. 10 mg disuccinimidyl suberate (DSS) is dissolved in 600 mL DMSO. A solution of 21 mL aminopentanol in 5.4 mL of 1xPBS buffer is prepared, and the DSS solution is added to it. The resulting solution is stirred for 10 minutes. The probe is added to this solution, and the solution is stirred for 10 minutes. The results is a surface of -OH groups at the end of long spacer arms. This is the starting point for conventional automated solid-phase DNA synthesis. We have replaced the glass beads which are normally the substrate with the scanning probe. The scanning probe chip fits easily within a standard DNA synthesis fritted filter chamber.

The functionalization proceeds stepwise, starting from the probe surface and working out, as shown by the following scheme:

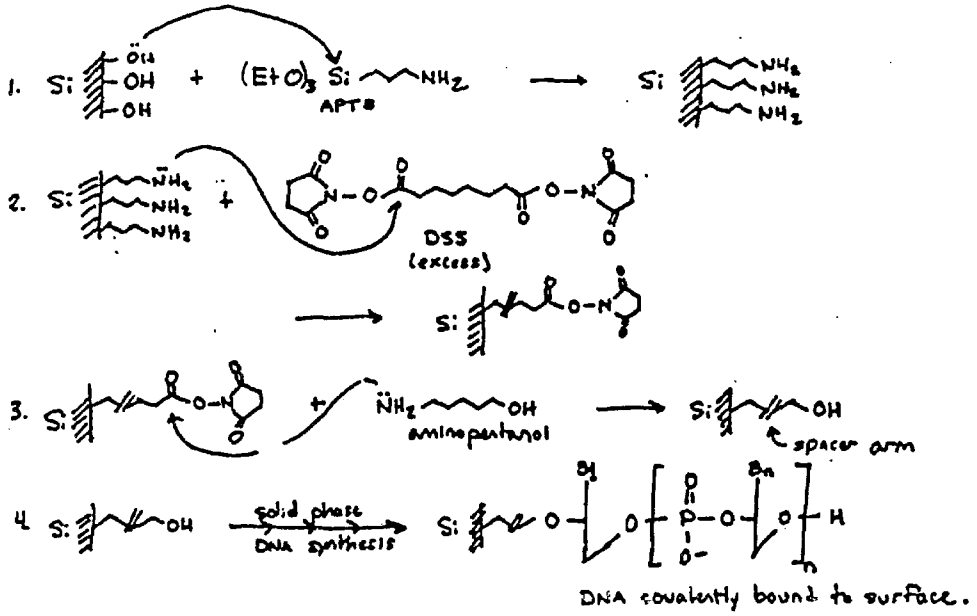

Example 2: Convergent Functionalization

A silicon nitride scanning probe is functionalized with a peptide epitope sequence as follows: A thin (30 Å) layer of chrominum is evaporated onto the probe, followed by a thin (100 Å) layer of gold. A peptide epitope sequence (for instance, enkephalin, Tyr-Gly-Gly-Phe, or human endorphin, Tyr-Gly-Gly-Phe-Met-Thr-Ser-Glue-Lys-Ser-Gln-Thr-Pro-Leu-Val-Thr-Leu-Phe-Lys-Ans-Ala0Ile-Ile-Lys-Asn-Al-Tyr-Lys-Gly-Glu) is synthesized using solid-phase Merrifield synthesis such that all amino-containing side chains are protected. The peptide is released from its solid phase support, and treated with a 5mM solution of Traut's Reagent (2-iminothiolane·HCl), which converts the amino-terminus of the protein to a sulfhydryl terminus. The probe is then added to a 3% solution of this sulfhydryl-derivatized epitope in ethanol and the solution is stirred for 3 hours. The derivatized epitope self-assembles on the gold-coated probe. Finally, the protecting groups on the side-chain amino groups are removed.

In the following scheme both the surface and the target moiety are modified separately, and the two are brought together to create the functionalized surface. This is a convergent synthesis:

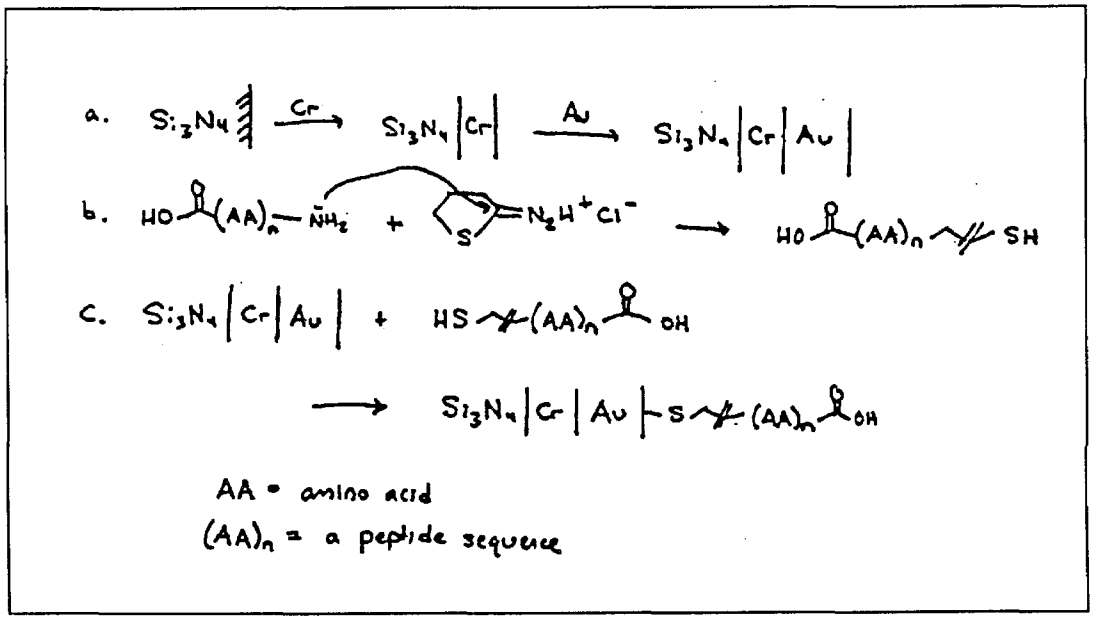

Example 3: Conduction through covalent bonds

A platinum scanning probe is functionalized with an electroactive reagent (for instance, allhydroquinone) as follows: the Pt probe is cleaned of organic contaminants by heating in a methane-oxygen flame for 10 minutes with repeated quenching in perchloric acid. Final cleaning is achieved by applying a cyclic potential (2mV/s, from 0.4 V to 1.3 V, then to -0.4 V and finally to 0.4 V vs NaCe) in 1M HclO4. The probe is then immersed for 5 minutes in a 10mM solution of the electroactive reagent in pure water.

This functionalized moiety can be oxidized and reduced by application of a potential to the scanning probe, showing that the covalent bonds connection it to the platinum probe are electrically conductive.

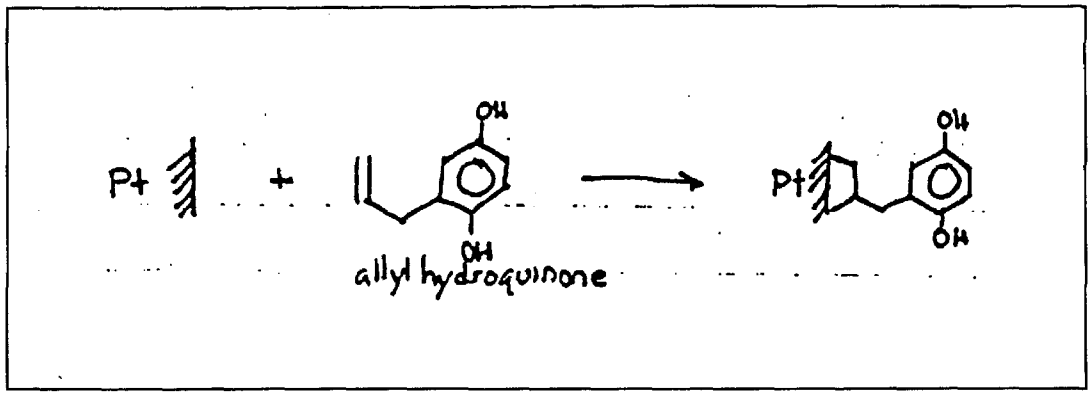

Passivation of the scanning probe.

Passivation, as used herein, means the protection by way of a layer on or by chemical, optical, or electric treatment of a substrate surface to isolate the substrate from electrical and chemical conditions in the environment.

Functionalization to a chemically unreactive moiety is one way to implement passivation. Therefore, for tips of silicon and silicon nitride, passivation methods useful in the present invention include treatment with diazomethane, fluorination, chlorination followed by alkylation or arylation, silanization to alkyl groups, hydrosilylation to alkyl groups, or treatment with acloxy-, enoxy-, oxime-, alkoxy-, or amine- organosilanes.

Other means of applying passivation layers include low pressure chemical vapor deposition (LPCVD), as described in U.S. Patent No. 5,250,473, thermal oxidation, and direct oxidation of the substrate by exposure to oxidizing agents.

Example 4: Passivation of methyl-functionalization

The surface of a silicon scanning probe may be passivated with methyl groups as follows: the probe is immersed in 2% solution of trimethylchlorosilane (TMCS) in dry benzene for 1 hour.

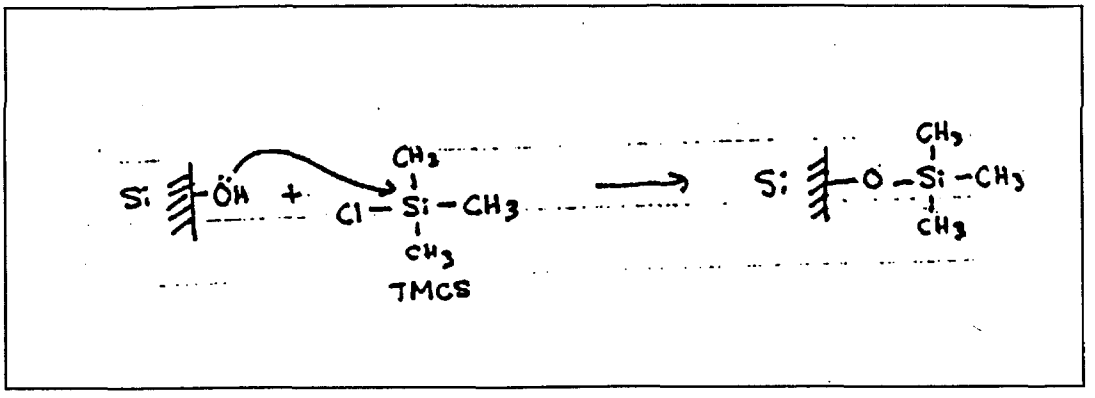

Example 5: Passivation of alkyl-functionalization

The surface of a platinum scanning probe may be passivated as follows: the probe is cleaned as described in example 3, and then functionalized by immersion in a 10mM solution 1-octene for 5 minutes.

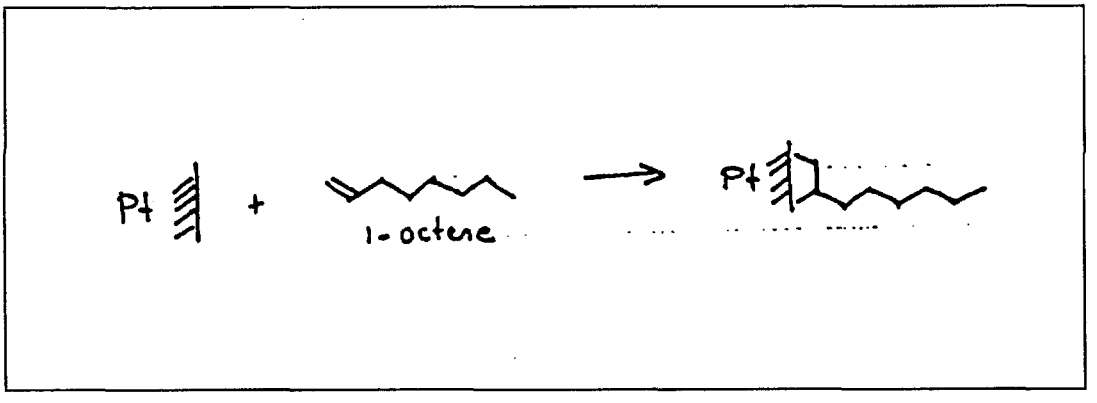

Tip-Apex Functionalization

The ability to attach a single macromolecule to, or specifically functionalize a small area of, the apex of an SPM tip depends on the ability to physically differentiate the apex from the remainder of the tip, and to cause chemical change based on that differentiation. Since the area is desired to be on the order of molecular dimensions, the physical effects used must be very short-range, capable of affecting one area while leaving another, relatively few atomic distances away, unchanged. There are many ways to do this, including employed steric control, evanescent waves, electron tunneling, or lithographic techniques.

Differentiate by Steric Control

Steric interactions (inter-atomic repulsion at short distances) are extremely short range. This type of interaction can be used to block a reagent from the apex of an SPM tip, or to confine a reagent to the apex.

Differentiate by Applied Potential:

Application of an electrical potential between a sharp tip and a substrate creates highly nonhomogenous electric fields which are extremely intense near the apex of the tip. Magnetic fields at sharp tips are similarly nonhomogenous and intense at the tip apex. Thus, these fields can be used to guide ions or electrons onto a small area at the apex, to selectively functionalize or passivate the tip. The strong fields may also activate or deactivate chemical groups towards a particular reaction pathway.

Differentiate with Lithographic Techniques:

Lithographic techniques to differentiate the tip from other surfaces on the probe depend on lateral, differentiation (along the surface of the probe), rather than vertical differentiation as implied in the evanescent wave and electron tunneling techniques.

Apex differentiation may constitute either activation towards, or protection from, chemical change.

Methods based on apex activation have three steps:

1. Activation of a small area at the apex of the scanning probe towards functionalization.
2. Functionalization of said area with a desired macromolecule according to the present invention.
3. Passivation of the non-activated area of said tip according to the present invention (if necessary).

Methods based on apex protection have four steps:

1. Protection of a small area at the apex of the scanning probe tip from passivation.
2. Passivation of the unprotected area of said probe tip according to the present invention.
3. Deprotection of the protected area at the apex of said tip.
4. Functionalization of said area with a desired macromolecule.

Referring to Figure 4, the protection (i.) of a small area 40 at the apex of the scanning probe tip 42 may be accomplished by bringing the small area into close proximity with a substrate surface 41, (ii). such that the molecules 43 of the passivating agent are sterically impeded from contact with the small area at the apex of the tip. Passivation layer 44 is

formed at other unprotected areas. This can be seen in more detail in Fig. 2B. As an example, if the passivating agent comprises molecules of effective maximum diameter of 20 Å, the apex may be located next to the surface such that the space inbetween is much less than 20 Å. Deprotection (iii.) is accomplished by simply withdrawing the probe tip 42 from the substrate 41. Functionalization (iv.) can then proceed using the specialized molecules 45 designed to attach at the unpassivated tip. A typical rigid molecule 45 is shown in Fig. 4.

Differentiate with an Evanescent Wave:

The intensity of an evanescent wave at a flat surface falls off exponentially with distance. A more complicated optical field is created at an aperture smaller than the wavelength of light, with an intensity that may fall off even faster than the evanescent wave at a flat surface. This exponential falloff can be used to differentiate an area at the apex from the remainder of the tip. Since intensity of an evanescent wave decreases exponentially with distance, the probability of reaction of a photoactive group on the probe surface also decreases exponentially with distance from the surface.

Differentiate by Electron Tunnelling:

The probability of electron tunnelling also falls off exponentially with distance. Electro-active (redox) groups on the apex can thus be differentiated by proximity to the substrate. Electron transfer between the electrode and redox-active groups on the probe surface leads to oxidation or reduction of the redox-active groups. Since electron transfer occurs by quantum-mechanical tunneling, the probability of electron transfer decreases exponentially with distance.

The number of electrons that tunnel may also be controlled by controlling the applied potential and the number of electrons available at the tunneling site.

After the passivation procedure, the small unpassivated area remaining at the apex of the tip is preferably in the range of about 10000 Å to 3 $Å^2$. It will be realized that the size of area may vary and is controlled by the shape of the tip, and the proximity to and local topography of the substrate surface, or the masking process. However, a small unpassivated area at the substrate tip enhances the probability of attachment thereto of only one macromolecule.

The macromolecule will be attached to the substrate probe tip material in a manner which restricts motion with respect to the substrate. Thus, preferably, there should be a plurality of sites of attachment.

Example 6: Apex Assembly of a Single Enzyme Molecule Tip

The apex of a silicon nitride scanning probe may be functionalized with a single molecule of an enzyme (for instance Horseradish Peroxidase, molecule eight 44,000) as follows: A

silicon nitride probe is mounted in a SPM liquid cell. The apex of a silicon nitride scanning probe is brought into close proximity with a graphite surface, as described above. The unprotected surface is then passivated by filling the liquid cell with a 2% solution of TMCS in anhydrous toluene and allowing reaction for 1 hour. At the end of this period, the probe tip is withdrawn from the surface and the apex is derivatized by filling the liquid cell with a 2% solution for APTS in anhydrous toluene and allowing reaction for 1 hour. This yields an apex derivatized covalently with amino groups. The probe is then removed from the liquid cell, and the remaining reaction steps are carried out as for functionalization of an entire scanning probe. A solution of 100mg DSS / 1mL DMSO is prepared, and the scanning probe is stirred in it for 10 minutes. The resulting groups are highly reactive toward amino groups. The probe is removed from the DSS/DMSO solution, rinsed with DMSO to remove excess DSS, and placed in a solution of 3% enzyme in ethanol, where it is allowed to react for 1 hour. Finally, the probe is washed with ethanol and distilled water to remove excess enzyme.

As may be seen from the scheme, the functionalization proceeds stepwise, starting from the probe surface and working out.

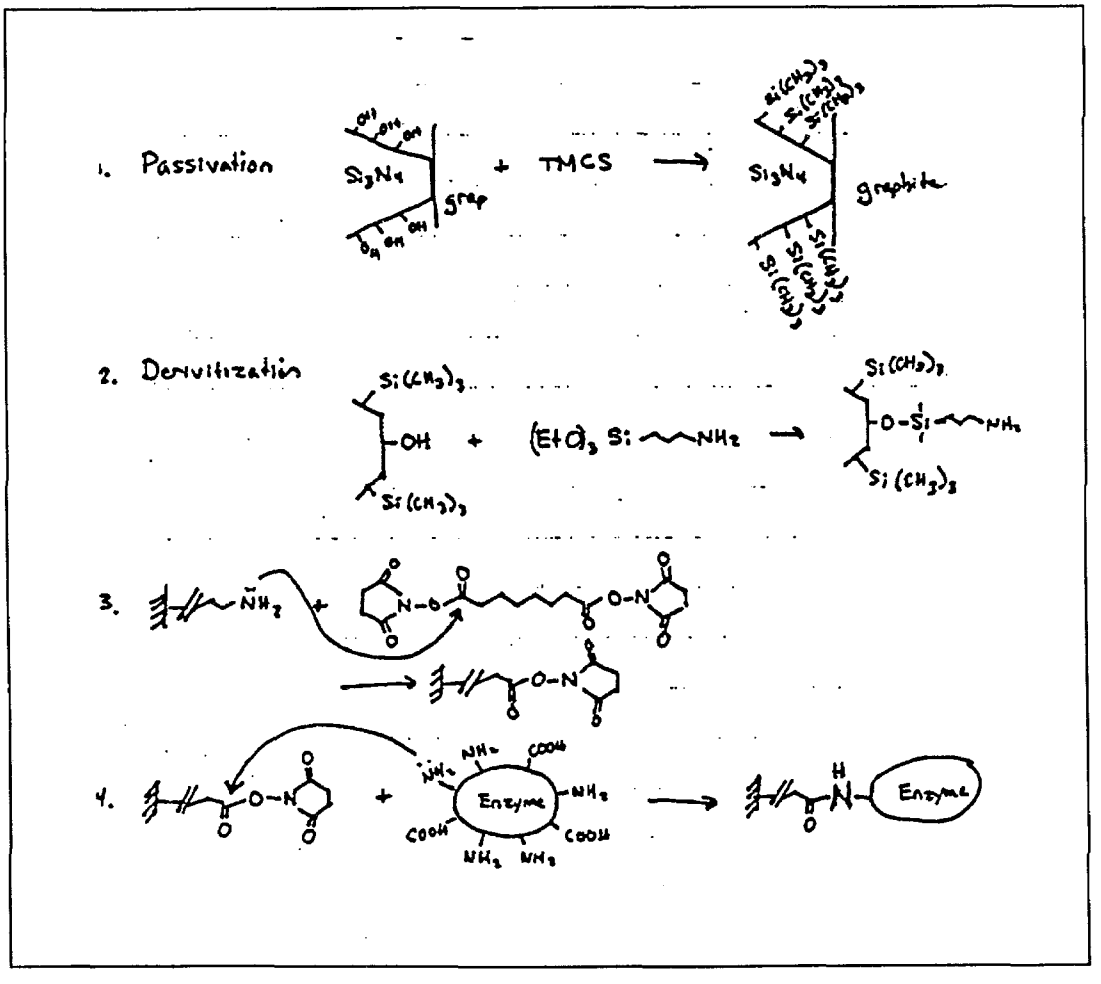

Example 7: Apex Assembly of a Polypeptide Nanotubule Tip

The apex of a silicon nitride scanning probe may be functionalized with a single polypeptide nanotuble as follows: A silicon nitride probe is protected with TMCS and its apex derivatized with APTS as described in example 6. The cyclic polypeptide cylo[-(D-Leu-Glu-D-Leu-Glu)$_2$] is prepared by the method of Ghadiri *et al.* (Nature **366**, 324 (1993)). Aggregation of this polypeptide is stabilized axially by hydrogen bonds between backbone units and potentially by Van der Waals interactions between the isoleucine side groups. In contrast to the polypeptide of Ghadiri *et al.*, however, lateral association is discouraged, both because of the steric bulk of the isoleucine side groups and because no amino side chains are present to form hydrogen bonds. Self-assembly occurs as pH is reduced.

A single polypeptide nanotube is anchored to the amino apex covalently as follows: a 10 mM solution 1-ethyl-3-(3-dimethylaminopropyl)-carbodiimide hydrochloride (EDC) in aqueous buffer at pH 7 is prepared. 1% by weight of polypeptide is added. The EDC activates the carboxylic acid groups of the glutamic acid side chains for attack by amino groups. After dissolution of the peptide, the probe chip is added and allowed to react for 1 hour. The amino groups on the apex form amide bonds with a polypeptide, anchoring it to the surface. The probe is washed with aqueous buffer solution at pH 9 to remove excess peptide, and then immersed in a fresh solution of 1% polypeptide at pH 7. The pH of the solution is gradually lowered by addition of dilute HCl to allow the polypeptide nanotubule to self-assemble.

As may be seen from the scheme, both the surface and the target are modified separately and then brought together to create the functionalized apex. This is a convergent synthesis.

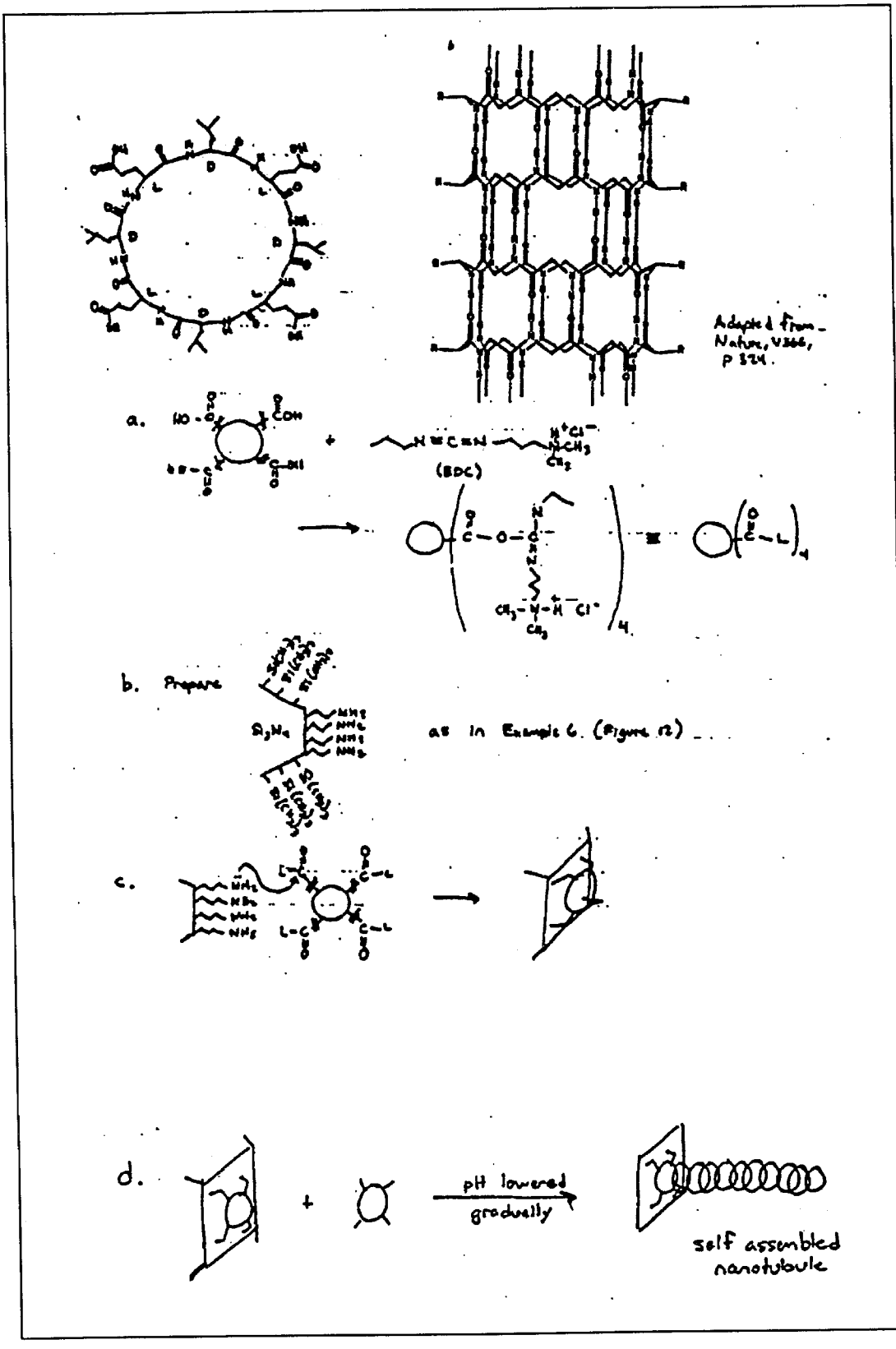
Adapted from Nature, V366, P324.
a.
(EDC)
b. Prepare
as in Example 6. (Figure 12)
c.
d.
pH lowered gradually
self assembled nanotubule

Example 8: Apex Assembly of a DNA Double Helix on a Pt Probe

The apex of a platinum scanning probe may be functionalized with a DNA double helix as follows: the probe is cleaned as described in example 3, and then mounted in an SPM liquid cell. The apex of the probe is brought into close proximity to a mica substrate, as described above. The unprotected surface is then passivated by filling the liquid cell with a 10mM solution of 1-pentane in anhydrous pentane and allowing reaction for 5 minutes. The liquid cell is flushed with anhydrous pentane, then with acetonitrile, then with pure water, then filled with a 10mM solution of the vinyl-derivatized double helix (prepared as described below) in water. The probe is withdrawn from the surface and allowed to react for 10 minutes, after which the liquid cell is flushed with pure water.

The 2-aminobutyl-1,3-propanediol (ABPD) structure shown in the Figure replaces a normal DNA base in a strand of DNA. The DMT-protected phosphoramidite based on the ABPD structure (SBPD-PA) is a perfect chemical replacement for a DMT-protected nucleotide phosphoramidite in automated solid-phase synthesis of DNA; it undergoes the same addition, deprotection, capping, and chain extension reactions. The amino-terminated "side chain" or ABPD-PA can also be derivatized, and this is how the DNA double helix will be attached.

A 100mM solution of ABPD-PA in anhydrous acetonitrile is prepared. To this is added an equal amount of 1M 1-vinyl-2-pyrrolidionone (VPD) in acetonitrile, and the reaction is allowed to proceed for 30 minutes. This terminates the side chain of ABPD-PA with a vinyl group (ABPD-PA-V). The reaction mixture is purified by column chromatography and the ABPD-PA-V fraction is retained.

The desired sequence of DNA and its complement are synthesized by automated solid-phase synthesis. On one strand, additional 3' and 3'+1 residues are inserted; there are ABPD-PA-V. On the complementary strand, additional 5'-1 and 5' residues are added; these are also ABPD-PA-V. This yields a DNA double-helix with four double bonds capable of covalent bond fraction with the surface. The complementary strands are hybridized together.

As may be seen from the scheme, the derivatized DNA double-helix is created entirely separately from the surface, and then attached as a final step. The functionalization proceeds stepwise, starting with the ABPD-PA and working in.

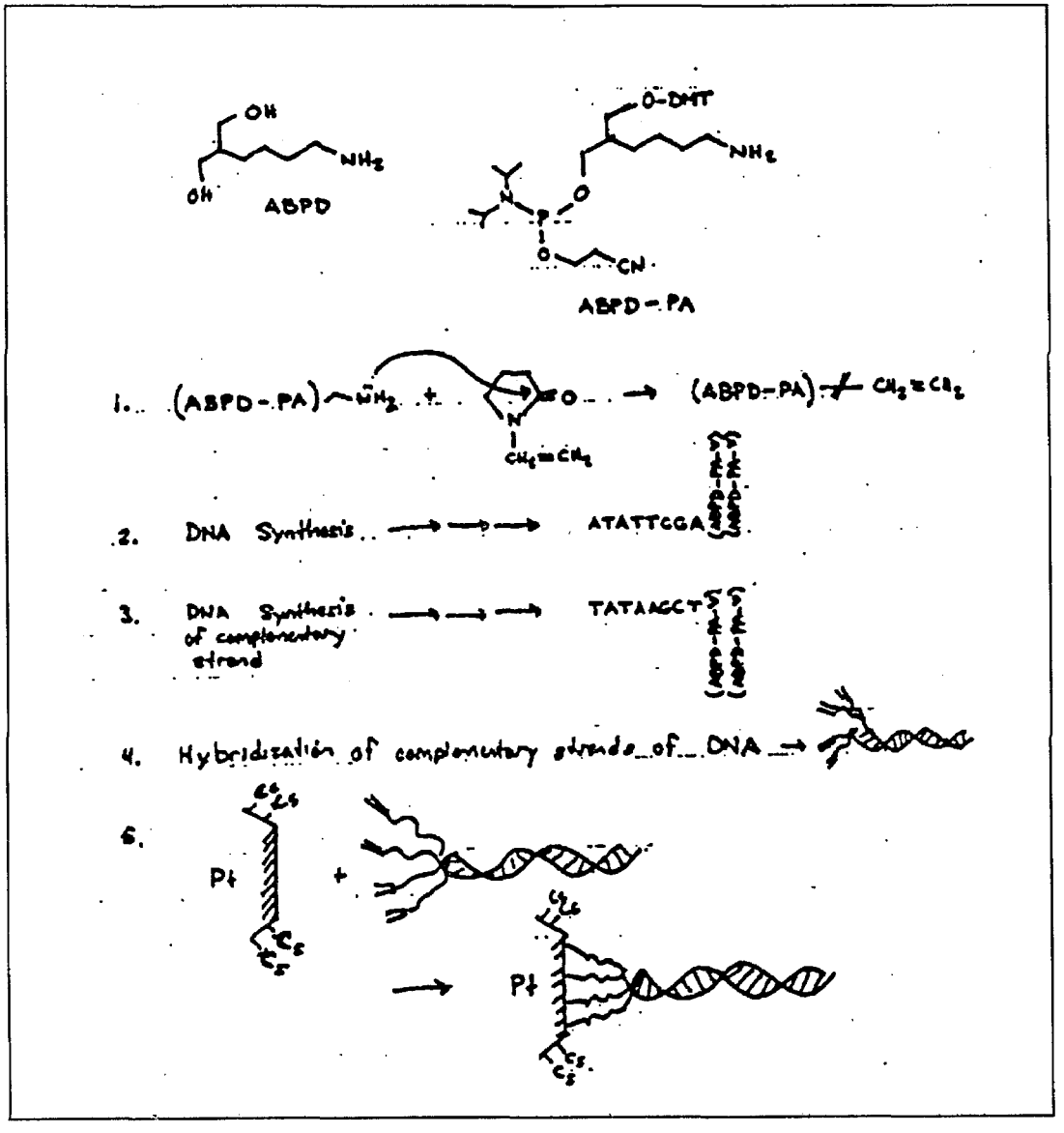

EXAMPLE 9: Differentiation by Steric Control by blocking a passivation reagent from reaching the apex

Use steric control to constrain a masking agent to the apex.

1. Touch tip apex down on the surface, flow in passivation solution, rinse, retract.

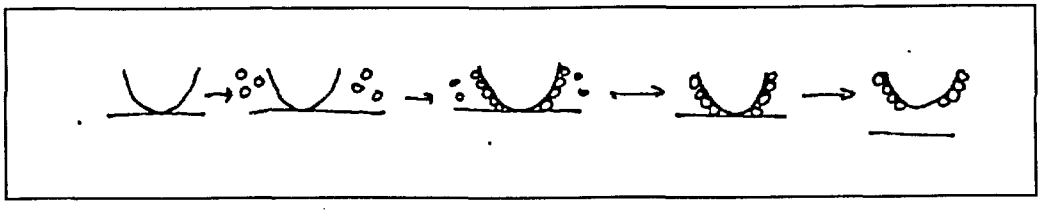

2. Alternatively, touch tip apex down on surface through a drop of passivation solution. Typically, the slow chemical kinetics of passivation prevent apex passivation.

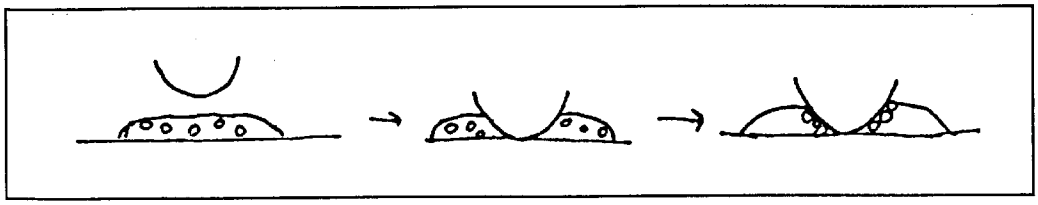

3. Alternatively, touch tip apex on surface through an electroactivatable passivation solution; then
   - electroactivate the solution with an external electrode, or
   - electroactivate with the tip as an electrode, or
   - electroactivate with the substrate as an electrode.
4. Alternatively, touch tip apex down through a heat-activatable passivation solution, then
   - heat solution from the tip, or
   - heat solution from the substrate, or
   - heat with an external probe, or
   - heat with a laser

4a. Alternatively, touch tip apex down through a light-activatable passivation solution. Then, light from tip, substrate, probe, laser etc.

5. Alternatively, tip apex down, then electrochemically passivate the tip. Note that this is different than 3. In 3, same species in solution is activated, A, to an activated species A* which can then passivate the surface. In 5, a species is oxidized or reduced on the surface of the tip in such a fashion that it can be oxidized or reduced only with another species present in solution. In 3, A* is blocked from reaching the apex whereas in 5 a necessary solution reagent NH is blocked from reaching S* on the surface.
6. Alternatively tough down the tip apex, then light-passive tip (same principle as in 5).
7. Alternatively touch down the tip apex, the heat-passivate tip (same principle as in 5).

EXAMPLE 10: Differentiation by steric control to constrain an activation agent to the apex

1. Touch down tip into an aperture filled with an activation reagent/functionalization reagent:

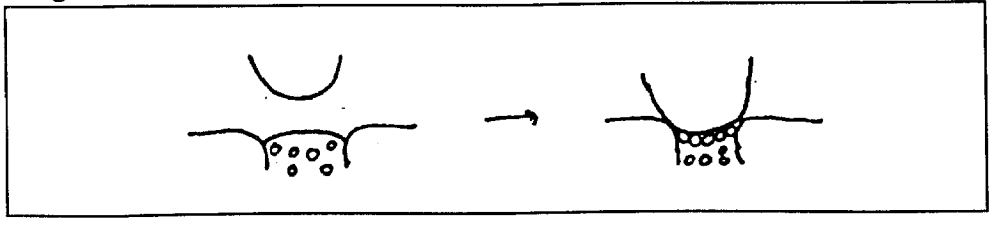

The activation/functionalization reagent may be electroactivate, photoactivated, or heat-activated.

2. In a solution containing electroactivateable reagent, touch down on an aperture where electroactivation may selectively occur. The reagent may be photoactivated or heat-activated.

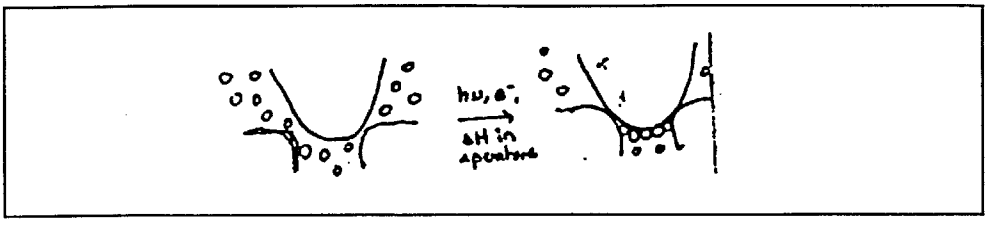

3. Town down on a catalytic surface (for example, to reduce $-NO_2$ groups to $-NH_2$ groups with Pd.)
4. Touch down on a surface which chemically reacts with groups on the apex to activate or functionalize the apex.

EXAMPLE 11: Differentiation by steric control to constrain a masking agent from the apex

1. Touch down on a surface to transfer a temporary masking agent to the apex.

EXAMPLE 12: Differentiation by (Evanescent) Photon Control

To photoactivate a reaction (i.e., cause a photochemical change) with light at this to apex, one takes advantage of the exponential distance dependence of evanescent waves.

1. Touch tip down at a surface where a wave is undergoing total internal reflection.

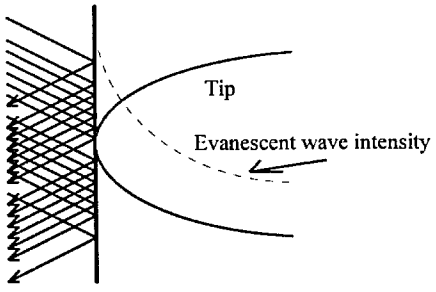

2. Alternatively, touch tip down at an aperture smaller than the wavelength of light.

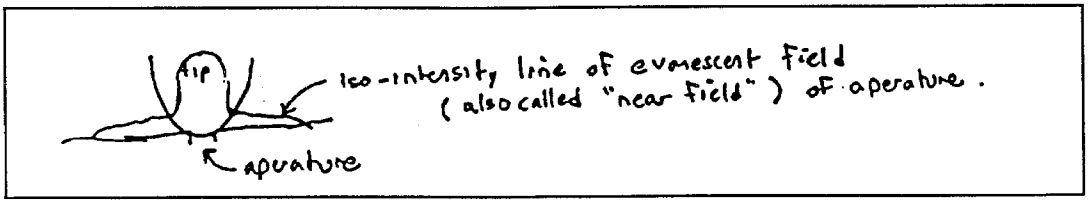

3. Alternatively, the near-field light of a pulled-optical-fiber near-field scanning optical microscope tip (NSOM tip) may be used to photochemically alter the apex of the tip.

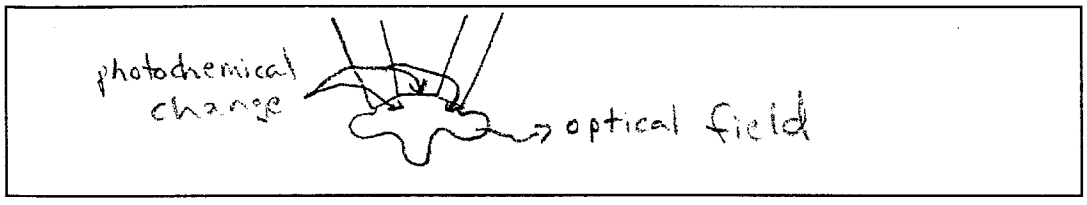

EXAMPLE 13: Differentiation by non-evanescent photon control

1. A tip is brought close to the surface and irradiated with light of high intensity, having a wavelength too long to cause the desired photoreaction. Second-harmonic generation at the tip-sample interface will double frequency (half-wavelength) of some of the light. This frequency-doubled light can cause photochemical change which the original light could not, due to higher energy per photon.
2. Alternatively, bring the tip down to a point source of light of the required wavelength to activate
   - a frequency-"upping" molecule, or
   - an electroactivateable luminescent molecule

EXAMPLE 14: Differentiation by (Tunneling) Electron Control

Specificity of an electrochemical change to the apex comes about through exponential distance dependence of tunneling probability of electrons. For specificity one should limit the number of e-transferred in an electrochemical cell. Therefore, a limited electron source/drain (a "limited e-sink") for this purpose can be provided as follows.

1-6. Either electroactivate groups on apex, with an unlimited e- sink or source, limited e-sink or source or null sink or source, or electroprotect the substrate connected to an unlimited e- sink or source, limited e- sink or source or null sink or source.
7. Connect to sink/source as in 1-6 above, but with the tip in contact, instead of in the tunneling region.
8. Connect to sink/source as in 1-7, but with electron-transfer chemical groups on the substrate.
9. Connect to sink/source as in 8, where the electron-transfer groups are spatially limited.
10. Contact sink where the applied voltage is varied with time.

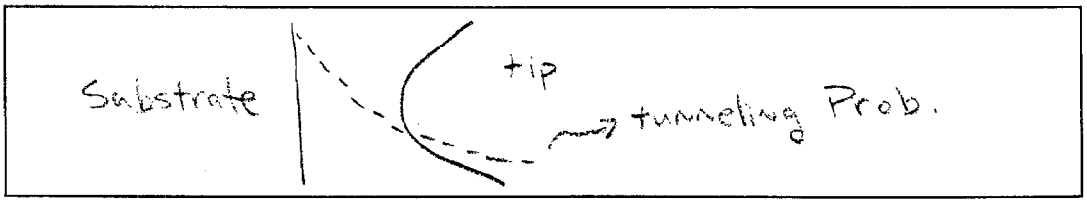

EXAMPLE 15: Limited electron sinks/sources

The following sinks/sources are all drawn with e- transferred from substrate to tip, but the extension to e- transfer from tip to angle is apparent.

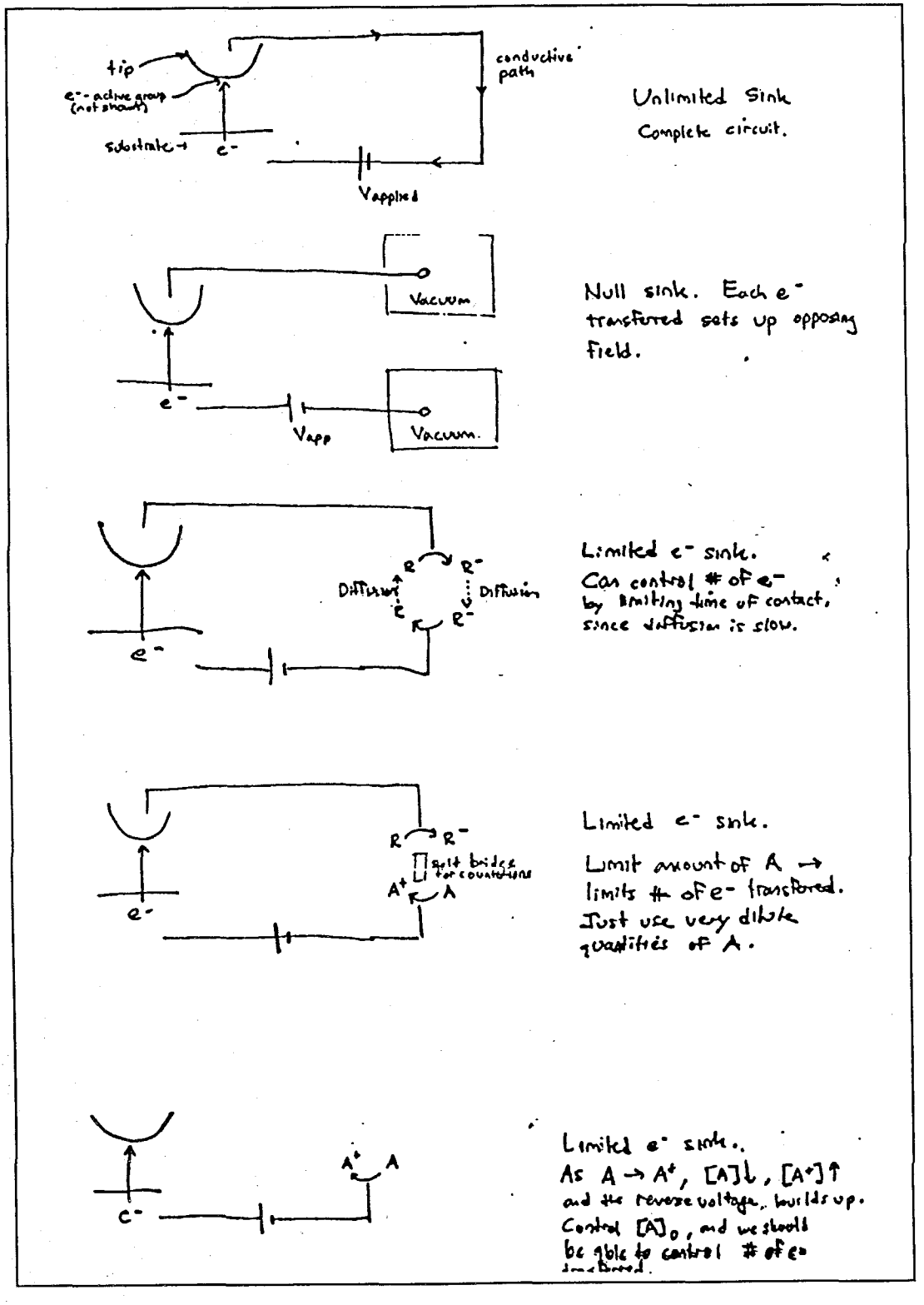

EXAMPLE 16: Differentiation by Applied Fields

As applied field is utilized to single out the apex. These are essentially static fields which are not extremely-fast-oscillating fields like an EM wave (light):

1. A chemical change is induced by field ionization at the apex.
2. A chemical change is induced by high field intensity. For example, if the high field lowers the energy of the transition state of a chemical reaction, ionization is not necessary.
3. As 1., but assisted with applied light or heat.
4. As 2., but assisted with applied heat or light.
5. Chemical change is induced by ion or e-collision, where the ions or e- are guided to the apex by an applied field.
6. Ionize the apex with a field, then guide ions to apex.

EXAMPLE 17: Differentiation by Lithographic Techniques

1. A (positive) resist is applied, patterned with light or e-, and unexposed resist is removed. The tip is passivated, the exposed resist is removed, and the exposed surface is functionalized.

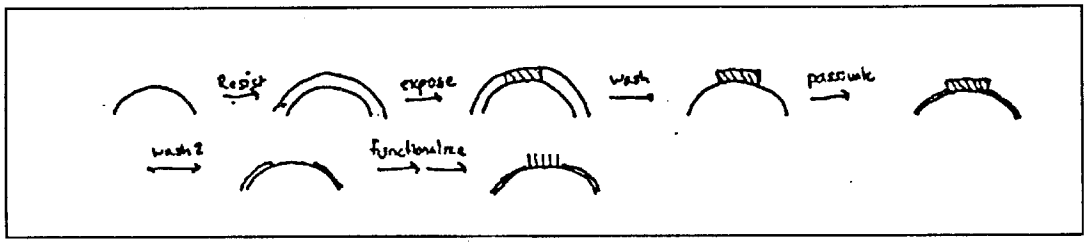

2. A (negative) resist is applied, patterned with light or e-, and the unexposed resist is removed. The exposed surface is functionalized. The exposed resist is removed if necessary.

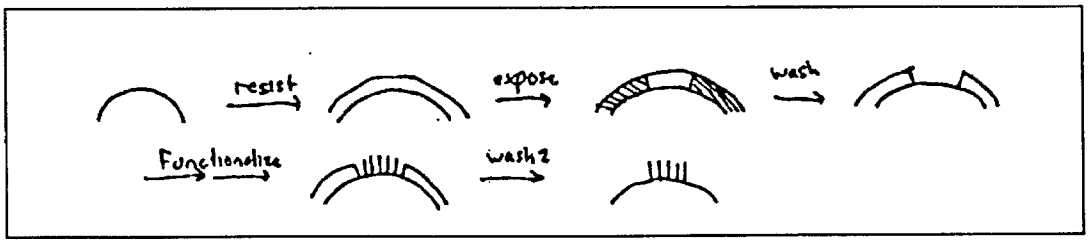

3. Alternatively, proceed as 1, but with a negative result and expose the tip except for the apex.
4. Alternatively, proceed as 2, but with a positive result and expose the tip except for the apex.

5. Alternatively, proceed as 2 and 3, but with a negative resist of electro- or photo-sensitive molecules which on exposure react to leave the exposed area derivatizeable.
6. Alternatively, functionalize entire tip with photo- or electrosensitive target molecule. Irradiate all areas except for apex to remove the target molecule from all sites except the apex.

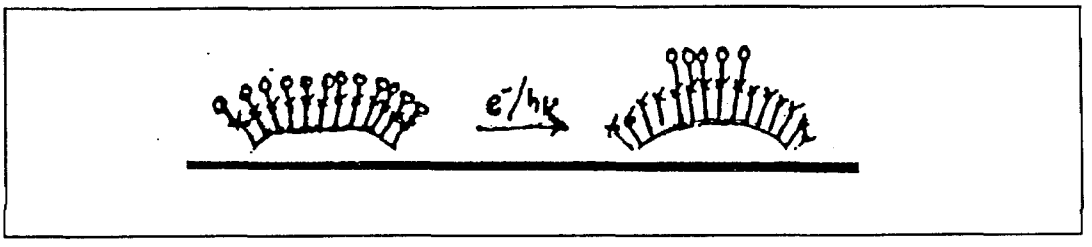

Tip macromolecule.

Referring to figure 6, the macromolecule 45 needs to be sufficiently rigid after attachment to the tip 42 in order to avoid undesired displacement which is not under control of the computer-controlled mechanism for moving the tip. Hence, complex molecules which are cross-linked, folded or otherwise restricted in degrees of freedom around covalent bonds are required. Such molecules include, but are not limited to, single-wall carbon nanotubes, deoxyribonucleic acid (DNA) double helices, polymeric nanotubes composed of sugar molecules, cyclic peptide nanotubes, proteins, and synthetically constructed macromolecular structures. Nanotubes are molecular structures stacked or coiled to form tubular shapes. Protein structures may be locked by cross-linking or by inserting metal atoms to chelate internal groups.

Single-wall carbon nanotubes having typical diameters of .2 to 3 nm may be prepared according to the methods described in Iijima, S., Nature **363**, 603 (1993) and Bethune, D.S., Nature **363**, 605 (1993). These nanotubes are believed to be significantly stiffer than coiled proteins or DNA.

Since a DNA helix fragment is a rigid, electronically coupled aromatic column of stacked base pairs within a sugar phosphate backbone about 2 nm thick which can efficiently promote electron-transfer reactions over distances of more than 40 Å, such helices are useful as probe tips according to the invention.

Polyrotaxane nanotubes, prepared by polymerizing a-cyclodextrin sugar units (see Harada, A., Nature **364**, 516 (1993)) are also useful in the practice of the invention. These tubes have internal and external diameters of about .5 and 1.5 nm, respectively. Since cyclodextrins bind organic substrates in aqueous media and the tubes have about the same internal diameter as native biological tubular structures, aside from being useful as a sensing probe, they are useful as extremely selective filters and catalysts for reactions taking place inside the cavity.

Another class of molecules that may be used according to the practice of the invention is cyclic peptide or protein nanotubes having internal diameters of about 0.8 nm (Ghadiri *et al.*, Nature **366**, 324 (1993)). Peptides and proteins may be rigidified with metal atoms, such as copper, which chelate with functional groups internal to the structure. Furthermore, by selecting and/or modifying the amino acid constituents, protein tubes may be prepared to achieve a desired internal diameter or to place reactive moieties at the tip in order to perform particular functions.

The macromolecules, particularly proteins and sugars which have pendant functional groups, can be cross-linked to impart stiffness to the structure. Cross-linking may be accomplished by known methods as disclosed, for example, by Mattson *et al.*, Molec. Biol. Reports **17**, 167-183 (1993).

Accordingly, the present invention provides a scanning probe tip capable of specific molecular interactions with a substrate. The tip is useful for sensing and analyzing microscopic structures and environments by means of the interactions between the tip moieties and the substrate.

In addition to improving scanning probe microscopy, the functionalized tip of the present invention is useful as a molecular biological or chemical tool. For example, a probe functionalized with a DNA molecule bearing a specific code sequence may be used to selectively detect, manipulate or remove specific DNA fragments in a complex mixture of biological molecules, either *in vitro* or *in vivo*. Detection, in this application, may be achieved by monitoring conformational or other changes in the tip molecule caused by binding to its substrate, or by chemical means upon removal of the tip from the mixture, or by means of the force exerted on the tip when it is moved away from the location of the complementary DNA on the substrate.

Similarly, a probe may be functionalized with a protein macromolecule with an epitope sequence at its tip. Such a probe may then be used, *in vitro* or *in vivo* to detect, select or manipulate antigenic materials in mixtures.

Referring to Figure 6, the completed tip comprises a single, rigid macromolecular 45 rigidly attached to a small area of the apex of a scanning probe tip 42.

Accordingly, the present invention provides a scanning probe tip having a smaller radius of curvature, greater angle of taper and a more reproducible shape than the tips previously available. This tip is useful for sensing microscopic environments since the macromolecular tip is able to penetrate or sense finer indentations in a substrate surface than prior tips. In addition,

A probe modified according to the present invention may also be used as a tool in nanofabrication techniques, in molecular chemistry or biochemical catalysis. With the appropriate functional group attached, a probe may be used to add or remove a chemical moiety in a precise location on a molecular structure. Alternatively, a probe may act as a

catalyst in chemical or biochemical reactions by precise positioning of a specific functional group in the reaction environment, or by providing the reaction environment itself, for instance, the cavity of a tubular macromolecular tip.

The present invention has been described, in part, in terms of preferred embodiments. The invention, however, is not limited to the embodiments depicted and described. Rather the scope of the invention is defined by the appended claims.

WHAT IS CLAIMED IS:

1. A method of preparing or probe for sensing a microscopic environment comprising the step of:
   treating at least the tip of a probe selected from the group consisting of silicon, silicon oxides, silicon nitrides, metal oxide and metal with a chemical moiety which functionalizes the surface of said tip with functional groups for sensing a microscopic environment or manipulating a microscopic structure.

2. A method according to Claim 1 wherein said chemical moiety is covalently bound to said probe.

3. A method according to Claim 2 wherein said probe comprises silicon dioxide and said chemical moiety is selected from the group consisting of alkali metal alkanes, alkanols, aryl alcohols, diazoalkanes, ammonium halides, thionyl chloride, alkyl silyl halides, aryl silyl halides, alkoxy silanes, alkyl silanes, alkylcarboxy silanes, and amino silanes.

4. A method according to Claim 2 wherein said tip comprises carbon and said chemical moiety comprises a halocarbon.

5. A method according to Claim 2 wherein said tip is selected from the group consisting of gold and silver and said chemical moiety comprises alkylthiols.

6. A method according to Claim 2 wherein said tip comprises aluminum and said chemical moiety comprises an alkyl phosphate.

7. A method according to Claim 2 wherein said tip comprises platinum and said chemical moiety comprises an olefinic group.

8. A method of preparing a probe for sensing or manipulating a microscopic environment or structure comprising the steps of:
   (a) protecting from a passivating agent an area at the tip of a probe suitable for scanning microscopy wherein said area is suitable for linkage thereto of a single, rigid macromolecule having a proximal and a distal end;

(b) passivating said tip with said passivating agent whereby the unprotected portion of said tip is passivated;
(c) deprotecting said area;
(d) covalently attaching to said probe is said area said proximal end of said rigid macromolecule, said macromolecule having a substantially cylindrical or conical shape defined by a longitudinal dimension, an outer proximal diameter at said proximal end and an outer distal diameter at said distal end.

9. A method according to Claim 8, wherein said area is in the range of about 10000 $Å^2$ to 3 $Å^2$.

10. A method according to Claim 8, wherein said outer distal diameter is in the range of about 2 to about 50 Å.

11. A method according to Claim 8, wherein said macromolecule comprises a peptide.

12. A method according to Claim 8, wherein said macromolecule comprises a protein.

13. A method according to Claim 8, wherein said macromolecule comprises a DNA double helix.

14. A method according to Claim 8, wherein said macromolecule comprises a carbon nanotube.

15. A method according to Claim 8, wherein said macromolecule comprises a polyrotaxane.

16. A method according to Claim 8, wherein in said step (b) said passivation is preformed by treatment with diazoalkane.

17. A method according to Claim 8, wherein in said step (b) said passivation is performed by fluorination.

18. A method according to Claim 8, wherein in said step (b) said passivation is performed by stepwise chlorination and alkylation or arylation.

19. A method according to Claim 8, wherein in said step (b) said passivation is preformed by alkyl silanation.

20. A method according to Claim 8, wherein in step (b) said passivation is performed by alkyl hydrosilanation.

21. A method according to Claim 8, wherein in said step (b) said passivation is performed by treatment with organosilanes.

22. A method according to Claim 8, wherein in said step (b) said passivation is performed by low pressure chemical vapor deposition.

23. A method according to Claim 8, wherein in said step (b) said passivation is performed by oxidation.

24. A method of sensing a microscopic environment comprising the step of placing a probe into said environment wherein the surface of said probe comprises chemical moieties selected from the group consisting of alkali metal alkanes, alkanols, aryl alcohols, diazoalkanes, ammonium halides, thionyl chloride, alkyl silyl halides, aryl silyl halides, alkoxy silanes, alkyl silanes, alkylcarboxy silanes, aminosilanes, halocarbons, alkylthiols, alkyl phosphates and olefins.

25. A method of sensing a microscopic environment comprising the step of placing a probe with a sensing tip into said environment, said tip comprising the end of a rigid, substantially cylindrical or conical shaped macromolecule.

26. A method according to Claim 25, wherein said end has an outer diameter in the range of about 2 to about 50 Å.

27. A method according to Claim 25, wherein said macromolecule is a peptide.

28. A method according to Claim 25, wherein said macromolecule is a protein.

29. A method according to Claim 25, wherein said macromolecule is a DNA double helix.

30. A method according to Claim 25, wherein said macromolecule is a carbon nanotube.

31. A method according to Claim 25, wherein said macromolecule is a polyrotaxane.

32. A probe for sensing or manipulating a microscopic environment or structure comprising a scanning probe surface-functionalized according to the method of Claim 3, 4, 5, 6 or 7.

33. A probe for sensing or manipulating a microscopic environment or structure comprising a scanning probe surface-functionalized according to the method of Claim 2.

34. A probe for sensing a microscopic environment comprising a scanning tip comprising the end of a rigid, substantially cylindrical or conical shaped macromolecule.

35. A probe according to Claim 34, wherein said end has an outer diamter in the range of about 2 to about 50 Å.

36. A probe according to Claim 34, wherein said macromolecule is a cyclic peptide.

37. A probe according to Claim 34, wherein said macromolecule is a protein.

38. A probe according to Claim 34, wherein said macromolecule is a DNA double helix.

39. A probe according to Claim 34, wherein said macromolecule is a carbon nanotube.

40. A probe according to Claim 34, wherein said macromolecule is a polyrotaxane.

41. A method of microscopic scanning to analyze the chemical composition of a surface comprising the steps of:
    (a) providing a scanning probe microscope with a scanning probe surface-functionalized according to the method of Claim 3, 4, 5, 6 or 7;
    (b) conducting scanning probe microscopy on said surface.

42. A method of microscopic scanning to analyze the chemical composition of a surface comprising of:
    (a) providing a scanning probe surface-functionalized according to the method of Claim 2;
    (b) conducting scanning probe microscopy on said surface.

43. A method of microscopic scanning to determine the topography of a surface comprising of:
    (a) providing a scanning probe microscope with a scanning tip comprising the end of a rigid, substantially cylindrical or conical shaped macromolecule; and
    (b) conducting scanning probe microscopy on said surface.

44. A method of sorting molecules comprising the steps of:
    (a) providing a scanning probe tip functionalized with a molecule having selective affinity for a molecule of interest;

    (b) introducing said probe into said the environment of said molecule; and

(c) contacting said tip with said molecule such that said molecule selectively bonds to said tip.

45. The method according to claim 44 further comprising manipulating said molecule in said environment with said tip.

46. The method according to claim 44 further comprising removing said molecule bound to said tip from said environment.

47. The method according to claim 46 further comprising removing said molecule from said tip.

48. A method of detecting a microscopic substrate comprising the steps of:
    (a) providing a probe tip functionalized with a molecule having selective affinity for said substrate;
    (b) introducing said tip into an environment where said substrate is sought;
    (c) scanning said tip about said environment;
    (d) removing said tip from said environment; and
    (e) analyzing said tip for the presence of said substrate.

49. A method of providing chemical or biochemical catalysis at a microscopic site comprising the steps of:
    (a) providing a probe tip functionalized with a molecule having a specific functional moiety or structure;
    (b) positioning said tip and said site where catalysis is desired.

50. A method of nanofabrication comprising the steps of:
    (a) providing a probe tip functionalized with a molecule having a specific functional moiety or structure;
    (b) positioning said tip in the environment of a target molecular locus; and
    (c) adding, removing, or altering a chemical group or structure at said locus by interaction of said functional group with said locus, or by an externally applied influence such as an electric potential, a magnetic field, a pressure wave, or a flux of light.

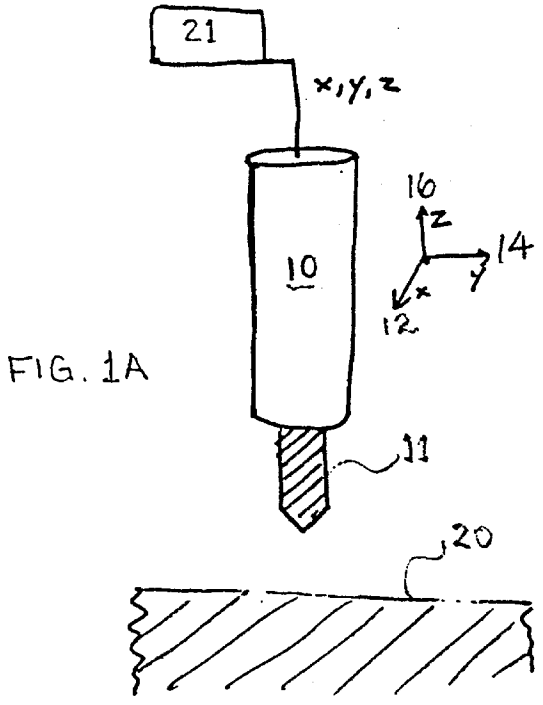

FIG. 1A

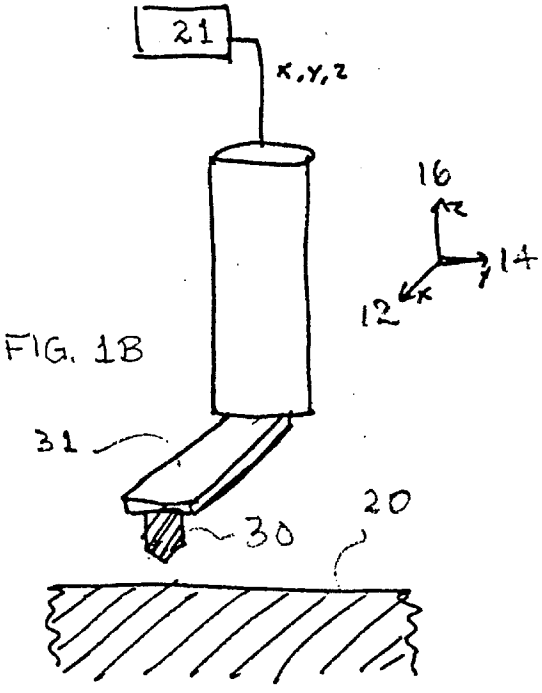

FIG. 1B

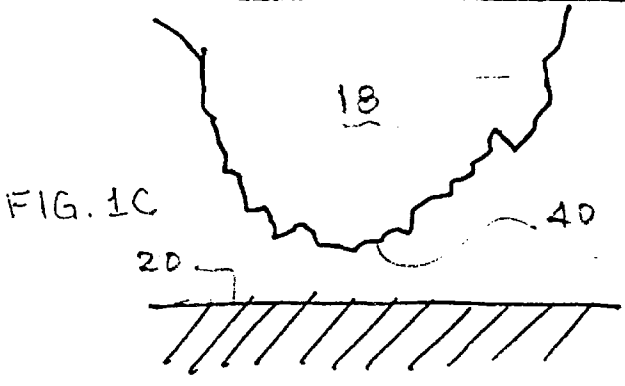

FIG. 1C

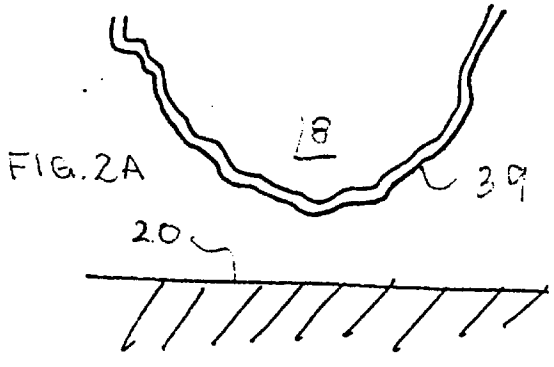

FIG. 2A

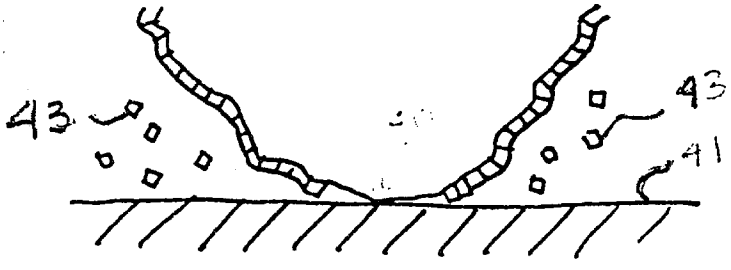

FIG. 2B

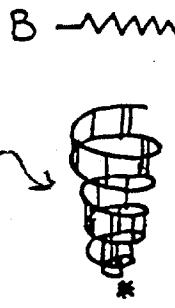

FIG. 4

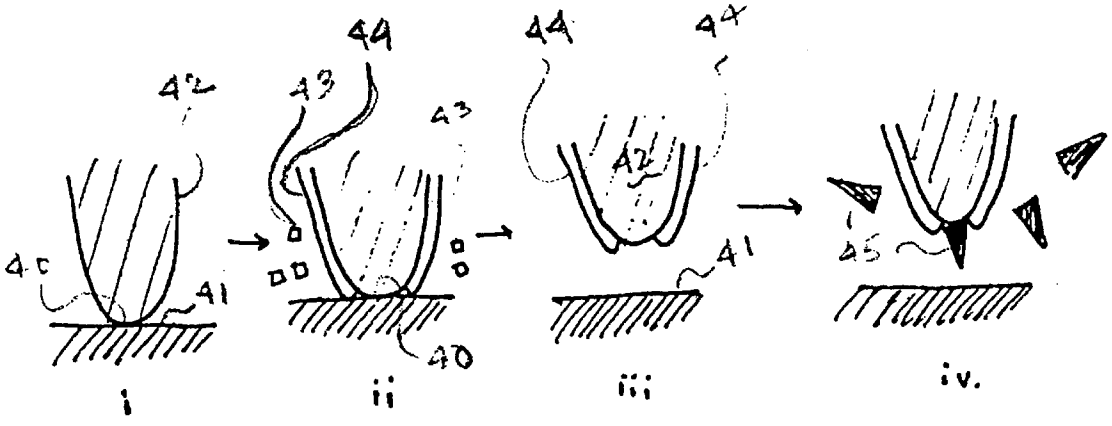

FIG. 5

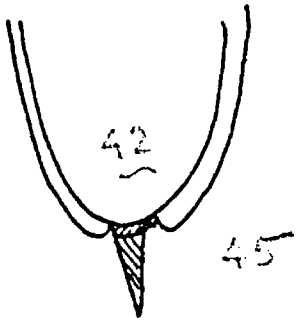

FIG. 6